INTERFACES IN ALL SOLID STATE LITHIUM-ION BATTERIES

by

Pengyu Xu

A Dissertation

Submitted to the Faculty of Purdue University

In Partial Fulfillment of the Requirements for the degree of

Doctor of Philosophy

School of Materials Engineering

West Lafayette, Indiana

May 2021

THE PURDUE UNIVERSITY GRADUATE SCHOOL
STATEMENT OF COMMITTEE APPROVAL

Dr. Lia Stanciu, Chair
School of Materials Engineering

Dr. Haiyan Wang
School of Materials Engineering

Dr. R. Edwin Garcia
School of Materials Engineering

Dr. Elliott Slamovich
School of Materials Engineering

Approved by:
Dr. David F. Bahr

To my family

ACKNOWLEDGMENTS

Firstly, I would like to thank my advisor, Prof. Lia Stanciu for her kind guidance, constant support and encouragement. She kindly mentored me to overcome all the difficulties during my PhD study. She always supports me to explore the field that I am interested and encourages me to become an independent researcher. I am really grateful for how much she helped me in both my research and daily life. I am also grateful to thank my committee members, Prof. Haiyan Wang, Prof. Edwin García, and Prof. Elliott Slamovich for their continuous help on my research and constructive advice. I would also like to thank Prof. Wolfgang Rheinheimer for his generous help in my research.

I would like to acknowledge my colleagues and friends for the great help throughout my graduate studies. Yifan Zhang and Jie Ding for guiding me through operations of FIB, Zhongxia Shang, Bo Yang and Zhimin Qi for helping me with TEM trainings, Xin Li Phauh for training me Spark Plasma Sintering, Andrew Schlup for helping me with hot-pressing and attrition milling, Lucas Robinson for the collaboration through battery project. Also, my groupmates, Winston Chen, Li-kai Lin, Susana Diaz-Amaya, Shoumya Nandy Shuvo and Ana Maria Ulloa Gomez for the kind help and fruitful discussions.

Finally, I would like to thank my family, my father Zhenxin Xu and mother Wei Wei for the love and support during my PhD study abroad.

TABLE OF CONTENTS

LIST OF TABLES

LIST OF FIGURES

LIST OF ABBREVIATIONS AND SYMOBOLS

Al	Aluminum
Co	Cobalt
Ti	Titanium
La	Lanthanum
Mn	Manganese
Li	Lithium
BSE	Backscattered electron
CS	Cold Sintering
LLTO	Lithium Lanthanum Titanate
LATP	Lithium Aluminum Titanium Phosphate
LLZO	Lithium Lanthanum Zirconium Oxide
LMO	Lithium Manganese Oxide
LCO	Lithium Cobalt Oxide
SSB	Solid State Battery
LIB	Lithium-Ion battery
ASSLIB	All Solid-state lithium-ion battery
SE	Solid electrolyte
SEI	Solid Electrolyte Interphase
SAED	Selected Area Electron Diffraction
SEM	Scanning Electron Microscopy
TEM	Transmission Electron Microscopy
XRD	X-ray Diffraction
FIB	Focused Ion Beam
STEM	Scanning Transmission Electron Microscopy

HRTEM	High Resolution Transmission Electron Microscopy
HAADF	High-angle Annular dark field
EELS	Electron Energy Loss Spectroscopy
IEF	Interelectrode Film
CCD	Critical Current Density
HOMO	Highest Occupied Molecular Orbital
LUMO	Lowest Unoccupied Molecular Orbital
XPS	X-ray photoelectron spectroscopy

ABSTRACT

Lithium-ion batteries (LIB) have been widely applied to portable electronic devices in the past decades. However, there has been a growing safety concern on Li-ion batteries, stemming from the flammability of the conventional liquid electrolytes. Replacing the organic liquid electrolytes with solid electrolytes (SEs) is generally viewed as the best potential solution to this challenge. Even though ceramic solid electrolytes are nonflammable and can tolerate extreme temperatures, there is still a long way before commercialization of solid state batteries (SSBs) is possible. The high interfacial resistance between SEs and electrodes is considered as the biggest roadblock standing in the way of the practical realization of SSBs. Such interfacial resistance could cause great capacity loss, as well as poor cycling performance. Therefore, in this thesis, research efforts have been made to understand the origins of the observed large interfacial resistance, and explore possible approaches to alleviate its impact on battery performance.

In this thesis, we studied interfaces include cathode-electrolyte and anode-electrolyte interfaces. In the study of the cathode-electrolyte interface, we applied Spark Plasma Sintering (SPS) to prepare $Li_{0.33}La_{0.57}TiO_3$(LLTO)/$LiMn_2O_4$, $Li_{1.3}Al_{0.3}Ti_{1.7}(PO_4)_3$/ $LiMn_2O_4$, $Li_{0.33}La_{0.57}TiO_3$/$LiCoO_2$ half-cells. Along with Scanning Electron Microscopy/ Transmission Electron Microscopy to characterize interfacial microstructure. The results showed that the interdiffusion between cathode and electrolyte materials leads to the formation of a micron-thick interdiffusion layer, and result in interfacial resistances on the level of 10^5 Ω, which is about 40 times higher than the resistance of individual SEs. Thus, the formation of interdiffusion layers is the dominant origin of high electrical resistance in cathode-electrolyte interfaces. Cold sintering has been applied to prepare LLTO/LMO half-cells. The interdiffusion proved to be somewhat alleviated by cold sintering. However, more work is needed to improve particle compaction and surface contact.

Towards the understanding of anode-electrolyte interface properties, it is the dendrite formation in LLTO that was studied herein. We found that the reaction between Li and LLTO could lead to an enhanced durability of LLTO against Li dendrites. The reaction product has better conductivity than LLTO. More evidence on

LLTO battery performance is still needed, however, this discovery has the potential of solving the dendrite problem for Li-metal SSBs.

CHAPTER 1. OVERVIEW OF KNOWLEDGE ON SOLID STATE LITHIUM-ION BATTERIES

1.1 Background

Lithium ion batteries (LIBs) have been applied to portable electronics as power source for the past decades. Therefore, they become established as one of the most promising energy storage devices.[1] LIBs are favorable in various applications as a result of their high power density and great cycling performance. State-of-the-art batteries with as high energy density as 260Wh/kg have been realized[2]. With the increasing demand for a low carbon society, possibilities of applying LIBs to electric vehicles (EVs) have been widely investigated.[3] To fulfill requirements for EVs, batteries with greater power densities, higher safety level, longer life and lower costs than those currently available are needed.[4] Safety issues have been the main drawbacks that hinder the LIBs application in EVs.[5] Electrolytes currently used in conventional batteries are flammable liquid organics. Their leakage at high voltages or elevated temperatures can bring about great safety concerns such as combustion.[6] One of the potential solutions is to replace the traditional organic electrolytes with solid state electrolytes (SSEs). The nonflammable SSEs usually have better mechanical properties than liquid electrolytes. Therefore, all solid state batteries can have a better packing efficiency as they break the restrictions of traditional design geometries.[7] Moreover, ceramic oxide electrolytes typically provide broader electrochemical windows, which allows the use of electrodes with larger chemical potential difference, and therefore can increase the voltage of the batteries. SSEs also make it possible to use lithium metal anodes in the batteries by suppressing the dendrite formation on the metal surface[8].Overall, the use of SSEs allows electrodes with higher capacity, as well as higher voltage of the batteries. Thus, a successful solid-state battery, if realized, is expected to have a higher energy density than those of existing conventional devices. The energy density of a battery follows the equation:

$$\mathrm{E} = \frac{C \times V}{m}$$

where E represents the energy density, C represents the charge capacity, V represents the voltage of the cell and m is the active mass of the electrode material. Potentials and capacities of common electrodes are shown in Figure 1.1.[9]

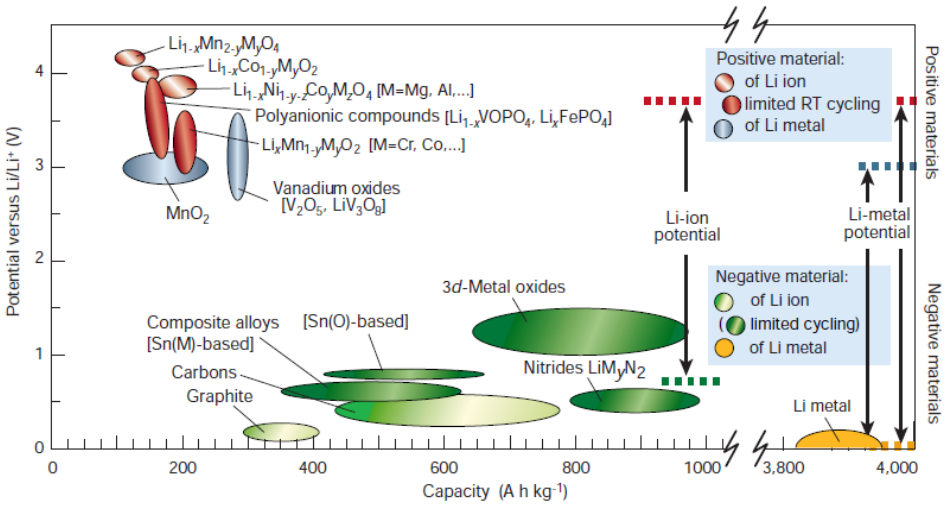

Figure 1.1 Voltage versus capacity for cathode and anode materials in LIBs[9]

Despite all the advantages of SSEs mentioned above, there are still great challenges encountered when trying to apply SSEs to all-solid-state batteries. Poor ionic conductivities of SSEs (compared to traditional liquid electrolytes) and high interfacial resistances between SSEs and electrodes are drawbacks that can result in low power densities and inferior cycling performance[10]. Some of the recent works have already developed SSEs with ionic conductivities comparable with the liquid ones. Kanno's[11] group developed a superionic conductor, $Li_{10}GeP_2S_{12}$, with an ionic conductivity of 10^{-2} S cm^{-1} at room temperature. Another glass-ceramic conductor Li_2S-P_2S_5, synthesized by Tatsumisago[12] also exhibited a high ionic conductivity of 3×10^{-3} S cm^{-1}. However, there is lack of fundamental understanding when it comes to the interfacial phenomena between electrodes and electrolytes. Some theories have been proposed to explain the high interfacial resistance, such as the space-charge layer effect,[13] and formation of interfacial phases during charging and discharging.[14] There is evidence that the formation of inter-electrode films (IEF) at the interface of ceramic compounds could heavily influence the charge transfer kinetics and cost great capacity loss.

IEFs are charged 2D interfacial phases (interphases) formed at the electrode/ electrolyte surface during cycling. Similar to the solid electrolyte interface (SEI) layers, which control the performance of traditional batteries, IEFs could define the high interfacial resistance between electrode/electrolyte in solid-state batteries. The formation of IEF layers could affect both

conductivity of electrolytes and electrode/electrolyte contact areas, which contribute to the ohmic loss in batteries.

However, the chemical and thermodynamic properties of the IEFs as well as the phase formation dynamics are still lacking complete understanding. Therefore, in this thesis, the goal is to study the fundamentals of charged IEF, to aid in engineering of structurally stable 2D interfacial phases that maximize the interfacial conductivity and mechanical integrity. This study could not only reveal the origin of large interfacial resistance in solid state batteries, but also provides guidance for the selection of electrode/electrolyte materials.

Last but not least, in addition to the formation of IEF at electrode/electrolyte interface, dendrite formation at anode/electrolyte interface is another significant challenge for solid-state batteries. In the last chapter, we also present the results of a study on the dendrite formation conditions at anode/electrolyte interface.

1.2 Solid State Electrolytes

1.2.1 Conduction of Li-ions in solid state electrolytes

Solid state electrolyte materials typically exhibit good conductivities for ions, while preventing the transport of electron species.[15] Ceramic electrolytes typically transport ions through point defects such as vacancies or interstitial ions.[16] For intrinsic point defects (Schottky defects and Frenkel defects), the number of defects obeys the Arrhenius equation:

$$N_D = N \cdot \exp[-\frac{E_f}{2KT}] \quad (1)$$

Where E_f is the formation energy of defects, N_D is the number of defects[17]. However, extrinsic defects introduced by impurities or dopants also contribute to the transportation of ions.

In SSEs, the movement of ions can be described by the simple hopping model, where the defects (vacancies and interstitial ions) are transported by jumping isolated through lattice sites.[15] In this case, the diffusion coefficient (D) can be described as:

$$D = \alpha d^2 v \quad (2)$$

Where α is the reciprocal of possible jumping directions (coordination number), d is the jumping distance and υ is the jumping frequency. The jumping frequency υ can be further interpreted by:

$$\upsilon = \beta\upsilon_0 \exp[-\Delta G/RT] \quad (3)$$

Where β is the fraction that ions can move and ΔG is the free energy of migration. The ionic conductivity follows Nernst-Einstein relation:

$$\sigma = \frac{nq^2D}{kT} \quad (4)$$

Where n is the number of ions that can move. Thus, if we plug Equation (2) and Equation (3) into Equation (4), we can see that the conductivity is proportional to n, υ_0 and ΔG. For the fast ion conductors that are suitable for electrolytes, the activation energy (mainly activation enthalpy[15]) should be several magnitudes lower than common materials. Also, the conductivity can be written in a simpler formula:

$$\sigma = \mathrm{A}v_d n_d = Aexp[-\frac{E_f}{k_B T}]\exp[-\frac{\mathrm{E_m}}{k_B T}] \quad (5)$$

Where E_f is the defect formation energy and E_m is the hopping barrier energy. In summary, a solid fast ion conductor is usually highly polarized, with weak binding energy. It should also have a low coordination number of mobile ions. [16] As a result, a lithium-ion conductor should have suitable conduction pathways for lithium ions, and low activation energy of the defects that transport lithium ions.

1.2.2 Common types of ceramic solid electrolytes

Figure 1.2[18] shows the ionic conductivities of common solid state electrolytes, among which we can see that the LISCON-like electrolytes (lithium ion super conductors, for example, Li_2S-GeS_2-P_2S_5) have the highest ionic conductivities. These conductivities are comparable with those of the traditional organic electrolytes (EC; DMC and 1M $LiPF_6$). Other structures for solid

electrolytes, such as Garnet, NASICON-like, and Perovskite, also exhibit ionic conductivities of 10^{-3} S cm^{-1}.

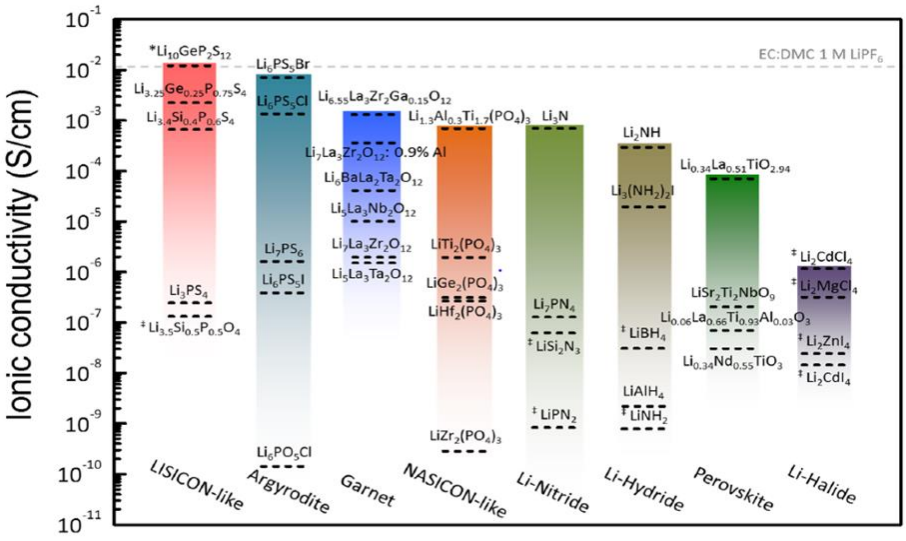

Figure 1.2 Ionic conductivity of common types solid electrolytes [18]

Lithium Lanthanum Titanite (LLTO)

Lithium Lanthanum Titanite ($Li_3xLa_{(2/3-x)}TiO_3$) is a perovskite(ABO_3) type lithium ion conductor (Figure 1.3). Inaguma[19] first reported the $Li_3xLa_{(2/3-x)}TiO_3$ (x=0.11) had a bulk ionic conductivity of 1×10^{-3} S cm^{-1} at room temperature. However, the overall ionic conductivity reduced to 2×10^{-5} S cm^{-1} when considering the grain boundary resistance. For a perovskite structure (Figure 1.3 (a)) [20] , Li^+ and La^{3+} share A sites, and Ti^{4+} occupy B sites. The trivalent La ions introduce A site vacancies to the structure while Li ions take up vacancies; therefore the $Li_3xLa_{(2/3-x)}\square_{(1/3-2x)}TiO_3$ (□ represents A site vacancies) transports Li ions through these vacancies. The $Li_3xLa_{(2/3-x)}\square_{(1/3-2x)}TiO_3$ has been reported to be stable through multiple compositions. The X value varies from 0.04 to 0.16, which changes the crystal structures of LLTO.[21] Generally speaking, there are two main types of LLTO with different crystal structures: α-LLTO and β-LLTO. LLTO is considered as a mixture of these two phases. α-LLTO has a cubic structure with Pm3m symmetry (a=0.38 Å), where La^{3+} and Li^+ ions are randomly distributed at A sites. While β-LLTO has a P4/mmm symmetry, alternative Li^+ and La^{3+} rich layers form a tetrahedral (Figure 1.3(b), where a=0.38 Å and c=0.76 Å.[14]) structure. The presence of the β-LLTO phase accounts for the high conductivity of LLTO, in which the lithium ions mainly diffuse through vacancies in the ab plane.

This diffusion is bottlenecked by oxygens that form TiO_6 octahedrals[22]. Researchers have found out that by applying larger A site ions than La^+ can increase bottleneck size and therefore increase the ionic conductivity of LLTO.[23] Although LLTO is stable at high potentials (5V vs Li/Li^+), it is unstable at low potentials (1.5V vs Li/Li^+) where Ti^{4+} ions get reduced to Ti^{3+}. This restricts the application of LLTO as a solid electrolyte for batteries because it is reactive against common anodes like lithium and graphite.[22]

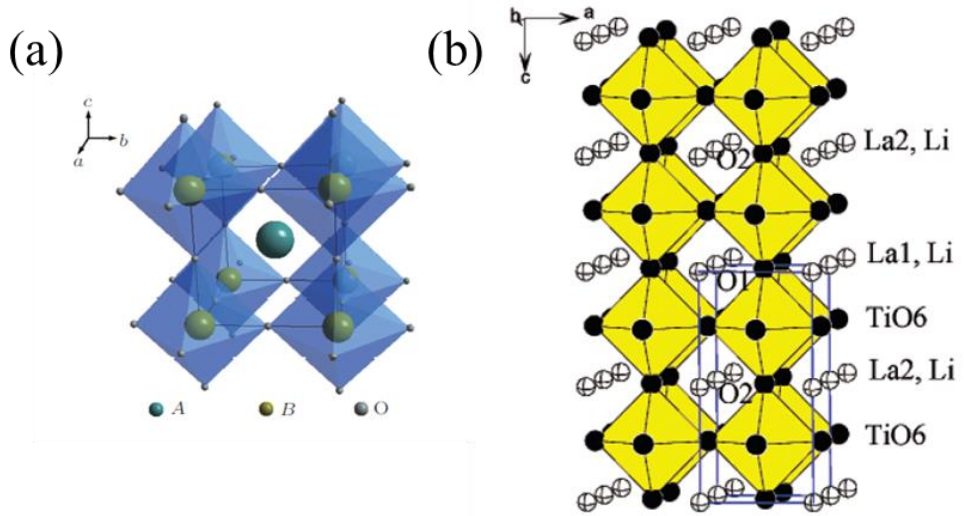

Figure 1.3 (a) Schematic of perovskite structure [20] (b) Structure of tetragonal $Li_3xLa_{(2/3-x)}TiO_3$ (x=0.11) [21]

Lithium Lanthanum Zirconate ($Li_7La_3Zr_2O_{12}$)

$Li_7La_3Zr_2O_{12}$(LLZO) is a new garnet structure($A_3B_2M_3O_{12}$) lithium ion conductor. Garnet structure conductors have superior ionic conductivity because of their ability to accommodate an excess amount of lithium ions. In a garnet crystal($A_3B_2M_3O_{12}$), which is a cubic structure, A sites have a coordination number of 8, B sites are octahedral (CN=6), and M sites are tetrahedral (CN=4)[18]. For lithium ion conductors, lithium ions would take tetrahedral (M) sites. Researchers found out that to get a higher ionic conductivity, more lithium ions could be added to the structure. This made a $Li_5La_3M_2O_{12}$ (M=Nb, Ta) structure.[24] Additional Li^+ ions are held in a mixture of tetrahedral coordinate M sites and distorted octahedron sites at the vacant of $A_3B_2M_3O_{12}$ structure. [25] Then, Wepper reported $Li_7La_3Zr_2O_{12}$ (LLZO) with a room temperature bulk ionic conductivity of 4×10^{-4} S/cm and an overall conductivity of 1×10^{-4} S/cm[26]. The crystal structure of LLZO is

shown in Figure 1.4 (a)[27] . LaO_8 and ZrO_6 constructs the garnet structure, and Li^+ ions (showed in Figure 1.4(b)), take the tetrahedral sites (Li1) and distorted octahedral sites (Li2), the lithium sites form a 3D network as Figure 1.4(c), which explains the high ionic conductivity of LLZO. Additionally, Zr^{4+} is stable against Li metal at low potentials, thus the cubic phase LLZO can be applied to batteries with lithium metals anodes. However, there are also reports mentioned that the LLZO is unstable against CO_2 and water, which are considered as shortcomings of this garnet type electrolyte.[28]

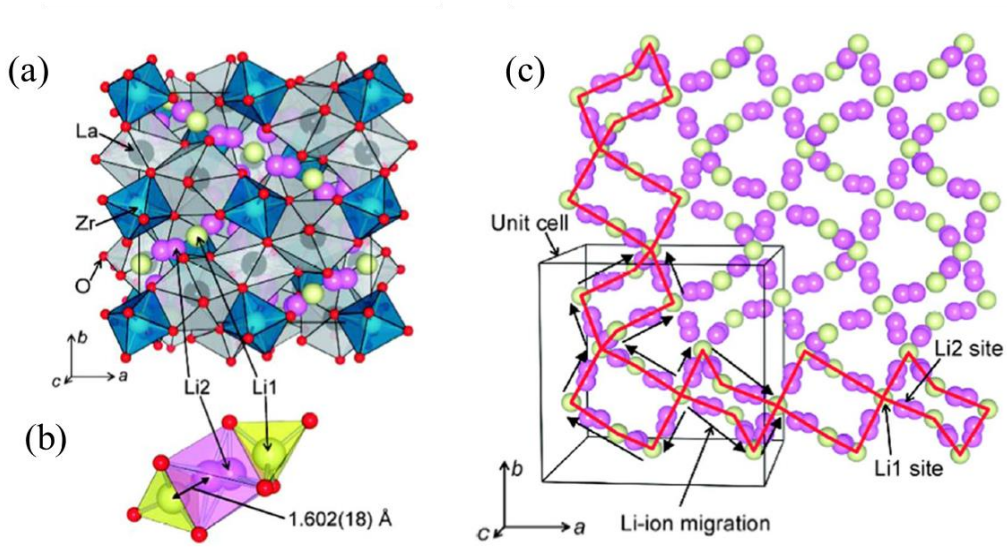

Figure 1.4 (a) Crystal structure of the LLZO (b)Coordination polyhedral around Li sites (C) 3D network structure of Li atomic arrangement in a cubic LLZO

Lithium Aluminum Titanium Phosphate ($Li_{1.3}Al_{0.3}Ti_{1.7}(PO_4)_3$)

$Li_{1.3}Al_{0.3}Ti_{1.7}(PO_4)_3$ (LATP) is a NASICON type lithium ion conductor. The NASICON type solid $AM_2(PO_4)_3$ (A=Na, M=Ge, Ti, Zr) was first found out to have great Na ion conductivity.[29] The structure schematic is shown in Figure 1.5 (a).[20], where Li^+ or Na^+ takes A sites, and the BO_4 tetrahedra and MO_6 octahedra are connected by oxygen ions on the corners. As we are discussing Li ion conductor, A sites should be taken by Li ions. The Li^+ also have two additional sites in the structure, which are shown in Figure 1.5 (b), M1 and M1/2 sites are the favorable positions for Li^+.[30] These sites form a 3D network, where lithium ions are transported by hopping among these sites. For the $LiTi_2O_4$, the ionic conductivity can be further improved by substituting part of Ti^{4+} ions with Al^{3+}. To maintain the charge neutrality, more lithium ions should be accommodated in the crystal structure. A bulk ionic conductivity of 3×10^{-3} S cm^{-1} was reported

for $Li_{1.3}Al_{0.3}Ti_{1.7}(PO_4)_3$[31]. However, the LATP has been proved to be unstable at low potentials, as Ti^{4+} get reduced at 2.5V vs (Li/Li^+). This makes LATP incompatible with low potential anodes like lithium metals or graphite. The high ionic conductivity and high potential stability still makes LATP a promising solid electrolyte material[31].

Other types of lithium ion conductors such as thio-LISICON conductors are also reported to have great room temperature ionic conductivity, however, the stability in ambient atmosphere and the stability against metal Li are still the main concerns for this type of electrolyte.[14]

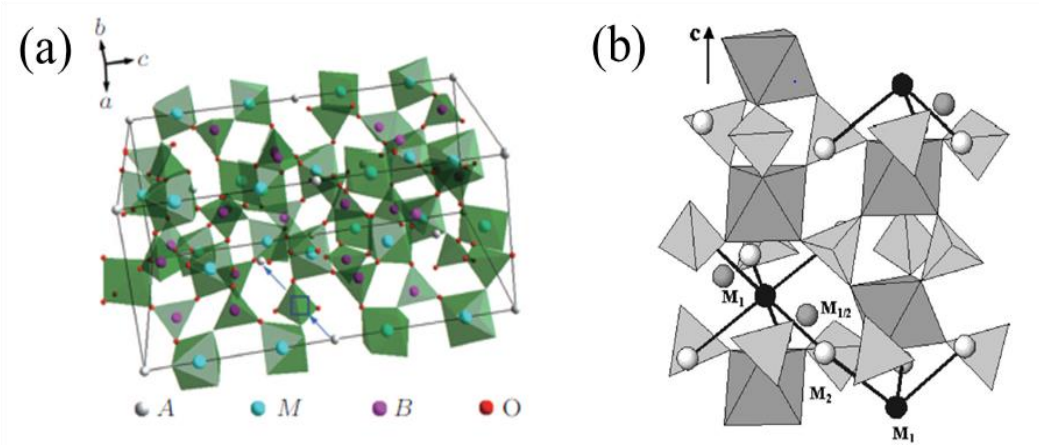

Figure 1.5 (a) Crystal structure of the LLZO (b)Coordination polyhedral around Li sites (C) 3D network structure of Li atomic arrangement in a cubic LLZO

1.3 Electrolyte/ electrode interface in LIBs

Interfacial properties between electrode and electrolyte have a significant effect on the transportation of lithium ions. Additionally, in SSBs, undesired products of side-reactions cannot dissolve or diffuse in the solid electrolyte, which would further influence the performance of the batteries.[32] Thus, understanding the electrode/electrolyte interfacial properties can help engineer the interface to get favorable ionic transport performance.

1.3.1 Stability between electrolyte and electrode.

For the conventional lithium ion batteries with organic electrolytes, during the first cycle, solid electrolyte interphase (SEI) layers will form on the surfaces of both cathode and anode, and cause about 10% capacity loss.[33] The SEI is a passivation layer formed by reduction of electrolyte.

However, this SEI layer is Li ion conductive and electron insulating, thus it prevents the electrolyte from further decomposition and ensure the stable cycling of batteries.[34] The formation of SEI can be attributed to the electro-chemical potential of electrode laying outside the electrochemical window of the electrolyte. The schematic is shown in Figure 1.6[35]. In the battery system, the anode is reductive, while the cathode is oxidating. The electrochemical window (E_g) of an electrolyte refers to the energy separation between its lowest unoccupied molecular orbital (LUMO) and highest occupied molecular orbital (HOMO). μ_A and μ_C refer to the electrochemical potential of anode and cathode. From Fig. 6 we can notice, for an anode, if μ_A is above the LUMO, the anode would donate electrons to the electrolyte, i.e. reduce the electrolyte. This happens unless a passivation layer (SEI) is formed on the interface, which can block the further transportation of electrons from anode to electrolyte. Similarly, for a cathode, if μ_C is lower than the HOMO, the cathode would take electrons from the electrolyte, i.e. oxidize the electrolyte unless the formation of SEI. Thus, a stable battery assembly requires the electrochemical potentials of both electrodes be located within the electrochemical window of the electrolyte. However, the open circuit voltage (OCV) obeys:

$$\mathrm{F} \times \mathrm{Voc} = \mu_A - \mu_C < E_g$$

Where F is the faraday constant. Thus the OCV of a battery is controlled by the difference in electrochemical potentials between two electrodes[36]. By allowing the formation of SEI on electrodes, we broaden the potential difference of electrodes and increase the OCV of the battery, which accounts for a higher energy density of the battery. The carbonate electrolytes we currently use have oxidation potentials at below 4.7 V (vs Li/Li^+)[37], and reduction potentials at about 1V (vs Li/Li^+)[38]. Therefore, traditional organic electrolytes are unstable against some high voltage cathodes such as $LiNi_{0.5}Mn_{1.5}O_4$. This brings us back to the desire for solid state electrolytes that exhibit great stabilities at high voltages.[39] Despite SEIs being often observed at the surface of anode in traditional batteries, SEI can also form at the cathode surface[40]. Moreover, Mohanty[41–43] designed a series of characterization methods to investigate the structure of $Li_{1.2}Co_{0.1}Mn_{0.55}Ni_{0.15}O_2$ (NMC) when cycling at high voltages. He found out that the formation of SEI consumed lithium ions from both the cathode and electrolyte, and therefore reduced the ionic conductivity of the system. Thus, the anode potential would increase as less lithium ions inserted

to the anode, which also in return required a raise in cathode potential to maintain the cutoff voltage of the battery. The cathode structure was distorted and experienced phase transformations, which led to the cycling instability of the cell. This effect is also considered as a shortcoming when SEI forms on the cathode surface.

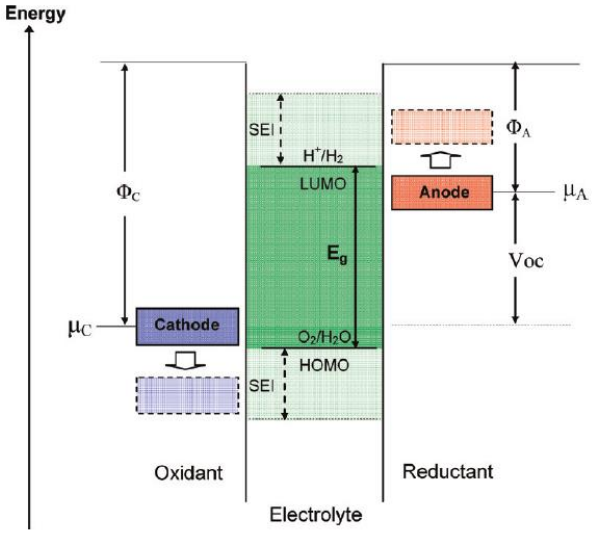

Figure 1.6 Energy requirement for the formation of cathode and anode SEI[35]

1.3.2 Space-charge layer effect

Space-charge layer is reported to be formed at the interface or grain boundaries of ceramics to compensate for the charged surface. For example, if the surface has a positive charge, it will attract negative charged defects to the surface, and form a potential barrier at the interface. This potential barrier will affect the conduction of ions.

Maier published a series of papers focusing on the role of space-charge layer for ionic conduction.[44–47] Maier's study discusses this phenomenon for two F^- ion conductors, BaF_2 and CaF_2 deposited as a layer by layer structure. Part of F^- ions will transfer across the interface to reach an equilibrium and form a space-charge. The transfer of F^- ions will produce vacancies and interstitials in the two materials. However, the point defects (vacancies and interstitials) will in return increase the ionic conductivity.[44] Ohta believed this theory would hold when it comes to the Li^+ cathode and electrolyte interface. As the structure and composition of solid electrolytes had been optimized for ion conduction, the influence of ion transfer would cause the composition to

deviate, and therefore reduce the ionic conductivity for the space-charge layer[13]. Thus, the formation of space-charge layer would increase the resistivity of the interface. Takada also reported the space-charge layer influence on cathode materials against sulfide electrolytes[5]. Solid electrolytes tend to experience so called "anode polarization" at the interface against high voltage cathodes. As the electrochemical potentials of Li ions (fermi level) are equal for the adjacent cathode and electrolyte, the electrochemical potential is the combination of two parts, $\eta_i = \mu_i + z_i q \Phi$[15], chemical potential and electrostatic potential(inner potential). The anodic polarization will increase the electrostatic term for the electrode, in return reduce the chemical potential of Li ions. Lithium ions in the sulfate electrolyte have high mobility, which indicates high lithium ion chemical potential. The difference in chemical potential will drive lithium ions to move from electrolyte to cathode and form a lithium ion depletion zone in the electrolyte, which would greatly increase the resistance.[48] Takada performed a series of studies on developing oxide coatings on the surface of electrode, which were indicated as buffer layers.[5,13,48–50] A "buffer layer" is shown as the upper part in Figure 1.7[5], which is a thin layer of oxide that is electron insulator and ionic conductor. The oxide should have strong lithium ions attraction (electronegativity) to prevent the formation of lithium depletion layer. The result in Figure 1.7 proved the oxide coating can improve the conductivity by two orders of magnitude. They also tried other oxide coatings such as $LiNbO_3$, which also increased the overall conductivity of the cell, and further confirmed the feasibility of buffer layer coatings in reducing the electrode resistance.[51]

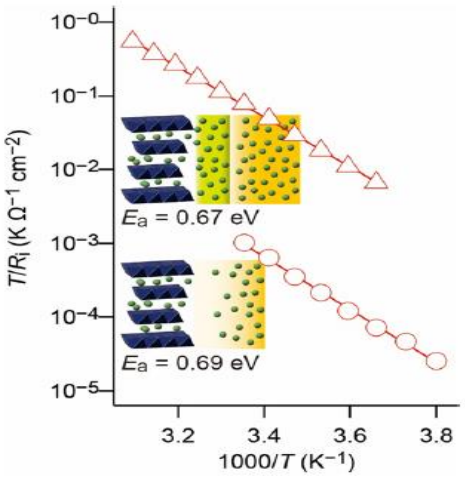

Figure 1.7. The temperature dependent resistance of the electrode with and without a $Li_4Ti_5O_{12}$ layer as the buffer layer.[5]

1.3.3 Interphase (IEF) formation effect

In addition to the space-charge layer theory, which assumes that there is no reaction taking place at the interface, another theory to explain the high interfacial resistance is the interphase formation theory. This theory states that there are low conductivity phases formed at the interface between cathodes and SEs. Either the interdiffusion of elements or side-reactions between cathode and SEs can lead to the interphase formation. As the composition of electrolyte has already been optimized for ionic conduction, the formation of interphase will increase the resistivity of the battery.

Sakuda investigated the $LiCoO_2$ and Li_2S-P_2S_5 interface with the help of Transmission Electron Microscopy (TEM) [52] and observed an interfacial layer after the first charge. They used high-angle angular dark field (HAADF) STEM images to characterize the interface between $LiCoO_2$ and Li_2S-P_2S_5 as shown in Figure 1.8. However, Figure 1.8 (1) (b) indicated that an interfacial layer with the thickness of about 10nm was formed after first charging, and that layer could be responsible for the increased resistance of the cell. The new phase is identifiable in HAADF mode as it shows a good Z contrast. Figure 1.8 (2) presents the distribution of elements in the direction of the arrow, proving that at the interface, there was interdiffusion of Co, P and S. A large amount of Co diffused into the Li_2S-P_2S_5 and only little S diffused into the $LiCoO_2$. From the result, we can deduct that the interfacial layer could consist of S, Co and maybe lithium. The presence of lithium element can be hard to trace as it is invisible under EDS. To suppress the formation of interfacial phases, a Li_2SiO_3 coating was applied to the surface of $LiCoO_2$. The distribution of elements across the interface was shown in Figure 1.8 (3), it is obvious that the Co diffusion was suppressed by the coating. The impedance profile also implied that the coating could reduce the overall resistance of the cell by suppressing the formation of interphase.

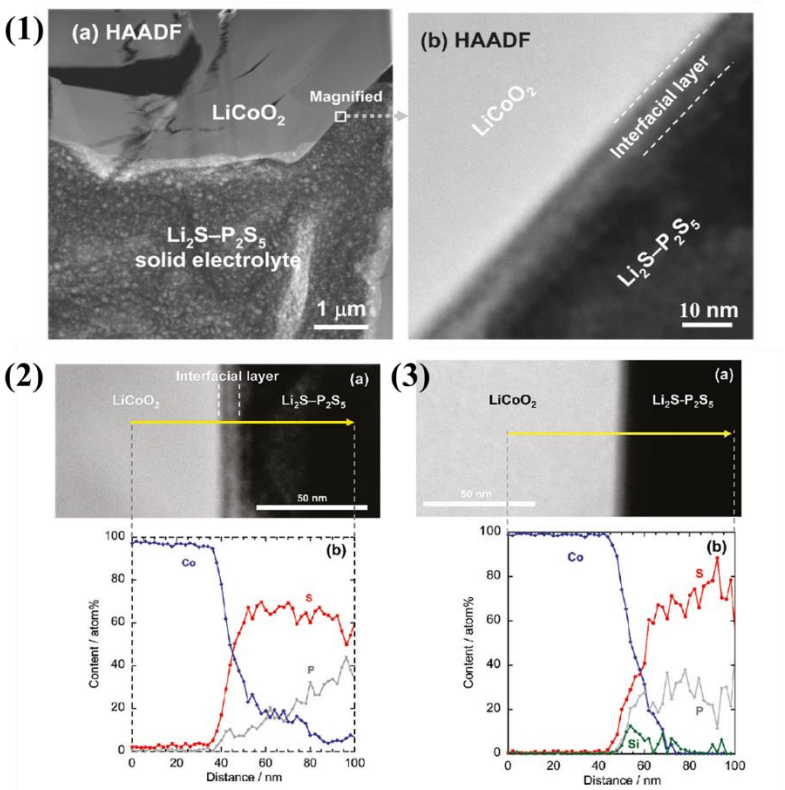

Figure 1.8 (1) (a)&(b) Cross-sectional high-angle annular dark field (HAADF) TEM images of the interface between LCO and Li_2S-P_2S_5 after the first charging. (2) EDX line scan through the interface (3) EDX line scan through the interface after coated the LCO surface with Li_2SiO_3[52]

Koerver investigated the interface between an NMC type cathode ($LiNi_{0.8}Co_{0.1}Mn_{0.1}O_2$) and β-$Li_3PS_4$ with in situ techniques during the first charging.[32] They identified a high resistivity layer formed by the oxidation of SE at the interface with the help of SEM and EIS, which was responsible for the additional resistance detected. Meng group reported a distinct interdiffusion layer observed at the Si/LiPON interface, which was an anode/electrolyte interface. Moreover, a lithium ion accumulation layer was also detected at the $LiCoO_2$/LiPON interface; the authors confirmed the existence of an interfacial phase by detecting the lithium ion distribution with the help of STEM/EELS. Layers at the surfaces of both electrodes could contribute to the increased lithium transportation resistance detected. Additionally, an interdiffusion interphase with the thickness of 50nm was also reported by Kim for $LiCoO_2$/LLZO combination (LLZO is $Li_7La_3Zr_2O_{12}$). By analyzing electron diffraction patterns, the diffusion layer was found to contain La_2CoO_4 .[53] Ceder used simulation methods to predict a workable cathode and electrolyte

combination, which had good agreement with experimental data. His simulation results also provide some alternative cathode/electrolyte combinations that were never attempted by experimentists.[7] Part of the simulation results performed on LLZO in contact with several common electrode materials are shown in Table 1.1. These results further prove that at cathode voltage, there are often side reactions, which will lead to formation of interphases. That interphase could possibility increase the interfacial resistance and cause capacity loss.

Table 1.1 Reactions could happen to LLZO/ cathode combinations according to simulation[7]

Cathode/electrolyte	Reaction at cathode voltage	Reaction with mixing
LLZO/$LiCoO_2$	$4Li_7La_3Zr_2O_{12} \rightarrow 7O_2+4La_2Zr_2O_7+ 2 La_2O_3$	$4Li_7La_3Zr_2O_{12} \rightarrow 7O_2+4La_2Zr_2O_7+ 2 La_2O_3$
LLZO/$LiFePO_4$	$4Li_7La_3Zr_2O_{12} \rightarrow 7Li_2O_2+4La_2Zr_2O_7+ 2 La_2O_3$	$10\ LiFePO_4+ Li_7La_3Zr_2O_{12} \rightarrow 7Li_3PO_4+3LaPO_4+5Fe_2O3_+ 3La_2Zr_2O_7$
LLZO/$LiMnO_2$	$4Li_7La_3Zr_2O_{12} \rightarrow 8LiLaZrO_4+5Li_2O_2+2La_2O_3$	$7LiMnO2+2Li_7La_3Zr_2O_{12} \rightarrow La_2O_3+7Li_2MnO_3+ 2La_2Zr_2O_7$
LLZO/$LiNiO_2$	$4Li_7La_3Zr_2O_{12} \rightarrow 8LiLaZrO_4 +5Li_2O_2 + 2La_2O_3$	$7LiNiO_2+Li_7La_3Zr_2O_{12} \rightarrow 2La_2Zr_2O_7+7Li_2NiO_3+ La_2O_3$

Other effects, such as poor contact between rigid solid electrolyte materials and cathode materials can also lead to high interfacial resistivities in solid state batteries. This situation can be further aggravated as the electrodes often experience a large volume change during charge and discharge.[54,55] Building a flexible solid state electrolyte,[56] bringing up a new design of a battery[57], or developing a oxide coating layer on the cathode surface to stable the cathode structure and enable better contact[58] have been considered as the possible solutions to this problem.

CHAPTER 2. ORIGIN OF HIGH INTERFACIAL RESISTANCES IN SOLID-STATE BATTERIES: INTERDIFFUSION AND AMORPHOUS FILM FORMATION IN LLTO/LMO HALF CELLS

This chapter is based on the work published in "Pengyu Xu, Wolfgang Rheinheimer, Shoumya Nandy Shuvo, Zhimin Qi, Or Levit, Haiyan Wang, Yair Ein-Eli, Lia A. Stanciu. Origin of High Interfacial Resistances in Solid- State Batteries: Interdiffusion and Amorphous Film Formation in $Li_{0.33}La_{0.57}TiO_3/LiMn_2O_4$ Half Cells[J]. ChemElectroChem, 2019, 6(17): 4576-4585."

2.1 Introduction

All-solid-state lithium ion batteries have been regarded as promising power sources for electric vehicles (EVs)[2–4]. By replacing flammable organic liquid electrolytes with non-flammable solid electrolytes (SEs), solid state batteries (SSBs) are projected to solve the safety issues of traditional lithium-ion batteries.[5,6] Moreover, solid electrolytes typically provide broader electrochemical windows, which could enable the application of higher potential cathodes. By suppressing the dendrite formation, SEs also make the use of lithium metal anodes possible in batteries[7,8] , thus increasing the energy density of SSBs.

However, the poor ionic conductivity of SEs and the high interfacial resistance between SEs and electrodes are two drawbacks for solid state lithium ion batteries, which could lead to low power density and poor cycling performance of SSBs.[10] Recently, great progress has been made in improving the ionic conductivity of SEs. Kanno's group reported a lithium superionic conductor $Li_{10}GeP_2S_{12}$ with ionic conductivity of 10^{-2} S/cm[11], which is comparable to a liquid electrolyte. At the same time, perovskite[19], NASICON-like[59] and garnet type[60] solid electrolytes were also reported to reach ionic conductivities of about 10^{-3} S/cm at the room temperature[18]. On the other hand, the large interfacial resistance between electrode and electrolyte could lead to large internal resistance of the battery and result in a loss of energy and power density[61]. However, interfacial phenomena between electrodes and electrolyte in SSBs are still not well-understood. Formation of interelectrode films[32,62], space-charge layers [49,63] and contact loss due to electrode deformation during cycling[64] are potential reasons for the large interfacial resistance. Among these, the interphase formation at the cathode/electrolyte interface during charging has been observed experimentally by Sakuda[52] and theoretically testified by Ceder's group[7]. Studying the formation

mechanisms of the interphase and investigating its effect on ionic conductivity is the first step towards engineering structurally stable SSBs.

At the same time, co-sintering experiments have been widely applied to investigate possible interfacial reactions between oxide electrolyte/electrode combinations[61,65–67], where the compatibility of garnet-like electrolyte[68] and Lithium Aluminum Titanium Phosphate (LATP)[61] against common cathode materials has been investigated. However, there is still a lack of research on the compatibility of perovskite electrolytes against cathode materials. Interphase formation occurs during co-sintering by an interdiffusion between both materials involved. Based on such experiments, this work evaluates the feasibility of a pair of model cathode/electrolyte ceramics for SSB applications. Lithium Lanthanum Titanite ($Li_{0.33}La_{0.57}TiO_3$, LLTO) is a perovskite electrolyte with a high bulk ionic conductivity of 10^{-3} S/cm at room temperature[19]. LLTO is stable in air, tolerates humidity and does not release any toxic gases as a result of chemical decomposition in contrast to sulfide electrolytes[66]. In addition, LLTO has good high temperature stability and is reported to be stable against high voltage cathodes[20,21]. Therefore, LLTO is a promising SE candidate in SSBs. However, its high grain boundary resistance and instability against low potential anodes are challenges that LLTO would face as a solid electrolyte in a battery[69]. Lithium Manganese Oxide ($LiMn_2O_4$, LMO) is a popular spinel cathode material, and it has been considered as the best candidate replacing e.g. lithium cobalt oxide ($LiCoO_2$) because of the abundancy of manganese in nature and its low toxicity level.[70,71]

Spark plasma sintering (SPS) is an advanced sintering method that utilizes uniaxial pressure and a pulsed DC current to consolidate powders with high sintering rates[72], and can thus be an appropriate technique to use for the sintering of SSB half cells. As mechanical pressure adds to the driving force for sintering and direct heating allows for very high heating rates, lower processing temperatures and shorter sintering times can be achieved, which can reduce particle coarsening greatly[73]. At the same time, the short sintering times can alleviate the formation of interphase, which is beneficial for batteries. The possibility of applying SPS to produce a laminar cathode/electrolyte/anode SSB has been brought to light according to the time-saving and good interfacial contact promised by this technique[74,75].

As future SSBs need a functioning interphase layer without the development of large resistances, a careful choice of chemistries and processing parameters is needed. Any computational study of the interphase formation will need experimental input on the interdiffusion

and phases that are being formed in the contact area. So far, no information is available for the interphase formation for the half-cell pair LLTO/LMO. Therefore, in this work, we co-sintered LLTO and LMO via both SPS and conventional sintering to understand their benefits as processing methods for the investigation of cathode/electrolyte interphase formation. We used scanning Electron Microscopy (SEM), High Resolution Transmission Electron Microscopy (HRTEM), Scanning Transmission Electron Microscopy (STEM) and Energy Dispersive X-ray spectroscopy (EDS) as characterization methods of the cathode/electrolyte interphase. Additionally, we analyzed the effect of the interphase formation on the overall conductivity by Electrochemical impedance spectroscopy (EIS).

2.2 Experimental

Powder synthesis: $Li_{0.33}La_{0.57}TiO_3$ (LLTO) was synthesized by solid state reaction. Li_2CO_3 (Sigma-Aldrich, ≥99%), La_2O_3 (Sigma-Aldrich, ≥99.9%) and TiO_2 (Rutile, Sigma-Aldrich, ≥99.9%, <5 μm particle size) were mixed according to stoichiometry in an attrition mill. The mixed powders were dried and calcined in a tube furnace at 1050°C for 6 hours to allow a solid-state reaction to the perovskite phase. The LLTO powders were attrition milled again for 2 hours to break agglomeration formed during calcination. The powder was characterized by XRD and SEM.

The cathode material, $LiMn_2O_4$ (LMO) is commercially available from Sigma Aldrich (>99%, <0.5 μm particle size).

Pellets for Sintering: LLTO and LMO powders were co-pressed axially into a layered pellet as shown in Figure 2.1 (a). LMO powders were pressed into a green pellet at 80 MPa for 1 minute. Subsequently, the same volume of LLTO powder was added and again pressed at 80MPa for 1 minute.

SPS and Conventional Co-sintering

Figure 2.1 (b) shows a co-pressed pellet sintered by a Thermal Technology SPS 10-3 machine. The SPS experiment was carried out at 50 MPa and 900°C for 10 minutes. The heating and cooling rate were 100 °C/ min. The co-sintered pellet was cut and embedded in epoxy. The cross-section was polished with SiC paper and diamond slurry (final particle size of 1μm).

Figure 2.1 (c) shows a co-pressed pellet after conventional sintering at 900°C in a tube furnace for 4 hours in Ar atmosphere. The pellet was cut and embedded in epoxy and the cross-section was polished similarly to the SPS sample.

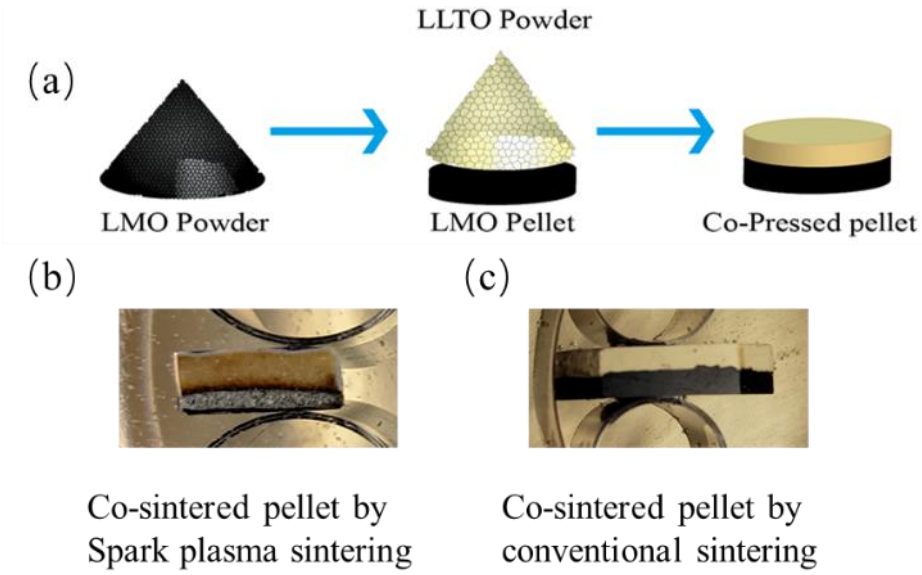

Figure 2.1 （a）Procedure for the fabrication of co-pressed pellets (b) co-pressed pellet sintered by spark plasma sintering (SPS), embedded in epoxy and polished. (c) co-pressed pellet sintered by conventional sintering, embedded in epoxy and polished

Materials Characterization

Scanning Electron Microscopy (SEM) and X-ray diffraction (XRD) were applied to characterize the LLTO powders. To evaluate a possible reaction between LLTO and LMO, both powders were mixed together with a volume ratio of 1:1 with a mortar and pestle. The mixture of electrolyte and cathode powders were pressed into pellets under a pressure of 100MPa. Pellets were heated to 900°C in Ar atmosphere for 4 hours. A subsequent XRD analysis (Bruker D8 Focus, 2θ =15° to 80°) was applied to identify the resulting phases.

For all pellets prepared by conventional sintering and spark plasma sintering, microstructures of interfacial regions have been investigated by SEM (FEI Quanta 650). EDS mapping and line scans (EDAX and Oxford Instruments) have also been applied to detect elemental distribution in the interfacial region. For the SPS sintered pellets, TEM lamellas with a width of 10-20µm were cut from the interfacial using a Focused Ion Beam microscope (FIB, FEI

Quanta 3D). HRTEM, STEM and EDS have also been applied to characterize the microstructure and chemistry using a FEI Talos 200X TEM.

Electrochemical impedance spectroscopy (EIS) was applied to the SPS co-sintered pellet, a pure LLTO pellet and a pure LMO pellet to characterize the effect of interfacial layer on overall resistivity with a BioLogic electrochemistry potentiostat in the frequency range of 1MHz to 1Hz. The measurement voltage was 100mV.

2.3 Results & Discussion

Powder characterization and phase composition

According to SEM images showed in Figure 2.2(a), the particle size of the powder precursors is in the order of 500nm. The XRD spectrum of LLTO is shown in Figure 2.2 (b), and matches the standard PDF card JCPDS No.870935, which underlines the phase purity of the synthesized $Li_{0.33}La_{0.57}TiO_3$.

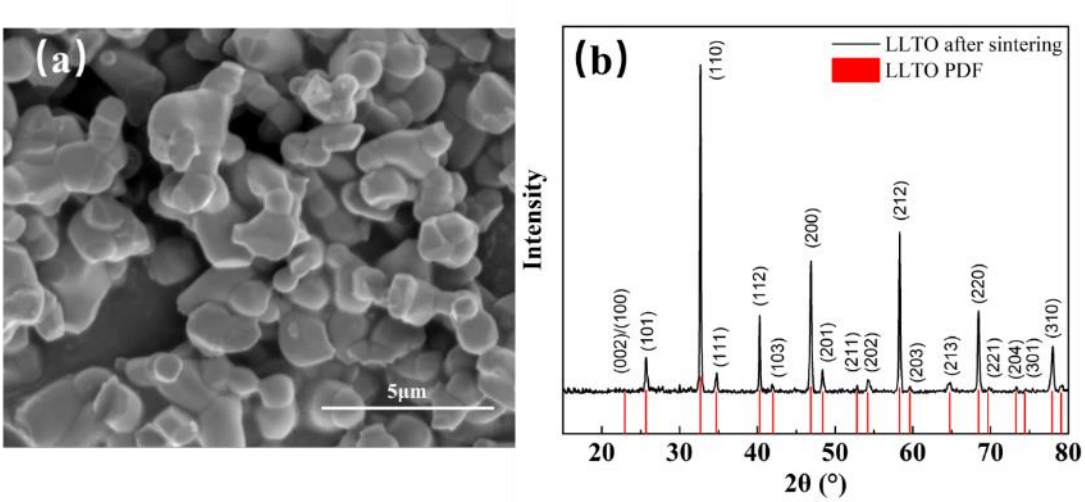

Figure 2.2 (a) SEM images of LLTO powders synthesized by solid state method, (b) XRD data of the LLTO powders compared with standard PDF card JCPDS No.870935

The XRD analysis of the individual LMO and LLTO, as well as the mixed LMO/LLTO pellets after heating to 900°C for 4h are shown in Figure 2.3. Comparing the pattern of the mixed pellet to the LLTO and LMO powders, no additional peak is visible in the mixed pellet profile. Accordingly, there is no significant chemical reaction or phase formation during conventional co-

sintering of LLTO and LMO powders. However, this result does not indicate that there is no interphase formation at the interface between LLTO and LMO after sintering. Merely, the XRD results show that in each of the individual bulk phases, there are no phase transformations or chemical reactions up to 900°C. A potential interphase formation would fall below the detection limit of the XRD.

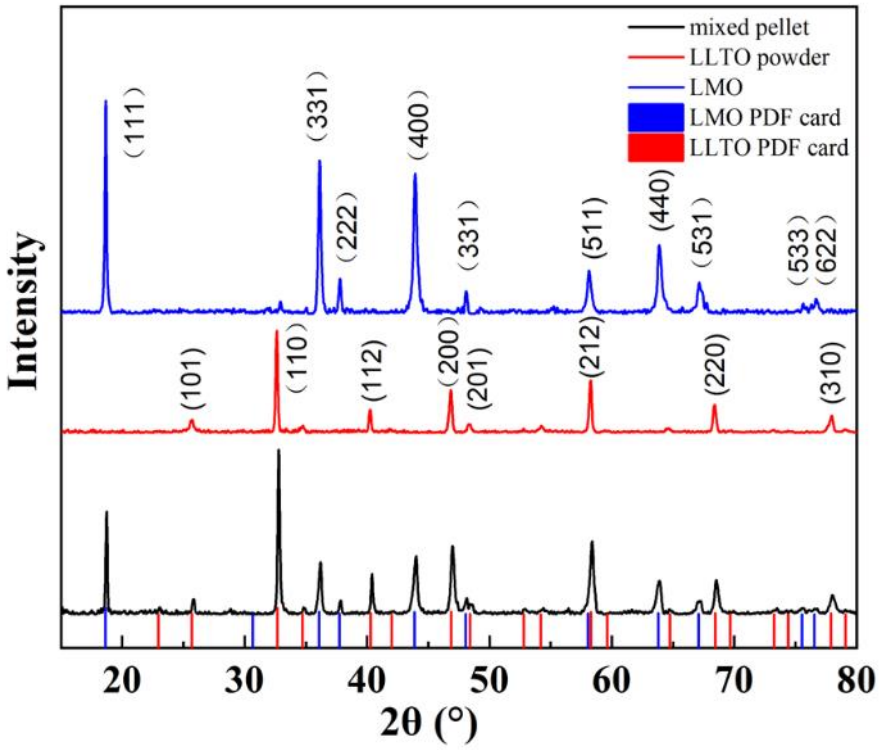

Figure 2.3 XRD patterns of $Li_{0.33}La_{0.57}TiO_3$ (LLTO), $LiMn_2O_4$(LMO), and LLTO+LMO powder mixture pellet heated to 900°C for 4h compared with standard PDF cards.

Electron Microscopy Characterization of Conventionally Sintered Sample

Analytical SEM and TEM has been widely applied in the investigation of interphases. Interdiffusion can be easily identified by concentration gradients in the EDS data[76]. In solid state batteries, Han[64] observed an interphase formed by interdiffusion between LCO and LLZO via SEM and EDS mapping, and Kim[53] detected the similar interdiffusion via TEM and EDS line scan. In high resolution TEM or STEM, the interphase could be observed directly by the difference in atomic mass (Z contrast). Sakuda[52] observed a clear interphase formed between LCO and Li_2S-

P_2S_5 via HAADF mode in STEM. In the present study, both the interdiffusion and interphase formation were investigated. The thickness of the interdiffusion layer could be only estimated due to the uncertainty of the EDS data and the asymptotic shape of the diffusion profile. A better quantification of interdiffusion can only be achieved if a computational modelling approach is used that incorporates thermodynamic details of eventually occurring phase transitions. This is beyond the scope of the present study.

To investigate the impact of the sintering, the conventionally sintered half- cell from Figure 2.1(c) was analyzed by SEM and EDS as shown in Figure 2.4. According to Figure 2.4 (a), conventionally sintering at 900°C for 4 hours did not fully densify LLTO and LMO. The interfacial region did not have a good contact as voids are visible along the interfacial region (red circle). The SEM-EDS results in Figure 2.4(c) indicate that significant interdiffusion between Mn and Ti occurred, while for La less interdiffusion is evident. In Mn and Ti mappings (Figure 2.4(a)), a clear diffusion of Mn and Ti ions across the interface is visible. However, the La concentration in the LMO phase was below the method detection limit. Accordingly, the La ions are much less involved in the interdiffusion compared to Ti and Mn ions. However, as best illustrated by the high concentration of Mn on the left end of the line scan in Figure 2.4 (c) (i.e. in the LLTO), the true diffusion distances for Mn, Ti and La ions are greater than the scanned length in Figure 2.4 (b). Therefore, line scans at boarder scales have been applied (Figure 2.9). The diffusion distances for Mn, Ti and La ions are roughly in the order of 300µm. However, we did not detect any evidence for a second phase formation within this 300µm thick interdiffusion layer.

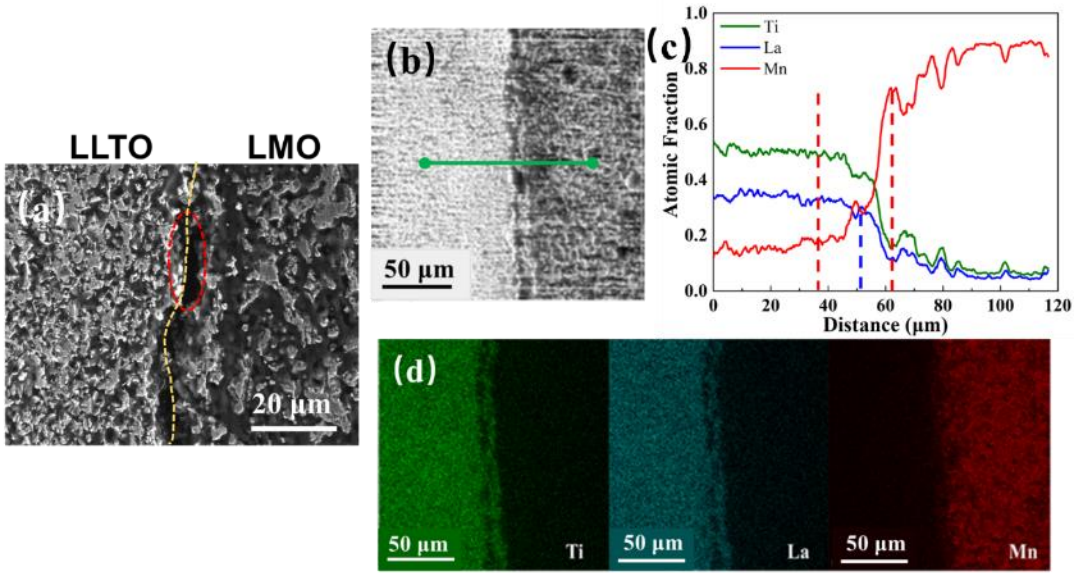

Figure 2.4 (a) Cross-sectional SEM image of the conventional sintered sample. (b) SEM image of the analysis region (c) Atomic fraction profile obtained by EDS line scan across the green line in (b), from left to right. (d) Element distribution profile in region (b), obtained by EDS mapping

Electron Microscopy Characterization of SPS Sample

We compared the SEM images of the cross-sections of SPS sintered LLTO/LMO and conventionally sintered LLTO/LMO (Figure 2.4(a) and Figure 2.5(a)). The interfacial regions were investigated by EDS to analyze the interdiffusion (Figures 2.4 and 2.5). Interdiffusion layer widths were estimated based on the EDS data.

The SEM overview of the interfacial region of the SPS sample is shown in Fig. 5(a). Both materials were sintered to very high density (>98%). The interface between LLTO and LMO shows a roughly 5 µm thick two-phase layer which was analyzed in detail by TEM-EDS as discussed further below. The interfacial region was further investigated by EDS line scan and mapping in Figure 2.5 (b) and (c). In the EDS line scan in Figure 2.5(b), concentration gradients were observed in the same region shown in Figure 2.5(a). Again, it is evident that for La, much less interdiffusion occurred compared to Mn and Ti. This agrees well with the EDS mapping shown in Figure 2.4(c). In the Ti mapping, we observed an obvious Ti diffusion into the LMO, and similarly, manganese was also detected in the LLTO. On the other hand, La was not detected in the LMO. Similar to the conventionally sintered sample, the interdiffusion layer width is in the order of 100-300µm and much larger than our scan length in Figure 2.5(b) (see Figure 2.10). No

evidence for a second phase was found in the line scan despite the intercalated morphology of the two-phase layer. These results on interdiffusion in the SPS sample are very similar to those of the conventionally sintered sample. Thus, the interphase formation does not depend on the sintering technique, and an interphase containing Mn, Ti and O (and probably Li) always forms at the LLTO/LMO interface during sintering.

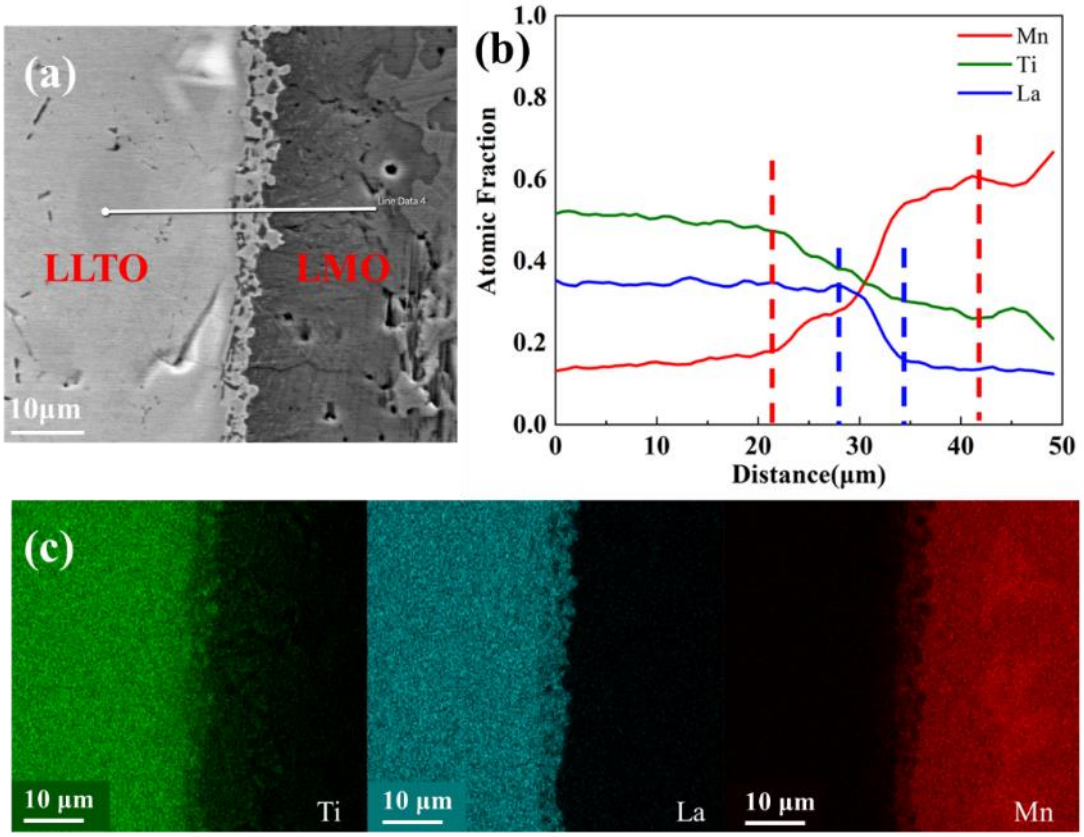

Figure 2.5 (a) Cross-sectional SEM image of SPS sintered sample. (b) Atomic fraction profile across the white line (from left to right) in (a), obtained by EDS line scan. (c) Element distribution profile of the region shown in (a), obtained by EDS mapping.

By comparing the interfaces of the two samples, we have an intuitive understanding of the advantage of SPS over conventional sintering in battery processing. SPS densifies the LLTO/LMO layered samples better and results in better interfacial contact. This is mostly the effect of the pressure applied during sintering, as well as the electrical field effects that have been proven in literature to accelerate diffusion responsible for materials densification, especially in cases when,

like in this work, there is a chemical potential difference present in the sample. The rapid heating rate of 100°C/min employed in the SPS sintering experiment presented here has also been shown to reduce grain growth during sintering, by bypassing the initial sintering stage where coarsening mechanisms are consuming driving force for densification[77]. Moreover, the pressure and the diffusion acceleration due to electrical field[73] also improves the contact between electrode/electrolyte, thus reducing the internal resistance of the SSBs.

To further confirm our results at higher resolution and particularly to investigate the two-phase layer observed in Figure 2.5 (a), a 20μm × 8μm rectangular lamella was cut and lifted out from the interfacial region by FIB (Focused Ion Beam, Figure 2.6 (a)). The lamella was thinned to 100nm thickness and analyzed by high angle angular dark field (HAADF-STEM), and STEM-EDS in Figure 2.6 (b) and (c). According to the Z-contrast of STEM-HAADF and the analysis of electron diffraction and EDS area scan results discussed in Figure 2.7, we identified the brighter phase as LLTO and the darker phase as LMO. According to the needle-like structure of these two phases, it is likely that during sintering at high temperature the region in blue circle in Figure 2.6(a) was a single phase that either decomposed due to decreasing solubilities or a phase transition during cooling. The EDS mapping in Figure 2.6(c) confirmed that in the "mixture region", both Ti and Mn are present, while La was again not detected. A needle-like distribution of Mn becomes evident, analogue to the microstructure in Figure 2.6(b). Figure 2.6 (d) and (e) provided a higher resolution mapping of this "needle-like" region. The upper third containing a bright phase in (d) is LLTO, while the darker region below contains two different phases with different contrast. These two phases (I, II) are different in Mn concentration with more Mn in brighter regions (I). We also observed a segregation of Mn around the Mn-deficient regions as indicated by a white arrow. Overall, the Ti concentration exhibited a distribution that is inverse to Mn, though at a lower extent.

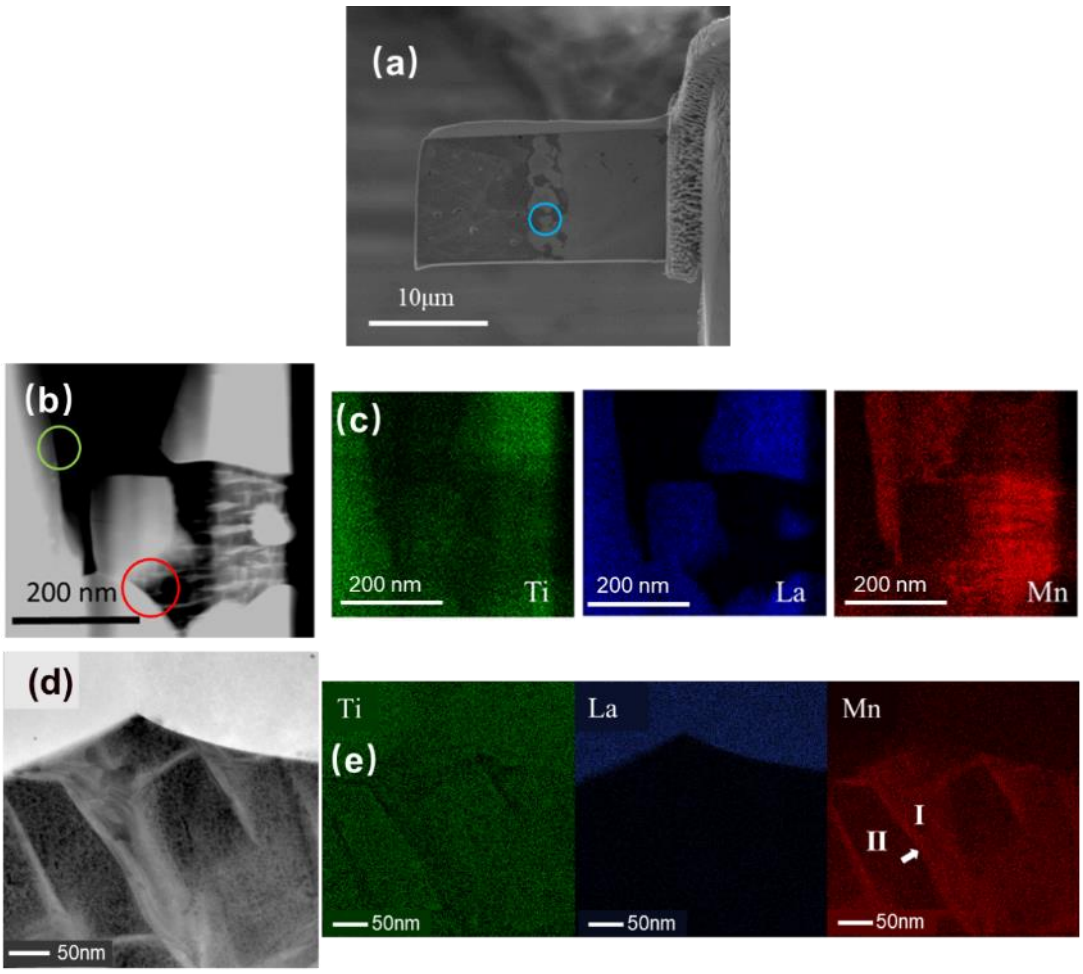

Figure 2.6 (a) Interfacial region obtained by focused ion beam (FIB) and lift-out. (b) STEM image of the circled region in (a). (c) Element distribution profile of (b) obtained by EDS mapping. (d) HAADF image of red circled region in (b). (e) Element distribution profile of (d), obtained by EDS mapping.

To fully understand the phases present in the two-phase layer shown in Figure 2.5 and 2.6, selected area electron diffraction (SEAD) and EDS area scans have been performed. As mentioned in Figure 2.6 (b) and (e), in the two-phase region, a needle-like phase distribution is evident. However, because the scale of these two phases (I, II) is in the nanometer region, the collected electron diffraction patterns are distorted. The SAED pattern in that area is shown in the Figure 2.7 below. Figure 2.7(b) shows the SAED pattern of the region shown in the bright field image in Figure 2.7(a). The pattern in Figure 2.7(b) matches the standard diffraction pattern for an FCC lattice in the [110] zone. The calculated lattice parameter is 0.853nm. The lattice parameter of spinel $LiMn_2O_4$ (space group Fd3m) is 0.83nm according to the database (JCPDS 35-0782). Given

that the pattern in Figure 2.7(b) is distorted to some extent, these two numbers are reasonably close, and it can be speculated that the phases shown in Figure 2.7(a) have an LMO lattice. EDS area scans have also been applied to the regions marked in Figure 2.7(c), and the results are summarized in Table 2.1. In Area 1, the atomic percentage of Mn and Ti together is 22.86 (Table 1; both are assumed to occupy the same lattice site in the hosting LLTO lattice). Accordingly, the atomic percentage ratio of La and "Mn+Ti" is 0.67, which is close to the La/Ti ratio in pure LLTO. Therefore, Area 1 appears to be LLTO phase which dissolved Mn. In Area 2 and Area 3, as we discussed with Figure 2.7(b), these two areas both are likely to have an LMO lattice, with different extent of Ti diffusion. Similar to the results in Figure 2.6(e), phase I has a higher Mn content than phase II, and both phases did not contain significant amounts of La. In Area 3 (phase I), the Mn/Ti ratio is 6.6 and in Area 2 (phase II) the Mn/Ti ratio is 2.67. This doesn't match the stoichiometry of any phase containing Li, Mn, Ti and O in the JCPDS database. As such, the identity of the phases present in the two-phase layer in Figure 2.5 and 2.6 is not completely clear, but it is likely that it could be composed of LLTO and LMO, while the latter decomposed into two different Mn/Ti ratios with the same hosting lattice (phases I and II). This is in good agreement with the SAED data and the powder mixture experiment, where an XRD investigation did not indicate the occurrence of any phases different from LLTO and LMO (see Figure 2.3).

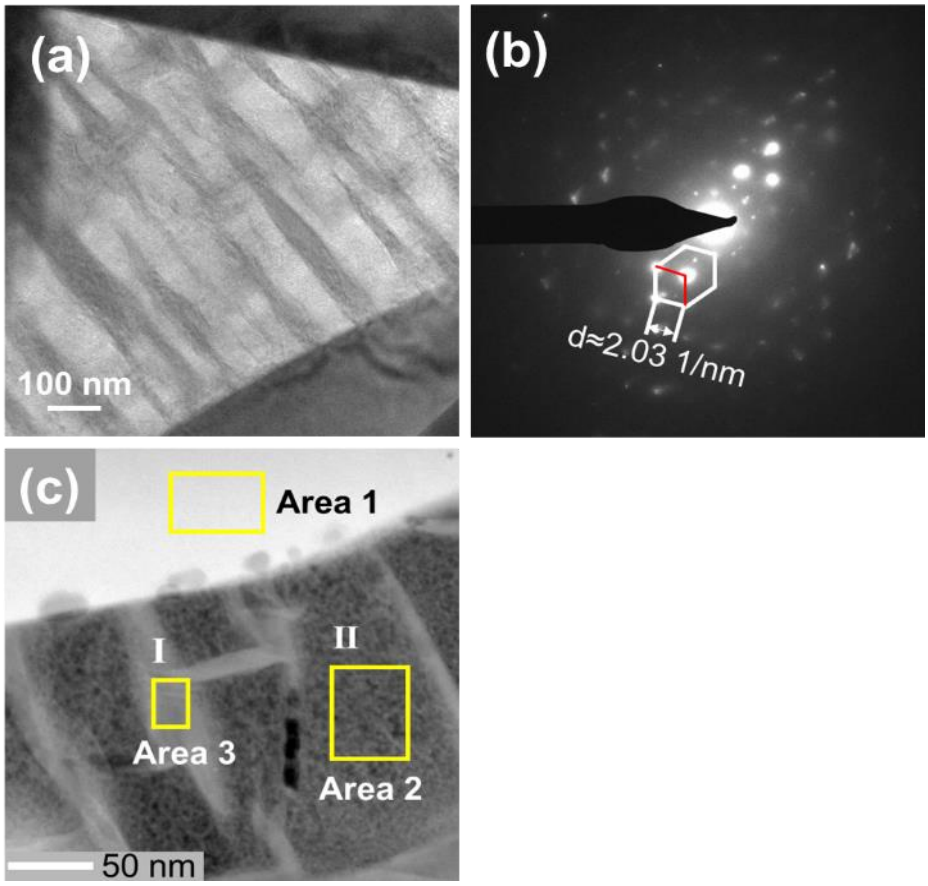

Figure 2.7 (a) Bright field TEM image of a Mn rich needle-like region. (b) SEAD pattern of area in (a). (c) HAADF image of a region like Figure 2.6 (d), EDS area scans were applied to this region. Phase I and Phase II are consistent with the Mn rich phases discussed in Figure 2.6 (e)

Table 2.1 Element distribution profile of areas in Figure 2.7(c)

Area	Element	Atomic percentage (%)
Area 1	O	61.75
	Ti	10.61
	Mn	12.25
	La	15.39
Area 2	O	67.5
	Ti	8.62
	Mn	22.99
	La	0.89
Area 3	O	60.66
	Ti	5.00
	Mn	32.99
	La	1.35

Figure 2.8 shows a high resolution TEM (HRTEM) image of the green circled region in Figure 2.6(b) where LMO and LLTO are in direct contact. According to this micrograph, an amorphous layer is present at the interface. The thickness of this layer is between 3 and 10 nm as the tilting angle of this layer is not known. Such amorphous films at interfaces are known as complexions[78,79] and are known to occur in various battery materials. [80–83] The complexion is a two-dimensional interfacial phase that is stabilized by its impact on the grain boundary energy. Potentially it affects the ion transportation across the interface drastically.

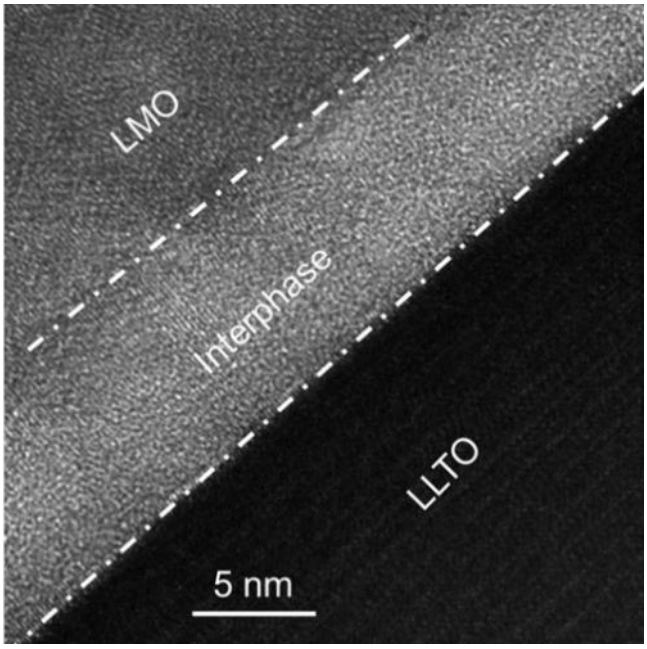

Figure 2.8 HRTEM image of the green circled region in Fig.6 (e).

In summary, at the LLTO/LMO interface, we observed two kinds of interphase. One is an interdiffusion layer with the thickness of tens or hundreds of microns, formed by the interdiffusion between manganese and titanium. The other is an amorphous complexion with the thickness of a few nanometers. The interface itself tends to form an intercalated structure where LMO and LLTO coexist. Based on the results above, the interphase between LLTO and LMO contains titanium, manganese and oxygen. Unfortunately, no information is available for lithium as it is not detectable by EDS. Electron Energy Loss Spectroscopy (EELS) is a technique that is sensitive for Li and could shed light on lithium presence and should be applied in future studies.

Chemical interdiffusion usually follows a substitutional diffusion mechanism. LLTO is a perovskite (ABO_3) type electrolyte, where the large La^{3+} cations occupy the A sites with a coordination number of 12. Ti^{4+} cations are located at the B sites with a coordination number of 6. LMO has a spinel structure (AB_2O_4), where Mn has a mixture 3^+ and 4^+ states. Mn occupies the B sites (octahedral interstitial) with a coordination number of six[84]. The ionic radii of these cations are 150pm (La^{3+}), 74.5pm (Ti^{4+}), 72pm (Mn^{3+}), and 67pm (Mn^{4+})[85]. In substitutional diffusion, a smaller difference in ionic sizes is likely to result in a smaller energy barrier for diffusion. As Ti^{4+} and Mn^{3+}/Mn^{4+} are very close in size and charge and the size of La^{3+} is much larger, it is reasonable that much less diffusion of La occurs, while Mn and Ti form extended interdiffusion layers with a thickness of 100 to 300µm.

Additional EDS information for conventional sintered LLTO/LMO sample:

To detail the interdiffusion of La, Ti and Mn (similar to Figure 2.4 (c)), longer line scans with lower resolution were applied to the conventionally sintered sample. According to Figure 2.9(b), the concentration of Mn in the LLTO drops below 10at% about 100µm away from the interface and below 5% about 500µm away from the interface. Below 5%, the accuracy of EDS might not allow significant quantification. Similar results are found for Ti and La, as a low concentration can still be found about 500µm away from the interface.

Furthermore, area scans had been applied to both LLTO and LMO 800 µm from the interface to study the element distribution far from the interface. The results are shown in Table 2.2. From this quantification, the concentration of Mn (La and Ti) in the LLTO (LMO) 800µm away from the interface is below the detection limit of EDS. Comparing this result with the line scans in Figure 2.9(b) and (c), it is apparent that the line scan somewhat overestimates the concentrations of Mn, La and Ti. As such, the true interdiffusion length is hard to estimate based on the presented EDS data, but certainly is in the order of 300µm for Mn into LLTO and about 200 µm for Ti into the LMO. Diffusion of La into the LMO occurs at a scale of 100µm.

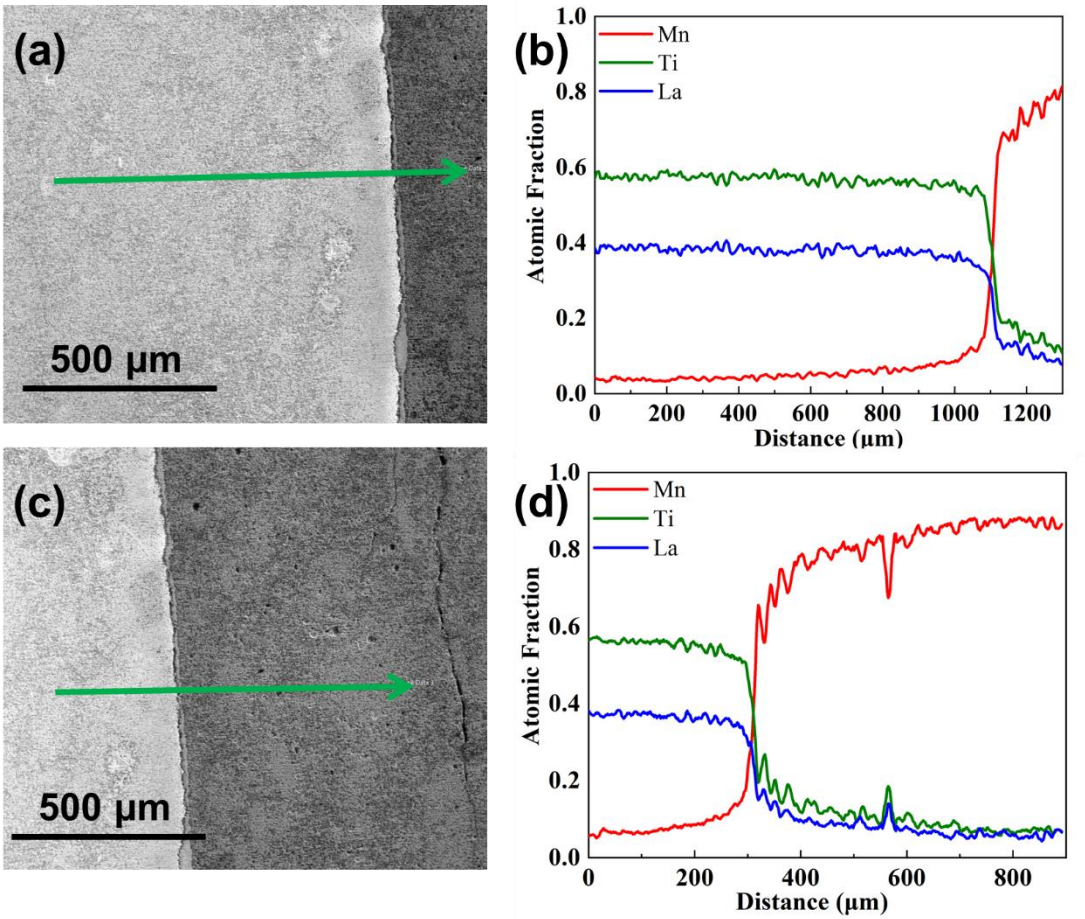

Figure 2.9 (a) SEM image of the analysis region. (b) Atomic fraction profile obtained by EDS line scan across the green line in (a), from left to right. (c) SEM image of analysis region. (d) Atomic fraction profile obtained by EDS line scan across the green line in (c), from left to right

Table 2.2 EDS area scan results for area 1 (LLTO phase) and area 2 (LMO phase).

LLTO	element	C	O	Si	Cl	Ti	Mn	Fe	La
	at%	54.57	29.98	0.12	0.1	9.39	0.3	0.16	5.38
LMO	element	C	O	Si	Cl	Ti	Mn	Fe	La
	at%	50.74	34.82	0.09	0.08	0.23	13.55	0.29	0.14

Additional EDS information for SPS sintered sample

Similarly, for SPS sintered sample, an additional EDS line scan was applied to gain more information on interdiffusion (Figure 2.10). Again, area scans have been applied to LLTO and LMO 400µm from the interface. Results are shown in Table 2.3. Overall, the results are very similar to conventional sintering. The interdiffusion layers are slightly thinner than for conventional sintering.

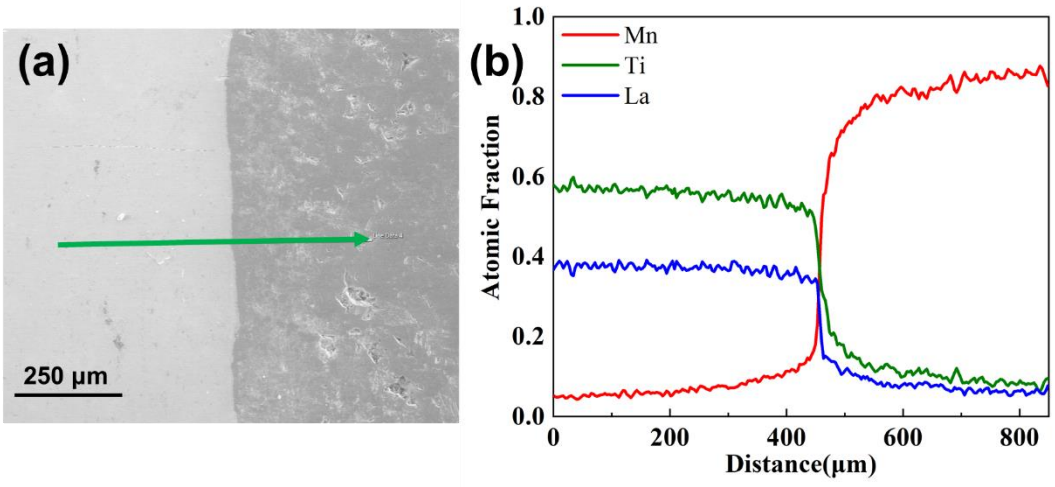

Figure 2.10 (a) SEM image of the analysis region. (b) Atomic fraction profile obtained by EDS line scan across the green line in (a), from left to right.

Table 2.3 EDS area scan for Area 3 (LLTO) and Area 4(LMO)

LLTO	element	C	O	Al	Si	Ca	Ti	Mn	La
	atomic%	5.91	60.79	0.17	0.13	0.06	20.22	1.03	11.69
LMO	element	C	O	Al	Si	Mn	Ti	La	
	atomic%	15.31	55.38	0.16	0.06	27.58	0.83	0.49	

Electrical Characterization of SPS Sample

In SSBs, the unwanted large interfacial resistance is likely to be caused by the interphase.[80] As the interphase layer is expected to have a high resistance, it can be identified with electrochemical impedance spectroscopy (EIS) as an additional part in the Nyquist plot, as reported in Koerver's work[32]. In general, separating individual contributions to the impedance of complex samples is challenging. In the present case, this is particularly true as the interphase even contains

two different layers (i.e. the interdiffusion layer and the amorphous phase). In the present work, we compared the impedance of LLTO/LMO composite with that of LLTO and of LMO to separate the impedance of the interphase layer. Figure 2.11 (a) shows the impedance profile of SPS sintered LLTO (900°C, 10 minutes, 50 MPa). In general, the overall resistance of LLTO can be divided into two parts, the LLTO grain impedance and the grain boundary impedance. The grain contribution usually occurs at higher frequencies than the grain boundary contribution. In addition, to the equivalent circuit in Figure 2.9 (a), a constant phase element was added to account for the electrode/LLTO contact capacitance.[86] By fitting the equivalent circuit (Figure 2.11 (a))and adding the two resistances R_{grain} and R_{GB} of the equivalent circuit (Table 2.4), the bulk resistance of LLTO was found to be approximately 12,000Ω. The overall ionic conductivity can be calculated through the equation $\sigma = \rho \frac{l}{s}$ and was found to be approximately 1.1×10^{-5} S/cm, which is comparable with data from the literature[19]. Figure 2.11 (b) shows the impedance of LMO. Given that LMO possesses both electronic and ionic conductivity, we applied the equivalent circuit in Figure 2.11 (b) [87] to fit the impedance data, and the fitting result was reasonable.

Figure 2.11 (c) shows the impedance profile of the LLTO/LMO SPS co-sintered pellet. As this sample is a series of LMO and LLTO, the respective equivalent should be a series of those used for LLTO and LMO in Figure 2.11 (a) and (b). For the interphase, at least one RC circuit should be added as shown in Figure 2.11 (e). However, this equivalent circuit results in a fitting function with 20 parameters which cannot be fitted to the data in a reasonable way. Accordingly, a simplified equivalent circuit (Figure 2.11 (c)) was performed, with the LMO, LLTO and interphase parts in series. As Figure 2.11 (c) shows, the fitting result still does not give usable information on the electric properties of the interphase. However, based on the fitted curve, we can estimate that the overall resistance of the co-sintered layered sample by adding the resistances of all three resistors in the equivalent circuit (Table 2.6). The estimated resistance of this interphase is about 1×10^{6} Ω, which is much larger than the individual resistances of LLTO and LMO as shown in Figure 2.11 (d). This much higher resistance is most likely caused by the formation of the interphase as discussed in the previous section. However, the specific resistance for this interphase could not be evaluated by the fitting procedure shown in Figure 2.11.

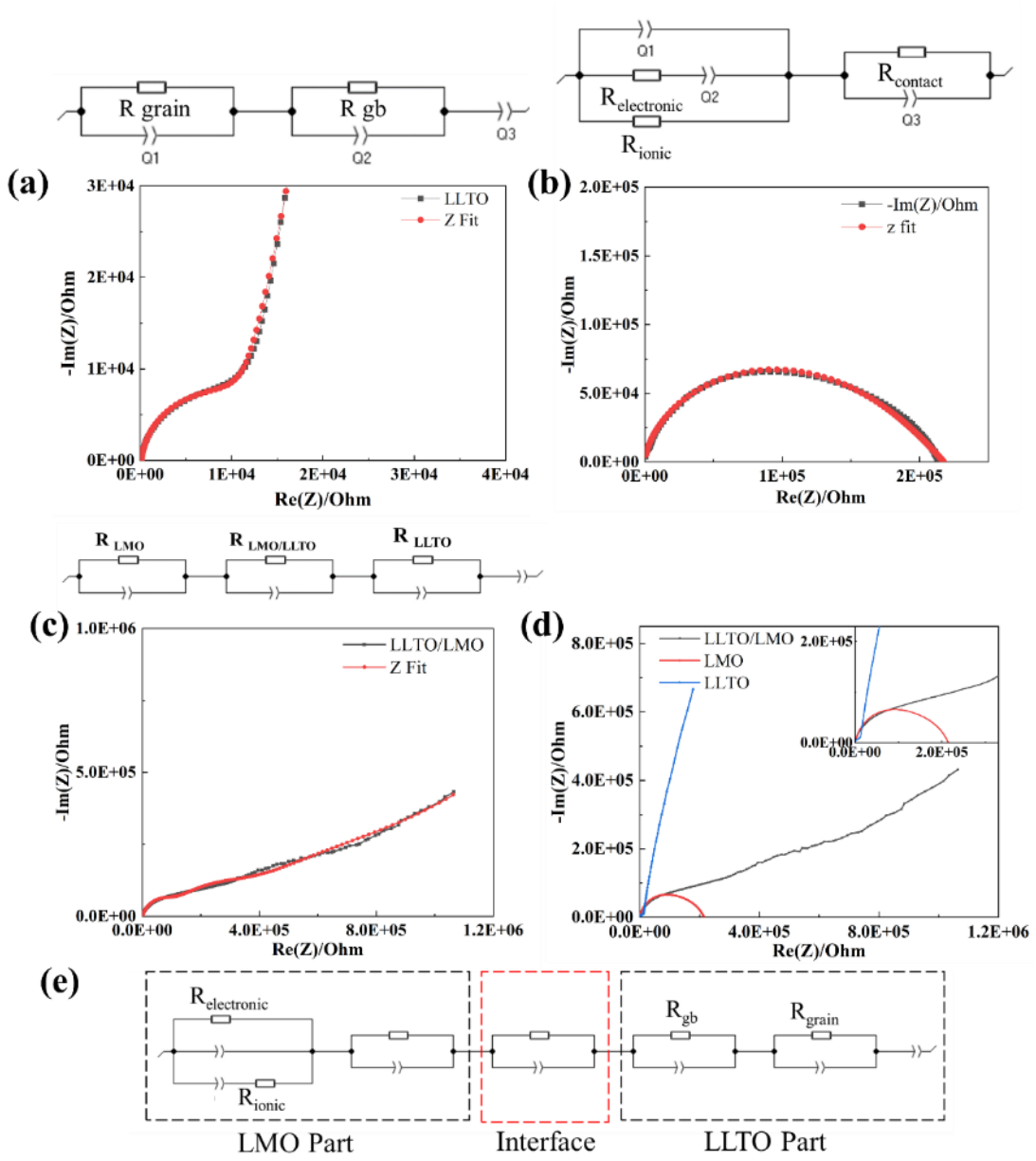

Figure 2.11 (a) The impedance profile of SPS sintered LLTO and the fitting result based on the equivalent circuit on the top. (b) The impedance profile of LMO and the fitting result base on equivalent circuit on the top. (c) The impedance profile of LLTO/LMO co-sintered by SPS and the fitted result based on the equivalent circuit on the top. (d) The overlaid impedance profiles of LLTO/LMO (black) LLTO (blue) and LMO (red). (e) Equivalent circuit of LLTO/LMO.

One way to approach the impedance of the interphase is to use the results from individual LLTO and LMO samples. As the LLTO/LMO is a series of these two materials with the interphase in between, the impedance of the interphase $Z_{interphase}$ corresponds to the difference between the individual impedances of LMO (Z_{LMO}) and LLTO (Z_{LLTO}) and the impedance of the LLTO/LMO ($Z_{LLTO/LMO}$) sample. Figure 2.12 (a) and (b) show a comparison of the measured $|Z|_{LLTO/LMO}$ (black curve) with the mathematical addition of $|Z|_{LMO}$ and $|Z|_{LLTO}$ (green curve). The gap between the black and green curve corresponds to a large interfacial resistance caused by the interphase. To analyze the impedance of the interphase, we estimated the imaginary part of interfacial impedance using the information on the impedance of separate LMO and LLTO samples:

$$Im(Z_{interphase})=Im(Z_{LLTO/LMO})-(Im(Z_{LLTO})+Im(Z_{LMO})). \quad (1)$$

Analogue, we estimate the real part of interfacial impedance by:

$$Re(Z_{interphase})=Re(Z_{LLTO/LMO})-(Re(Z_{LLTO})+Re(Z_{LMO})). \quad (2)$$

Subsequently, we plotted the Nyquist diagram ($-Im(Z_{interphase})$ vs $Re(Z_{interphase})$) from 10kHz to 5Hz as shown in Figure 2.12 (c). We have chosen this frequency range, as for higher frequencies, the difference between the black and green curve in Figure 2.12 (a) is negligible indicating that the impedance of the interphase is negligible as well in that frequency range. For frequencies lower than 5Hz, the impedance data contains too much noise as evident in Figure 2.11 (d). As the impedance of the interphase in Figure 2.12 (c) clearly contains two semicircles, we used an equivalent circuit with two RC elements which provided a reasonable fit. From this fit, we were able to get an approximation of the resistance of the interphase with $R_1= 1.36\times10^5\ \Omega$, $R_2=3.3\times10^5\ \Omega$, $Q_1=2.42\times10^{-9}$ F ($a_1=1$) and $Q_2=1.58\times10^{-8}$ F ($a_2=1$). Accordingly, the interphase resistance was found to be $4.66\times10^5\ \Omega$, which is about 40 times higher than the overall resistance of the LLTO sample.

As for both constant phase elements Q_1 and Q_2, it was found that $a_1 = a_2 = 1$, Q_1 and Q_2 directly correspond to a capacity. Using a plate capacitor approach, the capacity is $C = \epsilon_0\epsilon_r A/d$ with the permittivity of the vacuum ϵ_0, the relative permittivity ϵ_r, the cross-sectional area A and the layer thickness d. If we assume the relative permittivity to be in the order of 30 for

LLTO and LMO, a layer thicknesses of ~10µm for Q_1 and ~1µm for Q_2 is obtained. Considering the layer thicknesses known form electron microscopy for the interdiffusion layer (multiple tens to a few hundred µm) and the amorphous film (~5nm), the high resistance of the interface seems not to stem from the nm thick amorphous film. Instead, the impedance data indicates that the interdiffusion layer is causing the high interphase resistance. This result agrees well with the literature as nanometer thick amorphous layers are known to enhance the transport of Li for certain cathode materials[80,83,88].

Overall, our results confirm that the high interfacial resistance between electrodes and electrolyte will play an important negative role in the performance of all-solid-state batteries. This is a significant challenge in the field of all solid-state batteries, which has to be overcome by designing electrode/electrolyte pairs that are likely to bypass the formation of such interfacial layers with high resistance. In the light of the present study, research should focus particularly on hindering interdiffusion and not on preventing amorphous layer formation as the latter is not relevant for the high resistance of the interphase. Computational studies can help quantifying interdiffusion, aiding materials selection and finding new processing techniques that encourage densification while discouraging interdiffusion are key pathways toward overcoming this roadblock.

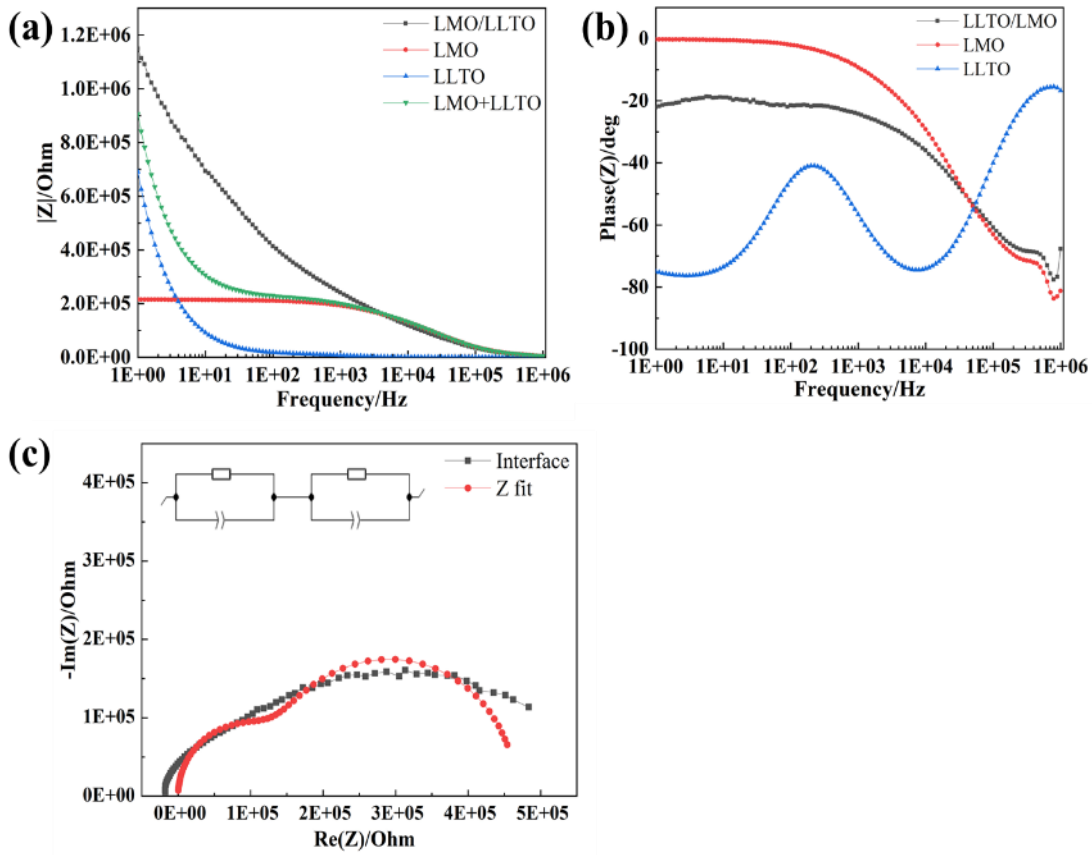

Figure 2.12 (a) plot of |Z| vs Frequency for LLTO/LMO (black), LMO (green), LLTO (blue), and the mathematical addition of LMO and LLTO. (b) Phase angle vs Frequency plot for LLTO/LMO, LLTO and LMO. (c) Nyquist plot of the interphase from 10kHz to 5 Hz, and the fitted curve based on the equivalent circuit above.

Additional Electrical characterization information

In the following, the fitting parameters of all impedance data as shown in Figure 2.8 and 2.9 are summarized.

1. Spark plasma sintered (SPS) LLTO (d=1cm, h=1mm)

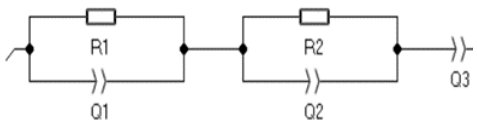

Figure 2.13 EDS area scan for Area 3 (LLTO) and Area 4(LMO)

We used the equivalent circuit as shown in Figure 2.13 to fit the impedance data. The fitting parameters are shown in Table 2.4

Table 2.4 Fitting parameters for SPS sintered LLTO

Parameter	Value	Unit
R1	10754	Ohm
Q1	3.994×10^{-8}	$F{\cdot}s^{a-1}$
a1	0.9339	
R2	125.8	Ohm
Q2	2×10^{-24}	$F{\cdot}s^{a-1}$
a2	0.1523	
Q3	0.2887×10^{-6}	$F{\cdot}s^{a-1}$
a3	0.8837	

2. SPS sintered LMO (d=1cm, h=1mm)

We used equivalent circuit as shown in Figure 2.14 to fit the impedance data. The fitting parameters are shown in Table 2.5.

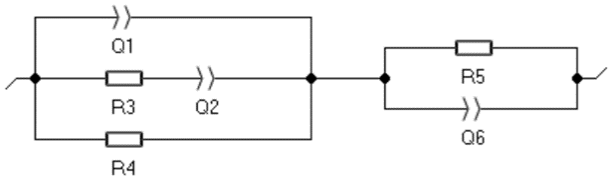

Figure 2.14 Equivalent circuit for SPS sintered LMO

Table 2.5 Fitting parameters for SPS sintered LMO

Parameter	Value	Unit
Q1	3.529×10^{-8}	$F{\cdot}s^{a-1}$
a1	0.8244	
R3	128.8	Ohm
Q2	1.253×10^{-5}	$F{\cdot}s^{a-1}$
a2	0.3428	
R4	149152	Ohm
R5	68008	Ohm
Q6	1.15×10^{-10}	$F{\cdot}s^{a-1}$
a6	0.9491	

3. SPS sintered LLTO/LMO (d= 1cm, each layer = 1mm)

We applied the equivalent circuit as shown in Figure 2.15 to fit the impedance data. The fitting results are shown in Table 2.6.

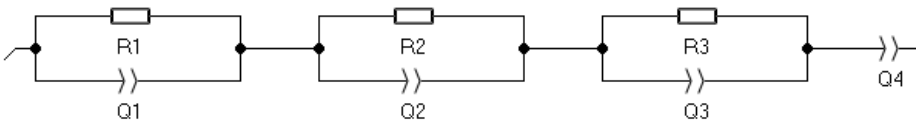

Figure 2.15 Equivalent circuit for SPS sintered LLTO/LMO

Table 2.6 Fitting parameters for SPS sintered LLTO/LMO

Parameter	Value	Unit
R1	87844	Ohm
Q1	2.14×10^{-10}	$F\cdot s^{a-1}$
a1	0.9132	
R2	247614	Ohm
Q2	1.63×10^{-8}	$F\cdot s^{a-1}$
a2	0.6689	
R3	623209	Ohm
Q3	2.47×10^{-7}	$F\cdot s^{a-1}$
a3	0.5396	
Q4	9.059×10^{-7}	$F\cdot s^{a-1}$
a4	0.5414	

4. Calculated impedance of the interphase layer

We used the equivalent circuit as shown in Figure 2.16 to fit the calculated impedance of the interphase layer. The fitting parameters are shown in Table 2.7.

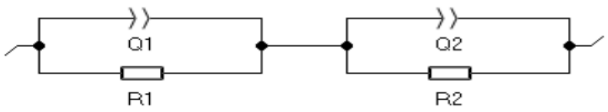

Figure 2.16 Equivalent circuit for the calculated interphase layer

Table 2.7 Fitting parameters for the interphase layer

Parameter	Value	Unit
Q1	2.42×10^{-9}	$F\cdot s^{a-1}$
a1	1	
R1	1.36×10^{5}	Ohm
Q2	1.58×10^{-8}	$F\cdot s^{a-1}$
a2	1	
R2	3.3×10^{5}	Ohm

2.4 Conclusions

The compatibility between the perovskite electrolyte material $Li_{0.33}La_{0.57}TiO_3$(LLTO) and the spinel cathode material $LiMn_2O_4$ (LMO) was studied with respect to the formation of interfacial phases and their effect on the conductivity. Co-sintering LLTO/LMO layered samples was done using both conventional sintering and spark plasma sintering (SPS). SPS sintering resulted in both denser samples and better interfacial contact. An amorphous complexion film was identified at the LLTO/ LMO interface by HRTEM. The interfacial phase and chemical composition were studied by analytical STEM and SEM and confirmed that the interphase contained manganese, titanium and oxygen. SAED confirmed that no additional bulk phase was present in the interphase layer. This is in good agreement to a simple powder mixture experiment, where no additional phases were found by XRD after a heat treatment. EIS characterization underlined that the formation of this interphase greatly reduces the ionic conductivity of the layered sample as the interfacial resistance is larger by a factor of about 40 compared to the sum of the individual phases. Interestingly, the amorphous layer at the grain boundary seems to not contribute to this high grain boundary resistance; the high impedance is only caused by the interdiffusion layer. Therefore, to improve the performance of SSBs, the focus should be on reducing the interdiffusion in the interphase and engineer the interphase towards enhanced ionic conduction performance.

CHAPTER 3. INTERPHASE FORMATION AND ANALYSIS FOR THE LITHIUM–ALUMINUM–TITANIUM–PHOSPHATE (LATP) AND LITHIUM–MANGANESE OXIDE SPINEL (LMO) HALF-CELLS

This chapter is based on the work published in "Or Levit, Pengyu Xu, Boris Shvartsev, Gal Avioz Cohen, Lia Stanciu, Yoed Tsur, and Yair Ein-Eli. Interphases Formation and Analysis at the Lithium–Aluminum–Titanium–Phosphate (LATP) and Lithium–Manganese Oxide Spinel (LMO) Interface during High- Temperature Bonding[J]. Energy Technology, 2020, 8(12): 2000634."

3.1 Introduction

As shown in previous chapters, the large interfacial resistance between solid-state ceramics electrolytes and electrodes in all solid state lithium ion batteries is a major bottleneck for their practical realization[91]. The insufficient contact between SE and electrodes[92], the space-charged layer effect[49] and formation of high resistance interphases[7] have all been cited as potential causes of undesirably high interfacial resistance. In this chapter, we present the results on research where we applied Spark-plasma sintering (SPS), which enables the densification of both cathode and electrolyte along with providing good interfacial contact, to LATP/LMO half-cell. Our prior results on the properties of LLTO/LMO half-cells proved that the interphase formation is a significant resource for interfacial resistance.

Here, a different material selection, namely Lithium-Aluminum-Titanium-Phosphate (LATP, $Li_{1.3}Al_{0.3}Ti_{1.7}(PO_4)_3$) as electrolyte material, and Lithium Manganese Oxide (LMO, $LiMn_2O_4$) as the cathode material have been investigated. The original work has been published as "Interphases Formation and Analysis at the Lithium–Aluminum–Titanium–Phosphate (LATP) and Lithium–Manganese Oxide Spinel (LMO) Interface during High-Temperature Bonding"[93] in Energy Technology. In this study, LATP/LMO half cell have been fabricated via two different SPS processes as shown in Figure 3. The microstructure of interface regions have been characterized by SEM and the interfacial resistance have been analyzed by EIS.

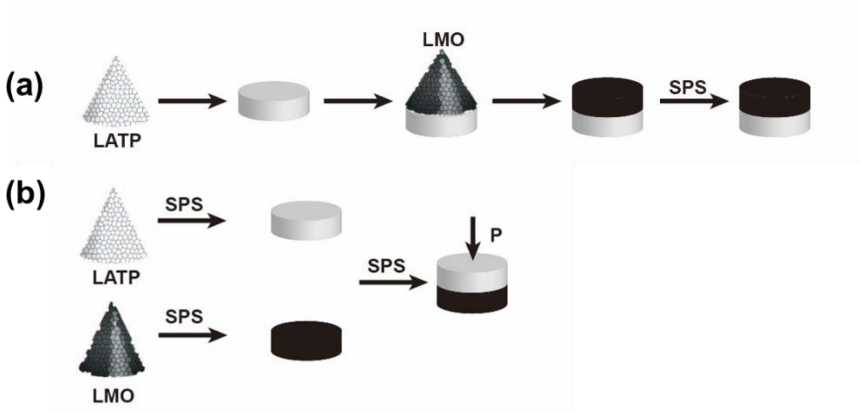

Figure 3.1 (a) Procedure for the one-step co-sintering experiment. (b) Procedure for the two-step joining experiment. [93]

Experimental

For the one-step co-sintering half-cell preparation showed as Figure 3.1(a), 0.45g LATP powders are first loaded in a graphite die and pressed into a green pellet. Then, 0.36g LMO powders are loaded on the top of LATP green pellet and subsequently pressed into a co-pressed pellet. After that, co-pressed pellet sintered by SPS. We sintered the co-pressed pellet with 4 different SPS parameters as listed in Table 3.1.

For the two-step joining experiment showed as Figure 3.1(b), 0.45g LATP powders and 0.36g LMO powders are densified by SPS respectively. Pellets were sintered at 800℃, 50 MPa for 10 minutes with heating and cooling rate of 100℃/ min. Then the pellets were polished by an 800 Grit SiC paper to 1 mm thickness and loaded in a graphite die for a second joining step. Pre-sintered LATP and LMO pellets were bonded at 700℃, 20MPa for 10 mins with a heating rate of 100℃/min and cooling rate of 10℃/min.

Table 3.1 Processing parameters for co-sintering LATP/LMO half-cell. [93]

Process number	Heating rate (℃/ min)	Cooling rate (℃/ min)	Temperature (℃)	Pressure (MPa)	Dewell Time (min)	Final Thickness (mm)
1	100	100	800	50	10	2
2	100	75	800	50	10	2
3	75	75	800	50	10	2
4	75	75	750	50	10	2

Electrochemical Impedance Spectroscopy (EIS) has been applied to characterize the interfacial resistance and the interphase resistance can be analyzed through the fitting of EIS data.

3.2 Results and discussion

The LATP and LMO pellets were densified by SPS at 800℃, 50MPa for 10 minutes with a heating and cooling rate of 100℃/ min. The sintered pellets reached densities of >95%. Then impedance of sintered LATP and LMO are measured, respectively. Results are shown in Figure 3.2[93]. For the fitting of LATP (Figure 3.2 (a)), we applied an equivalent circuit including two RC circuits, one accounts for LATP bulk impedance and the other accounts for the charge transfer at the surface. From the fitting result, R_1=4.3kΩ and R_2=9.6kΩ[93]. A similar approach has been applied for the fitting of LMO (Figure 3.2(b)). In the equivalent circuit, R_1 represents electronic conductivity of LMO particles and R_2 represents the ionic conductivity of LMO. From the fitting result, R_1=7.6MΩ and R_2=1MΩ. Comparing the impedance data of LATP and LMO, the impedance of LMO is significantly greater than LATP in the whole frequency range, as a result, we neglect the contribution of LATP phase in the analysis of half-cell impedance data.

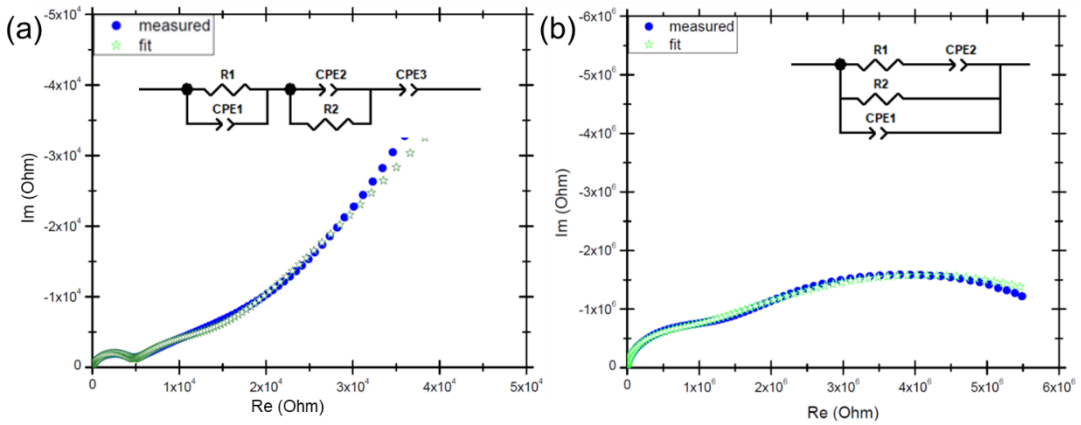

Figure 3.2. (a) Nyquist plot of SPS densified LLTO. Equivalent circuit model is applied for the fitting. (b) Nyquist plot of SPS densified LMO. Equivalent circuit model is applied for the fitting

For the characterization of co-sintered LATP/LMO half-cell, 4 different processing parameters have been applied (Table 3.1). For process 1, in which the half-cell is co-sintered at 800℃, 50MPa for 10 minutes with a heating rate of 100℃/min and cooling rate of 100℃/min.

The interfacial microstructure and impedance analysis results are shown in Figure 3.3(a)(b) and Figure 3.4(a). Based on interfacial microstructure in Figure 3.3(a) and elemental mappings in Figure 3.3(b), we noticed that there is an interphase formed between LATP and LMO. From element mappings, it is evident that Mn and P do not exist in this 17 μm thick layer, and therefore we can state that this interphase is an Li-Ti-O compound (Li_yTiO_{2-x}). The lithium concentration information is not clear as Li is undetectable in EDS. We also noticed that agglomerations of Al^{3+} rich phase form near the LMO phase. Moreover, we observed big pores exist between LATP and interphase, indicating poor interfacial contact. The impedance profile of the half-cell densified by process 1 is shown in Figure 3.4(a). As mentioned in the previous paragraph, we neglected the contribution of LATP phase in the analysis of the half-cell impedance. We applied two RC circuits for the interface, one accounted for the interfacial contact and the other for the interphase impedance. In the fitting process, we kept the resistance for LMO phase (R_1, R_2) as constant, R_1=7.6MΩ and R_2=1MΩ. Then we got R_3=34.9 MΩ (interfacial contact) and R_4= 8.8 MΩ (interphase resistance). The interfacial contact resistance of 34.9 MΩ again verifies that the interfacial contact between the LATP and the interphase is not satisfactory in process 1.

For process 2, the half-cell is co-sintered at 800℃, 50MPa for 10 minutes, but with a slower cooling rate of 75°C/min. Based on the interfacial SEM image in Figure 3.3(c) and (d), the interphase thickness reduced to 7μm with slower cooling rate. This interphase is still a Li-Ti-O compound, and we can still notice agglomerations of Al rich phase near LMO bulk phase. The interfacial contact between the interphase and the LATP bulk phase has been improved in this process, as a slower cooling rate can help relieve the thermal stress at the interface. From impedance perspective, the Nyquist plot of the half-cell prepared by process 2 is shown in Figure 3.4(b), and a similar equivalent circuit is applied for fitting. After the analysis, we obtained values of R_3=2.4MΩ (interfacial contact) and R_4=0.2 MΩ (interphase). Based on these results, we can conclude that the impedance from the interfacial contact is greatly reduced as the contact is improved by using a slower cooling rate. Moreover, the impedance from the interphase is also reduced from 8.8MΩ to 0.2MΩ, as the interphase thickness decreased from 14 μm to 7 μm.

For process 3, the half-cell is co-sintered at 800℃, 50MPa for 10 minutes, with a heating rate of 75 ℃/min and cooling rate of 75 ℃/min to evaluate the effect of reduced heating rate on interphase formation. The interfacial microstructure and element mappings are shown in Figure 3.3(e) and (f). From Figure 3.3(e), we observe that the interphase (Li_yTiO_{2-x}) thickness is still 7

μm, while the contact between LATP and interphase deteriorates again. We still observed agglomerations of Al^{3+} rich phase; these clusters are a few microns away from the LMO phase, indicating that the slower heating rate allows a longer time for Al^{3+} to diffuse. The Nyquist plot of the half-cell prepared by process 3 is shown in Figure 3.4(c). Here, we still applied a similar equivalent circuit to analyze the impedance of the interphase. From the fitting, we obtained values of R_3 (interfacial contact) =13MΩ and R_4 (interphase) = 0.7MΩ. Based on this information, we can conclude that the interphase impedance is closely related to its thickness. A slower cooling rate will help relieve the interphase resistance, while a slower heating rate will only affect the Al^{3+} diffusion, which would not result in any changes in terms of impedance. However, the interfacial contact needs to be improved in order to reducing the interfacial resistance.

For process 4, the half-cell is sintered at 750°C, 50MPa for 10 minutes, with a heating rate of 75 °C/min and cooling rate of 75 °C/min, to evaluate the effect of process temperature on interphase formation. The interfacial microstructure and the element mappings are shown in Figure 3.3(g) and (h). This time we do not observe the presence of a thick interphase. However, the LMO phase is not fully densified at 750°C. Al^{3+} agglomerates are observed at this very thin layer between LATP and LMO bulk phase. However, the impedance analysis in Figure 3.4(d) reveals that even though the interphase resistance (R4) is negligible at this temperature, the overall resistance is still over 13MΩ. The decreased density of LMO phase resulted in an increase of the internal LMO resistance. This is likely to lead to the observed increase in the total half-cell impedance.

Our co-sintering experiments reveal several important information in terms of interphase formation:

1. The thickness of the interphase is relevant to the cooling rate. A lower cooling rate will lead to a thinner interphase and reduce the interphase impedance.

2. Al^{3+} rich agglomerates will form near LMO surface, and heating rate will affect their distance from the LMO bulk phase.

3. At 750°C, the interphase will become very thin, and result in negligible interphase impedance. However, the LMO bulk phase would not be densified at that temperature.

4 Interfacial contact needs to be sufficiently high for low interfacial impedance.

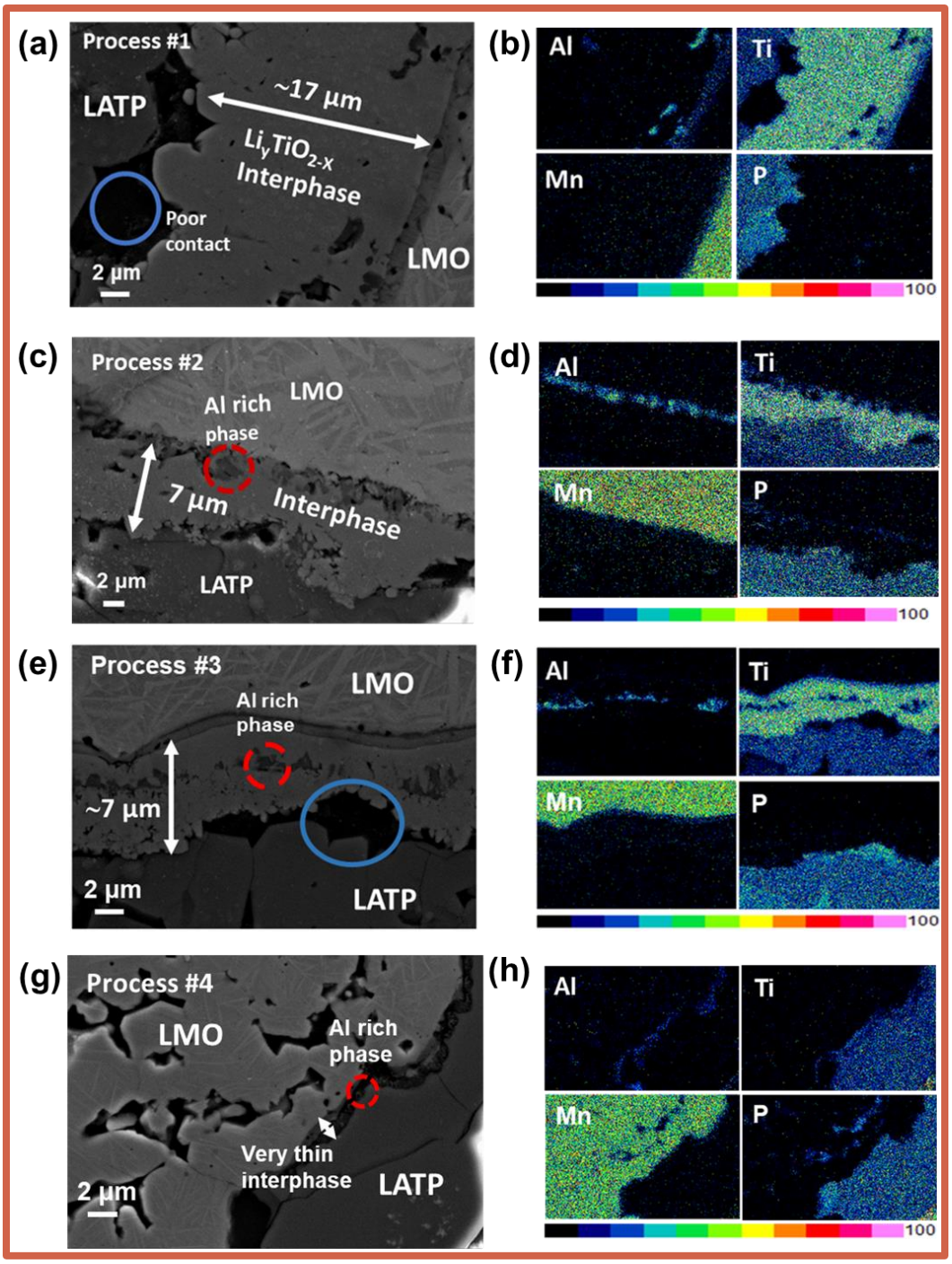

Figure 3.3. (a) Interfacial microstructure of co-sintered LATP/LMO half-cell densified by process 1. (b) Element mappings of the area in (a) obtained by EDS. (c) Interfacial microstructure of co-sintered LATP/LMO half-cell densified by process 2. (d) Element mappings of area in (c) obtained by EDS. (e) Interfacial microstructure of co-sintered LATP/LMO half-cell densified by process 3. (f) Element mappings of area in (e) obtained by EDS. (g) Interfacial microstructure of co-sintered LATP/LMO half-cell densified by process 4. (h) Element mappings of area in (g) obtained by EDS.

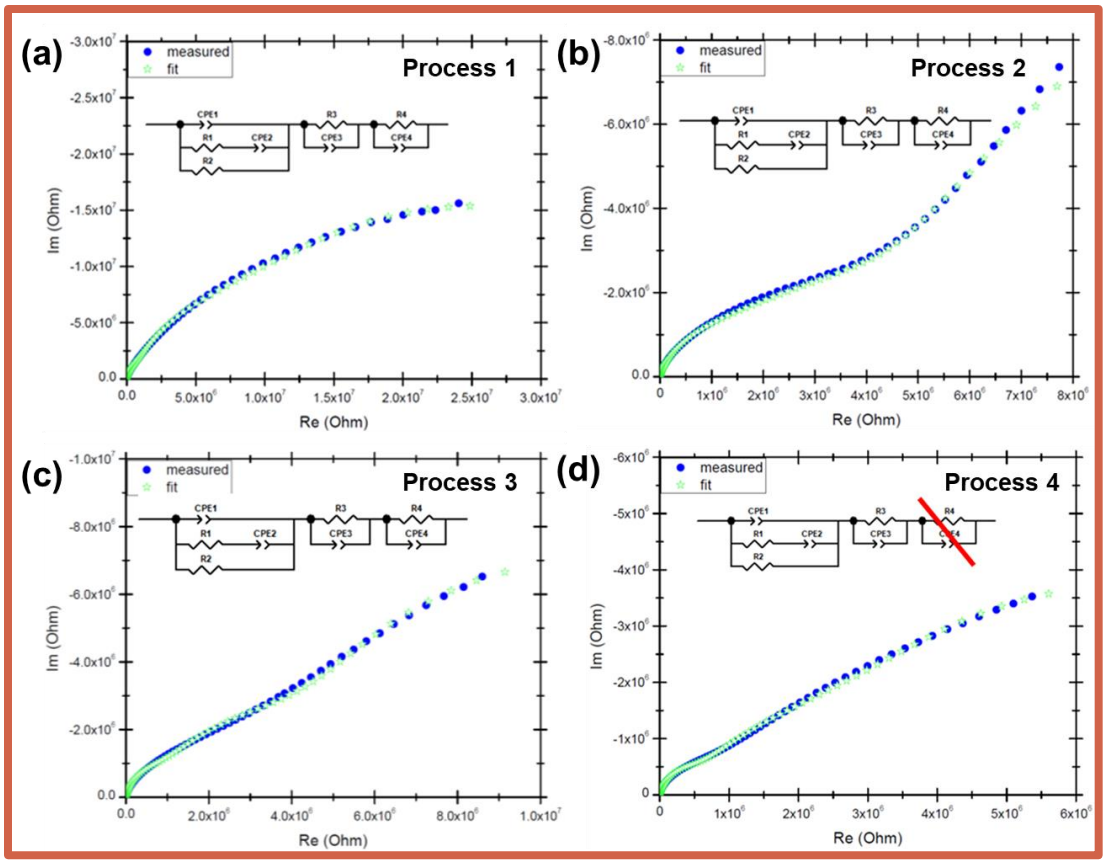

Figure 3.4. (a) Nyquist plot of Co-sintered pellet densified with process 1. Equivalent circuit is applied for the fitting. (b) Nyquist plot of Co-sintered pellet densified with process 2. Equivalent circuit is applied for the fitting. (c) Nyquist plot of Co-sintered pellet densified with process 3. Equivalent circuit is applied for the fitting. (d) Nyquist plot of Co-sintered pellet densified with process 4. Equivalent circuit is applied for the fitting.

Based on this information, we designed a novel two-step joining experiment (Figure 3.1 (b)). In this, LATP and LMO pellets are sintered first at 800°C, 50MPa for 10 minutes with heating and cooling rate of 100°C/min. Then the two pellets are polished and loaded for a second joining step. The two pellets are joined at 700°C, 20MPa for 10 minutes with a heating rate of 100°C/min, and a much slower cooling rate of 10°C/min. In this process, both pellets are densified at the first sintering step, which allows us to apply a much lower temperature at the second joining step. The low temperature of the joining step could potentially relieve the interphase formation. Moreover, we applied a much lower cooling rate to relieve the thermal stress at interface and reduce the thickness of interphase. The interfacial microstructure and element mappings are shown in Figure3.5 (a) and (b). In Figure 3.5(a), both LATP and LMO phases are densified and there is no

obvious pores or cracks at the interfacial region. Moreover, a 3 μm interphase is observed between LATP and LMO. The interphase is still a Li_yTiO_{2-x} compound. For Al^{3+} rich phase, however, instead of the formation of agglomerates as co-sintered samples, a very thin layer at LMO surface is present in this joined sample. The impedance of the interphase is analyzed by similar approach. In Figure 3.5 (c), we applied a similar equivalent circuit in the analysis of impedance data, LMO circuit is in series with two RC circuits, one RC circuit accounts for the interfacial contact and the other for interphase. From the fitting, R_3 (interfacial contact) = 0.6 MΩ and R_4 (interphase) = 8.8 MΩ. This indicates that even though the interfacial contact is improved by this two-step joining method, a high resistance interphase still forms. Although the thickness of the interphase has been reduced from 7 μm to 3 μm, the resistance from interphase still increases significantly, from 0.2 MΩ to 8.8 MΩ. This increase is probably caused by the formation of an additional Al^{3+} layer.

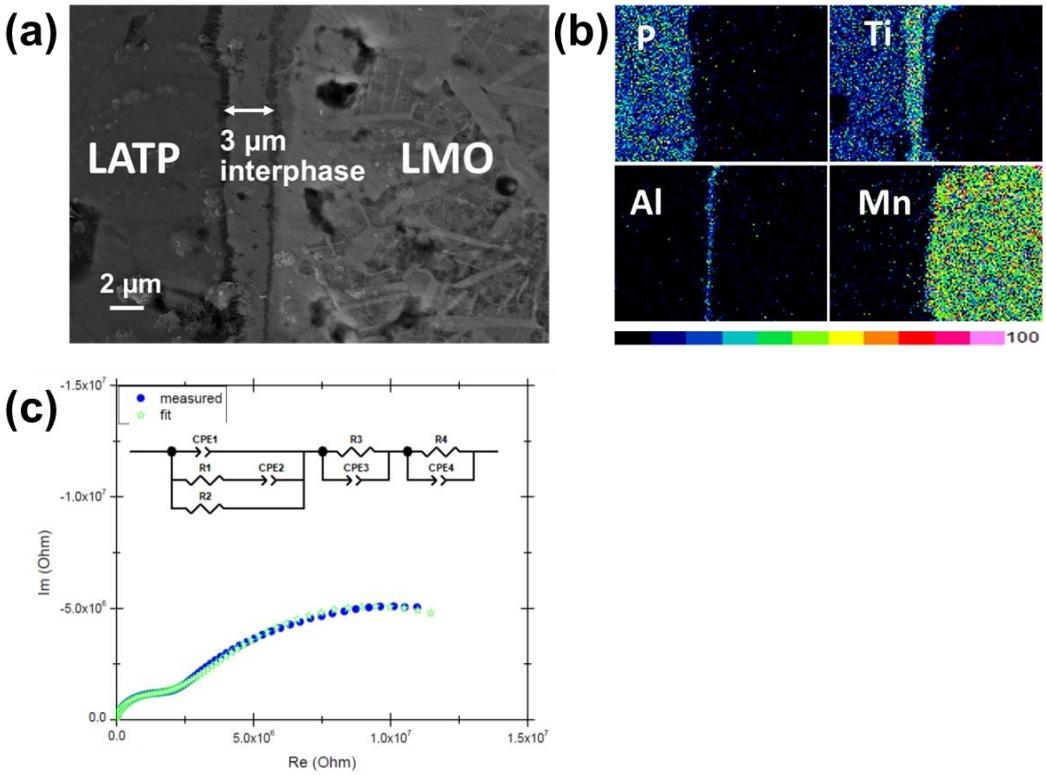

Figure 3.5 (a) Interfacial microstructure of LATP/LMO half-cell prepared by two-step joining process. (b) Element mappings of the area in (a), obtained by EDS. (c) Nyquist plot of LATP/LMO half-cell prepared by two-step joining

3.3 Conclusions

In this study, we investigated the effect of different sintering parameters on the formation of high resistance interphase. Two different sintering methods: one-step co-sintering and two-step joining have been proposed. The schematics of interface microstructure for the half-cells prepared by these two methods have been shown in Figure 3.6. The results show that the formation of a high resistance interphase is the main origin of the observed large interfacial resistance. The interphase consists of two parts. For the co-sintered half-cell (Figure 3.6(a)), there is a layer of Li_yTiO_{2-x} and agglomerations of Al^{3+} rich phase (Li-Al-O compound). The thickness of the Li-Ti-O layer depends on the cooling rate as well as processing temperature. While reducing sintering temperature can relieve the formation of interphase, however, the LMO bulk phase will be less densified and result in an increase in the overall half-cell resistance. On the other hand, for two-step joined sample, the interphase consists one layer of Li-Ti-O compound and one layer of Li-Al-O compound (Figure 3.6(b)). The interfacial contact is improved in this method, and the interphase thickness is also reduced. However, the interphase resistance increases considerably as the Li-Al-O compound forms an additional layer.

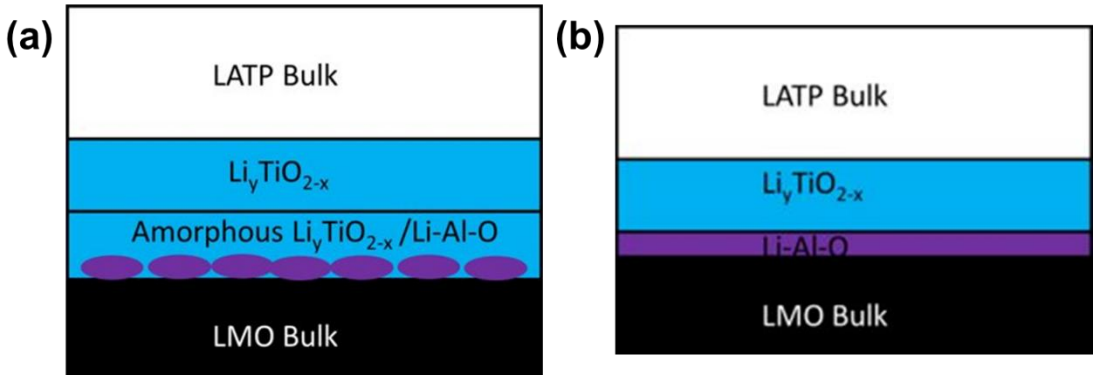

Figure 3.6 (a) Schematic of LATP/LMO interfacial microstructure prepared by one-step co-sintering (b) Schematic of LATP/LMO interfacial microstructure prepared by two-step joining

Therefore, the interphase is considered to be created by the diffusion of Ti^{4+} and Al^{3+} from the LATP bulk phase, and the O^{2-} from the LMO bulk phase. The formation of a high resistance interphase is undesirable in the preparation of cathode/electrolyte half-cells. Thus, further studies are needed to identify avenues to suppress its formation. However, SPS also exhibits its potential

in the preparation of half-cell couples. It is an effective tool in densifying solid state cathode and electrolyte materials in a short time with good interfacial contact.

CHAPTER 4. ORIGIN OF HIGH INTERFACIAL RESISTANCE IN SOLID-STATE BATTERIES: LLTO/LCO HALF-CELLS

This chapter is based on the work published in "Pengyu Xu, Wolfgang Rheinheimer, Avanish Mishra, Shoumya Nandy Shuvo, Zhimin Qi, Haiyan Wang, Avinash M. Dongare, Lia A. Stanciu. Origin of high interfacial resistance in solid-state batteries: LLTO/LCO half-cells. ChemElectroChem. DOI: 10.1002/celc.202100189"

4.1 Introduction

All-solid-state lithium ion batteries have been recognized as promising candidates for next generation energy storage devices.[2] In solid state batteries (SSBs), traditional liquid electrolytes are replaced by nonflammable solid electrolytes. Therefore, SSBs are expected to have outstanding safety performance[3]. Moreover, ceramic solid electrolytes typically provide broad electrochemical windows (>5V)[94] and high mechanical strength[95]. Thus, SSBs would have larger energy densities and longer cycling life[8,14,96].

At the same time, there are some challenges hindering the commercialization of SSBs. The poor ionic conductivity of solid electrolytes (SEs) as well as the high interfacial resistance between SEs and electrodes are the two primary obstacles confronting SSBs[10]. Large internal resistance in SSBs could lead to considerable ohmic loss, low power density and poor cycling performance [97]. Over the past decades, significant improvements have been achieved in elevating the ionic conductivities of SEs[98]. Li_2S-P_2S_5[99] and $Li_{10}GeP_2S_{12}$[11] electrolytes were reported to have ionic conductivities above 10^{-2} S/cm, which is comparable with traditional liquid electrolytes. Other oxide solid electrolytes such as $Li_{0.33}La_{0.57}TiO_3$ (LLTO)[100], $Li_{1.3}Al_{0.3}Ti_{1.7}(PO_4)_3$ (LATP)[59] and $Li_{6.4}La_3Zr_{1.4}Ta_{0.6}O_{12}$ (Ta-doped LLZO)[26] exhibit ionic conductivities in the order of 10^{-3} S/cm.

Despite the progress in SEs, our understanding of interfacial phenomena is still lagging, few studies have been reported on this topic[32,49,52,53,63,101–103] for solid state lithium ion batteries. Engineering the properties of the cathode/electrolyte interface is highly dependent on our ability to understand ion transport mechanisms for candidate solid electrolytes and cathode materials, which is the focus of this study. The formation of interfacial phases (interphases)[32,62], space-charge layer effects[49,63] and poor contact between electrodes and electrolyte[102] are the most important sources of interfacial resistance. Interphases formed by interdiffusion between cathode and electrolyte materials have been widely observed in SSBs, resulting in large interfacial resistances.

The Meng group[103] reported an interphase at the $LiCoO_2$/ LiPON interface using scanning transmission electron microscopy (STEM). The interphase was argued to cause irreversible capacity loss in the battery. Sakuda[52] investigated $LiCoO_2/Li_2S\text{-}P_2S_5$ interfaces after charging. Again, a clear interfacial layer was detected by STEM and energy dispersive spectroscopy (EDS). The Ceder group[7] theoretically testified the formation of interphases in multiple cathode/electrolyte combinations. Therefore, understanding the formation mechanism of this interphase and investigating its impact on battery resistance could be critical in engineering a structurally stable SSB.

On the experimental side, conventional co-sintering of cathode and electrolyte materials could provide sufficient interfacial contact for lowering the interfacial resistance of the half cell[104,105]. Compared with the other interfacial modification techniques such as buffer layer deposition[106,107], interface softening[108] and surface coating[64], co-sintering is the most convenient and economical method. However, the high temperature during co-sintering can lead to severe interdiffusion and cause undesired chemical reactions between cathode and electrolyte materials[109,110]. Spark plasma sintering (SPS) offers many benefits over conventional sintering; by applying uniaxial pressure and large pulsed DC current to the sample, SPS consolidates powders in a much shorter sintering time and at relatively lower temperature[72]. As a result, the formation of interphases could be alleviated in the SPS process, which makes SPS a promising technique in manufacturing cathode/electrolyte/anode SSB cells[111]. An additional new insight this work is putting forward stems from the fact that the electric field effects in SPS on the interdiffusion , which could potentially lead to the formation of metastable phases, is still not fully understood[112,113]. This potential effect is addressed here via parallel hot-pressing experiments of the cathode/electrolyte material pairs, followed by characterization.

It is now clear that to produce effective SSBs for industrial applications, an interphase with minimized ionic conduction resistance is desired. Thus, this work focuses on understanding the mechanisms of the interphase formation and its influence on ionic conductivity, which in turn could shed light on the appropriate choices of cathode/electrolyte materials. Lithium Lanthanum Titanite ($Li_{0.33}La_{0.57}TiO_3$, LLTO) is a well-known perovskite electrolyte with high bulk conductivity. LLTO is a very strong competitor among SEs when considering large-scale manufacturing SSBs.[68] LLTO is easy to handle and it is very stable in air against high moisture environment[21]. Moreover, LLTO has great thermal stability and good compatibility against high-

voltage cathode materials[20], which make LLTO a perfect candidate for investigations of interfaces in co-sintered cathode/electrolyte half-cells. In previous study[114], we investigated the interfacial phenomena in Li_2MnO_4(LMO)/$Li_{0.33}La_{0.57}TiO_3$(LLTO) half cells. The impedance of the half-cell was dominated by the interphase. In this work, we selected $LiCoO_2$ (LCO) as cathode material and investigated the feasibility of applying LLTO/LCO half-cell pair to an SSB. $LiCoO_2$ (LCO) is a cathode material currently in use for commercial batteries and offers a balance between capacity and cycling stability[115,116]. For the first time, we co-sintered the LCO and LLTO with a two-step joining via SPS to investigate the interphase formation in this system. Scanning Electron Microscopy (SEM), Scanning Transmission Electron Microscopy (STEM), High Resolution Transmission Electron Microscopy (HRTEM), Energy Dispersive X-ray Spectroscopy (EDS) and Electron Energy Loss Spectroscopy (EELS) were applied to characterize the LCO/LLTO interface. The influence of the interphase formation on the resistance of LCO/LLTO half-cell pair was analyzed by Electrochemical Impedance Spectroscopy (EIS) and computational modelling.

4.2 Experimental Procedure

Powder synthesis

$Li_{0.33}La_{0.57}TiO_3$ (LLTO) powders were prepared by the mixed-oxide/carbonate route[114]. Li_2CO_3 (Sigma-Aldrich, ≥99%), La_2O_3(Sigma-Aldrich, ≥99%) and TiO_2 (Rutile, Sigma-Aldrich, ≥99%) were mixed stoichiometric ally in ethanol with an attrition mill. The mixed powders were dried and calcined in a tube furnace at 1050°C for 6 hours in air to form the perovskite phase. Next, the LLTO powders were attrition-milled again for 2 hours to break agglomerates formed during calcination. Finally, the powders were sieved (100μm, Gilson company). The cathode material $LiCoO_2$ was commercially available from Sigma Aldrich (442704, purity of 99.8%).

SPS Co-sintering

Mixed LCO and LLTO powders were co-sintered by SPS and analyzed to understand any chemical reactions that may occur[117]. LCO and LLTO powders were mixed at a volume ratio of 1:1 in a mortar. The thoroughly mixed powders were sintered by SPS at 850°C and 50 MPa for 10 minutes, with a heating and cooling rate of 100°C/min.

LLTO/LCO half-cells were prepared through a two-step joining process[118] as sketched in Figure 4.1(a). In the first step, LLTO and LCO powders were first sintered individually by a

Thermal Technology SPS 10-3 machine into 1mm thick pellets. The pellets were sintered at 850°C and 50MPa for 10 minutes, with a heating/cooling rate of 100°C/min. To relief the thermal stress at the interface and avoid the formation of cracks, a separate joining process was designed. LLTO and LCO pellets were polished with SiC paper (800 Grit) and then joined by SPS at 700°C and 20MPa for 10 minutes. The heating rate was 100°C/min and the cooling rate was 10°C/min. Subsequently, the joined pellet was cut with a diamond blade and embedded in epoxy. The cross-section was polished by SiC paper and diamond slurry down to 1μm particle size.

The co-sintering experiment initially performed via SPS was also repeated by hot pressing, in an attempt to understand whether the electrical field had any effect on interfacial structure and composition. Thus, LLTO and LCO were pre-sintered by SPS respectively at 850°C and 50MPa for 10 minutes. The pellets were polished with SiC paper (800 Grit) and then joined in vacuum by a Centorr, Testorr^{TM} series hot pressing machine to identify the possible impact of electric fields during the bonding . The joining process was carried out at 700°C, 20MPa for 2 hours, with a heating rate of 25°C/min to 675°C, 5°C/min to 700°C and a cooling rate of 10°C/min.

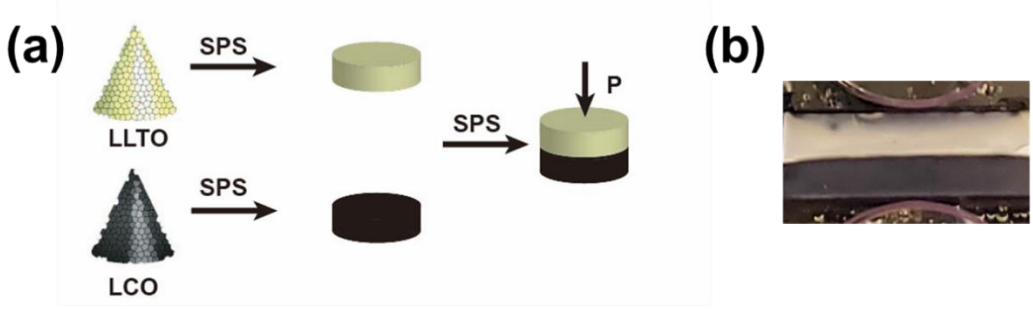

Figure 4.1. (a) Procedure of the two-step joining experiment for LCO/LLTO half-cells. (b) Polished cross-section of LCO/LLTO half-cell co-sintered via SPS.

Materials Characterization

XRD (Bruker D8 Focus, 2θ from 15° to 80°) and SEM-EDS (FEI Quanta 3D and Oxford Instruments) was used to characterize powders and samples.

For the LCO/LLTO half-cell in Figure 4.1(b), microstructures and elemental composition of the interfacial region were investigated by SEM, EDS line scans and EDS mappings. For TEM characterization, 10μm-20μm long lamellas were cut and lifted-out from the interfacial region by a Focused Ion Beam microscope (FIB, FEI Quanta 3D). Lamellas were thinned to 100nm thickness

for HRTEM, STEM, EDS and EELS characterization. HRTEM, STEM and EDS were carried out by a FEI Talos 200X TEM, STEM/EELS characterization were made by a Themis Z TEM, the dispersion is 0.05 eV/ch, while the energy resolution is 1.1eV.

Electrochemical impedance spectroscopy (EIS) was also applied to SPS sintered LLTO, LCO and the joined LCO/LLTO pellets to determine the effect of the interphase on the overall resistance. EIS measurement was carried out by a BioLogic electrochemistry potentiostat from 1 Hz to 1MHz.

4.3 Results and Discussion

Powder characterization and phase composition

Microstructural and compositional characterization of powder precursors has an impact on the understanding of the properties of the sintered samples after processing. Figure 4.2 (a) and (b) show SEM and XRD characterization of LLTO powders. Based on Figure 4.2 (a), the particle size for LLTO powders is about 1μm. Figure 4.2 (b) shows the XRD pattern of LLTO powders. According to the standard PDF card JCPDS No.870935, the synthesized LLTO is phase-pure perovskite $Li_{0.33}La_{0.57}TiO_3$.

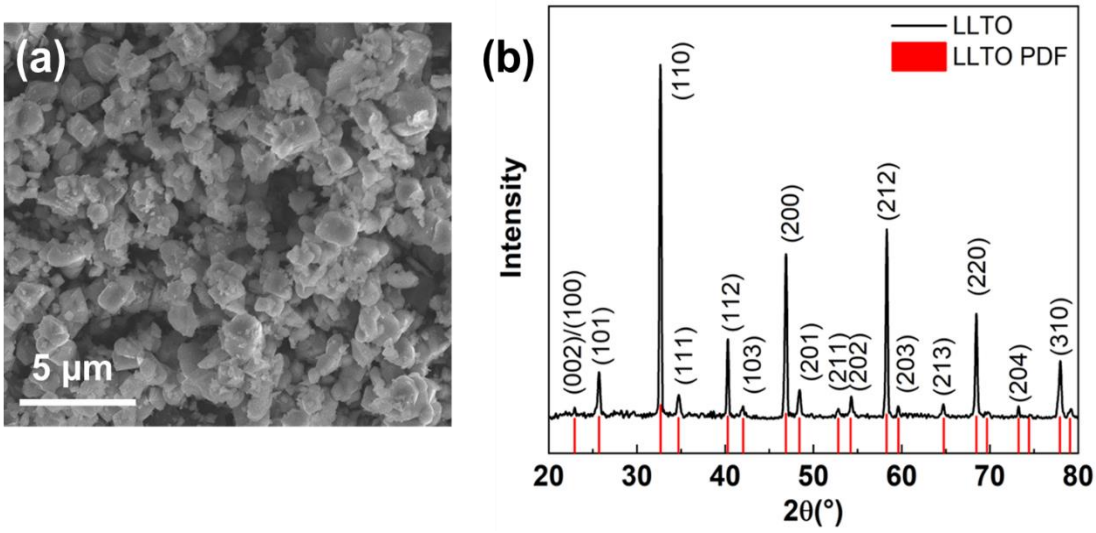

Figure 4.2. (a) SEM image of synthesized LLTO powders. (b) XRD pattern of the LLTO powders. The indexing relies on the standard PDF card JCPDS No.870935.

XRD, SEM and EDS have been applied to analyze possible reactions between LLTO and LCO powders after co-firing a powder mixture. Figure 4.3(a) shows the XRD pattern of SPS sintered LCO/LLTO powder mixture. According to the standard PDF cards, we identified two extra peaks (marked with stars) that match $Li_{1.47}Co_3O_4$ indicating a minor phase transformation during co-sintering. The corresponding microstructure and SEM-EDS mappings are presented in Figure 4.3(b). In the SEM image, based on Z contrast, we identified the darker phase as LCO and the brighter phase as LLTO. According to the SEM-EDS mappings in Figure 4.3(b), it is likely that some interdiffusion between Ti^{4+} and Co^{3+} occurred. However, very little La^{3+} interdiffusion is visible. These results indicate a chemical compatibility of LLTO and LCO. Still, the interdiffusion could potentially result in an interphase formation with a thin layer of other phases below the detection limit of XRD and SEM-EDS[114].

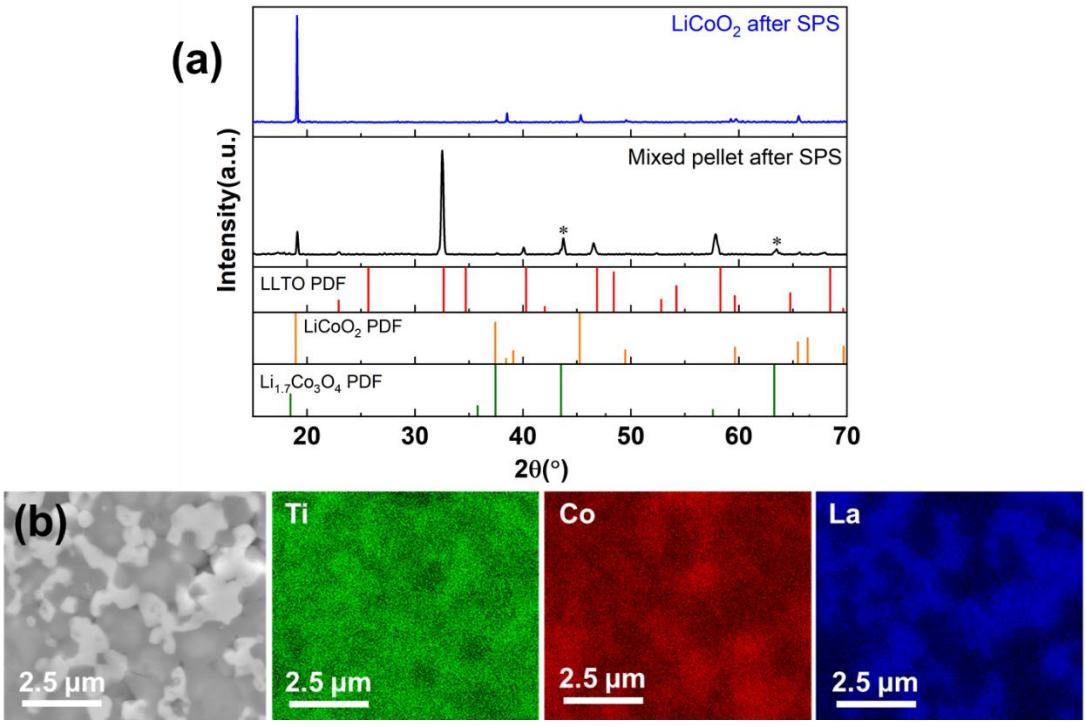

Figure 4.3. (a) XRD pattern of SPS co-fired LLTO and LCO powder mixture. The pattern was compared with standard PDF card of LCO (JCPDS No.500653) and LLTO. The extra peaks (marked with stars) match with $Li_{1.47}Co_3O_4$ (JCPDS No.782040). (b) SEM image and element mapping for the powder mixture pellet after SPS

SEM/EDS Area Scans for LCO/LLTO interface.

On the LCO side, area scans have been applied to characterize the element concentration. From Table 4.1, the atomic percentage of Ti is about 3% in all three selected regions. The La concentration is less than 2%. It is evident that more Ti diffused into LCO than La, which agrees well with the Co/Ti interdiffusion we observed in co-sintering experiment. Given that the Co concentration is about 25%, the calculated atomic fraction of Ti is about 10%. Therefore, in Figure 4.5(c), the true atomic percentage of Ti/ La would be less than 3% and 2%, given that EDS have certain detection error.

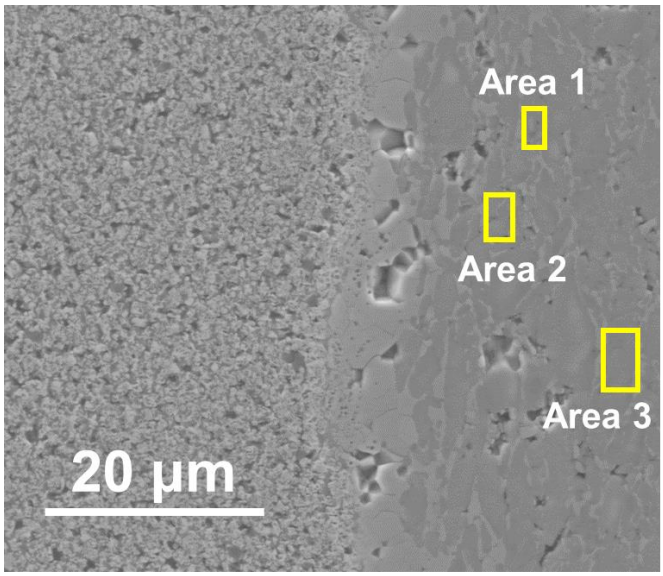

Figure 4.4 SEM image of LCO/LLTO interface. Element concentration profiles have been acquired by EDS in three different areas.

Table 4.1 Element concentration profiles obtained by area scans in Figure 4.4

Region number	Element	Atomic Percentage (%)
Area 1	C	13.2
	O	56.07
	Co	25.79
	Ti	3.19
	La	1.75
Area 2	C	13.07
	O	57.08
	Co	24.79
	Ti	3.25
	La	1.82
Area 3	C	12.63
	O	56.92
	Co	25.91
	Ti	2.91
	La	1.63

Electron microscopy characterization of LCO/LLTO half-cell

The LCO/LLTO half-cell was prepared by a SPS joining method as sketched in Figure 4.1 (b). SEM and EDS were used to investigate the microstructure and chemical composition of the interface. Based on the contrast in Figure 4.5(a), the interface contains five different layers. As LLTO contains heavier elements than LCO, it results in brighter contrast in BSE-SEM (region I). Region II is more than 20μm thick and contains a two-phase microstructure with bright grains (phase α) and dark grains (phase β) intercalating each other. From the microstructural appearance, region II might be the result of a phase decomposition of a single-phase during cooling. Note that in Figure 4.5(d), this layer seems to be porous. This is due to breakout during polishing. Region III is another 5μm thick layer, the microstructure of which is similar to Region II but the dark grains are not present in this region. Region IV is a few microns thick layer, with slightly brighter contrast compared to LCO in region V.

Figure 4.5 (c) shows the atomic fraction profile obtained by SEM-EDS line scan in Figure 4.5 (b). Significant interdiffusion was observed in a more than 100μm thick area. Most interdiffusion occurred for Co^{3+} followed by Ti^{4+}. Less La^{3+} interdiffusion occurred in this area. Combined with the SEM-EDS mapping in Figure 4.5(d), interdiffusion between Co^{3+} and Ti^{4+} is evident and, again, limited La^{3+} diffusion into the LCO is observed. This result agrees with Figure 4.3(b). However, in Figure 4.5(c), there were about 10% fraction of La^{3+} detected at the right end. According to the chemical analysis of the LCO phase (Table 4.1), the chemical composition was about 25mol% Co, 3mol% Ti and 2mol% La. Therefore, the quantification of the line scan in Figure 4.5 is only a guideline. Adequate quantification is only obtained by area scans. However, a higher resolution characterization method is necessary for the interdiffusion analysis, particularly to resolve the composition of the two phases in region II. High resolution characterization methods, such as STEM/ EDS, STEM/EELS and HRTEM have been applied to these interfacial regions (region II, region III and region IV).

In general, the interdiffusion documented in Figure 4.5 is similar to other half-cell combinations. LMO-LLTO half-cells form a very similar interfacial structure with similar interdiffusion layer width[114]. Kim[62] applied EDS line scans to detect the interdiffusion between LCO and LLZO and confirmed the presence of an interphase as well.

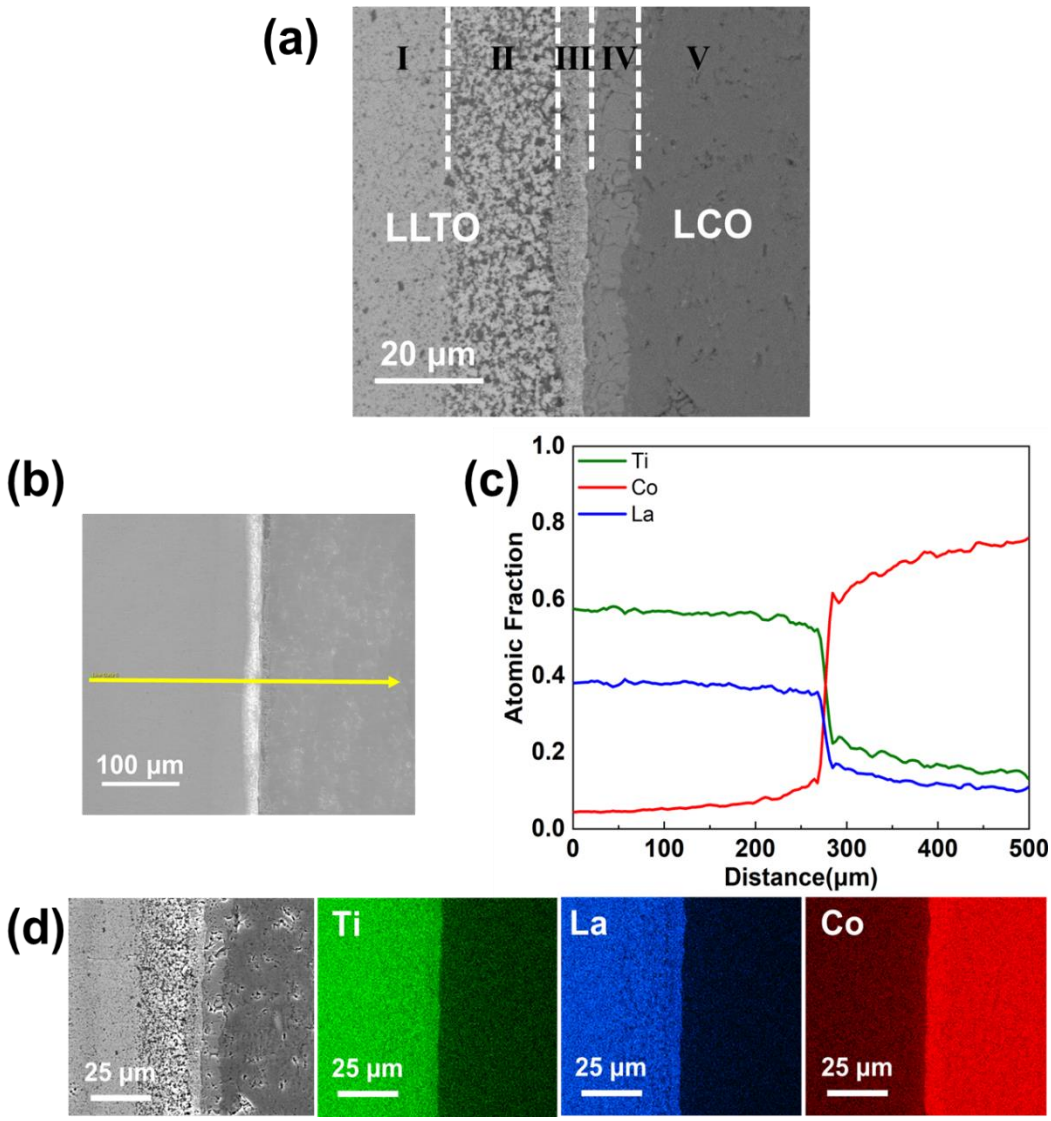

Figure 4.5. (a) Backscattered SEM image of LLTO/LCO interface, LLTO is the brighter phase (left) and LCO is the darker phase (right). The interfacial area contains five regions with different microstructures. I is LLTO phase, II is an intercalation region, III is a layer similar to II but without the second phase, IV is an LCO phase with contrast against V, V is LCO. (b) SEM image of LLTO/LCO interface, with an EDS line scan from left to right (in yellow). (c) Atomic fraction profile obtained by EDS line scan from the line marked in (b). (d) SEM image and element distribution profiles obtained by EDS mapping.

Figure 4.6(a) shows a 20μm long FIB sample containing region II, region III, region IV and a small part of region V in Figure 4.5(a). STEM/EDS characterization is applied to the entire sample area. From the HAADF-STEM image in Figure 4.6(b), four areas are identified for further chemical quantification (Table 4.2). Area 1 and Area 2 are from region II containing bright (phase

α) and dark grains (phase β) intercalated with each other. Area 1 is close to the bulk LLTO and contains fewer dark grains than area 2. Area 3 lies within an interphase formed between LCO and LLTO with a thickness of about 2μm and corresponds to region IV in Figure 4.6(a). Area 4 is from region phase V. From Figure 4.6(b) and Area 3 (Table 4.2), we can conclude that the interphase (region IV) contains Ti^{4+} and Co^{3+} but no La^{3+}, which indicates Co^{3+}/Ti^{4+}interdiffusion in this interphase. However, the JPDS database does not contain any Li-Co-Ti-O compound that matches the Co/Ti ratio of 1:1 so that the exact identity of this phase remains unclear. Given the location of this interphase in region IV (Figure 4.5(a)), we believe that this interphase has an LCO host lattice with some dissolved Ti.

The Co profiles indicate a rapid Co concentration decay from area 2 towards area 1. In area 4, the EDS results show no existence for any Ti^{4+} or La^{3+}. Therefore, the STEM/ EDS results are in disagreement with the hundreds of microns diffusion as detected by SEM. As discussed above, the TEM/EDS results seem to be more reliable because of less secondary X-ray emission compared to SEM.

To further investigate the chemical composition of bright and dark grains in area 2, high-resolution STEM/EDS scans were carried out as shown in Figure 4.6(c) and (d). The Li concentration was investigated by EELS analysis as shown in Figure 4.6(e) and (f). Based on EDS mappings (Figure 4.6(b) - (d)) and area scans (Area 5, Area 6 in Table 4.2), we conclude that in region II, phase α has less Ti^{4+} than phase β. The La^{3+} concentration in phase β is negligible. The chemical analysis of Area 5 and 6 reveals that the Ti/La ratio deviated from LLTO stoichiometry in phase α. Accordingly, La^{3+} diffused from phase β to α.

The cobalt concentration in phase α is smaller than in phase β. An accumulation of Co^{3+} was observed at the interfaces between α and β in the cobalt mappings, possibly indicating a complexion[114], space charge or a kinetic accumulation during growth of the particle (Figure 4.6(c), Figure 4.6(d)). Additionally, to verify lithium presence in the phase α and β in region II, an EELS line scan was carried out in Figure 4.7(c). Spectrums from 4 points (marked in Figure 4.6(c)) are shown in Figure 4.6(e). La $N_{4,5}$ Peaks were only observed in the bright grain spectrums (B1,B2), while the peak position is most likely shifted due to the oxidation state of La[119]. This observation accords well with the TEM-EDS results.

Li peaks were observed in phase α at about 62eV, while one measurement of the phase β (D2) showed a lithium peak at about 58eV. This peak shift of Li indicates a different oxidation

state in phase α and β. Additionally, the lithium concentration mapping in Figure 4.6(f) shows a much higher lithium concentration in α compared to β. Therefore, in the D1 spectrum, the Li peak is missing. Thus, we draw the conclusion that phase α contain Li, Ti, La, O with minor Co concentration. Phase β contain less lithium, but more cobalt and titanium.

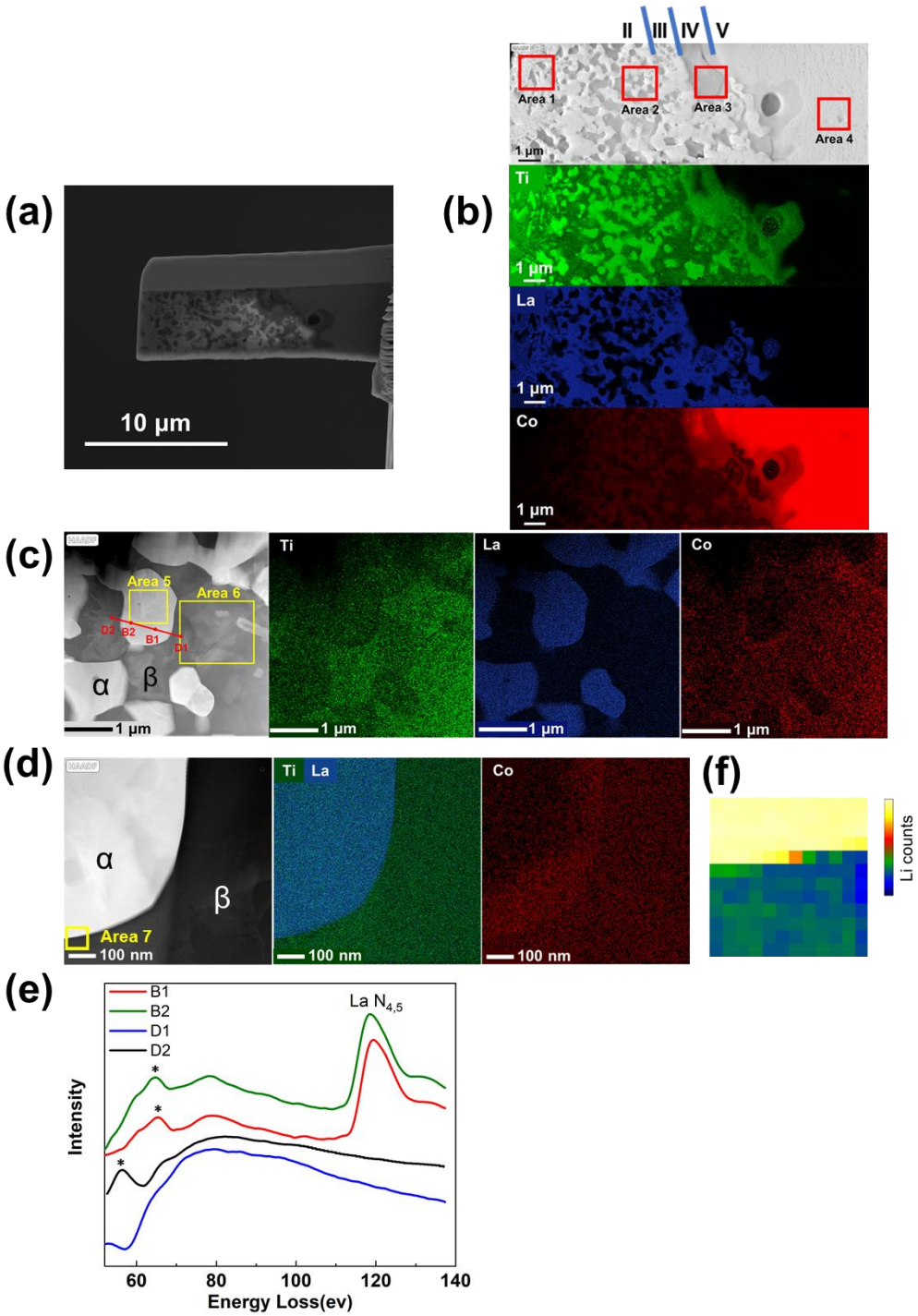

Figure 4.6. (a) SEM image of the lamella lift-out from the interfacial region. (b) Chemical mappings of the entire lamella as obtained by STEM/EDS. The four marked areas were analyzed in detail. II, III, IV, V refer to the same regions in Figure 4.5(a). (c) Chemical mapping of area 2 from (b) as obtained by STEM mapping. Again, two areas are marked. (d) Element concentration mapping of phase α/β interface. (e) EELS analysis of four points (B1, B2, D1 and D2) in (c). Lithium related peaks were marked out by stars. (f) Li concentration mapping for the area marked in (d). The color codes for Li counts in arbitrary units. The chemical composition was quantified by TEM-EDS area scans as detailed in Table 4.2.

Table 4.2 Chemical composition for the six areas marked in Figure 4.6(b) and (c), as obtained by STEM/EDS area scans

	Atomic Fraction (mol%)					
Element	Area 1	Area 2	Area 3	Area 4	Area 5	Area 6
O	55.73	54.19	55.46	41.9	64.47	74.96
Ti	27.34	25.43	21.37	0.05	15.79	22.07
Co	1.76	7.88	23.17	58.04	0.28	2.7
La	15.17	12.5	0	0.01	19.46	0.26

To confirm the Co^{3+}/Ti^{4+} interdiffusion would lead to the formation of interphase in the LLTO/LCO half-cell, it is necessary that we eliminate effect of electric field in SPS. Therefore, a hot-pressing joining has been applied to the pre-sintered LLTO, LCO pellets. Similar to the previous discussed approach, a 15μm lamella was cut and lift-out from the interfacial region of the hot-pressing LLTO/LCO sample. HAADF STEM and EDS has been applied to identify phase composition information. From the HAADF STEM image in Figure 4.7(b), we noticed that the microstructure in this hot-pressing interface is very similar to that of SPS sample (Figure 4.6(b)), the interfacial region still an intercalation region (region II) and a new phase in LCO side (region IV). Additionally, the EDS mappings in Figure 4.7(b) confirmed that the phase composition in this hot-pressing sample is the same as previous discussed SPS sample. Thus, we can safely draw the conclusion that the interdiffusion in the LLTO/LCO half-cell is not affected by the electric field and current during SPS.

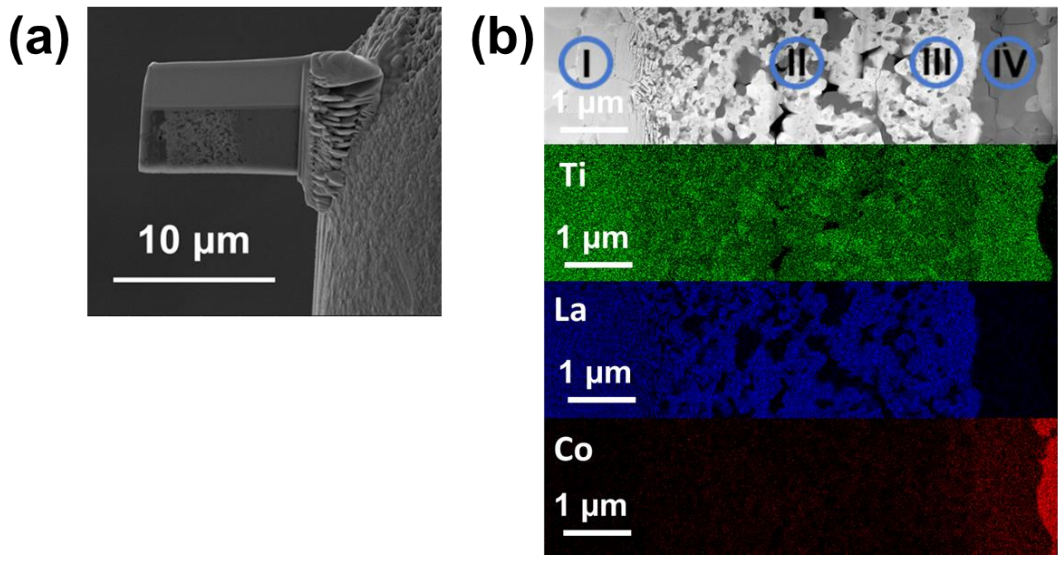

Figure 4.7. (a) SEM image of the lamella lift-out from the interfacial region of hot-pressing sample. (b) HAADF image and EDS mapping of the sample in (a).

To further investigate the interface between α and β in layer II for any interphase or complexion[120] in the intercalation region, HRTEM was applied to the interface in Figure 4.6(d) as shown in Figure 4.8 (a), (b). Figure 4.8 (b) revealed a tilted grain boundary between phase α and β grains. Phase α is crystalline perovskite phase while phase β has a $LiTi_2O_4$ host lattice. This finding is underlined by SEAD patterns presented in Figure 4.8(c), (d) and Figure 4.9. Based on Figure 4.8(c) and (d), we can determine that the crystal has an FCC lattice with lattice parameter of ~8.4 Å. After checking JCPDS database and matching with modeling result in Figure 4.10(b). The β phase diffraction pattern fits $LiTi_2O_4$ lattice (JCPDS No.400407). However, there is no evidence of a complexion other than the Co enrichment discussed with Figure 4.6(c) and (d).

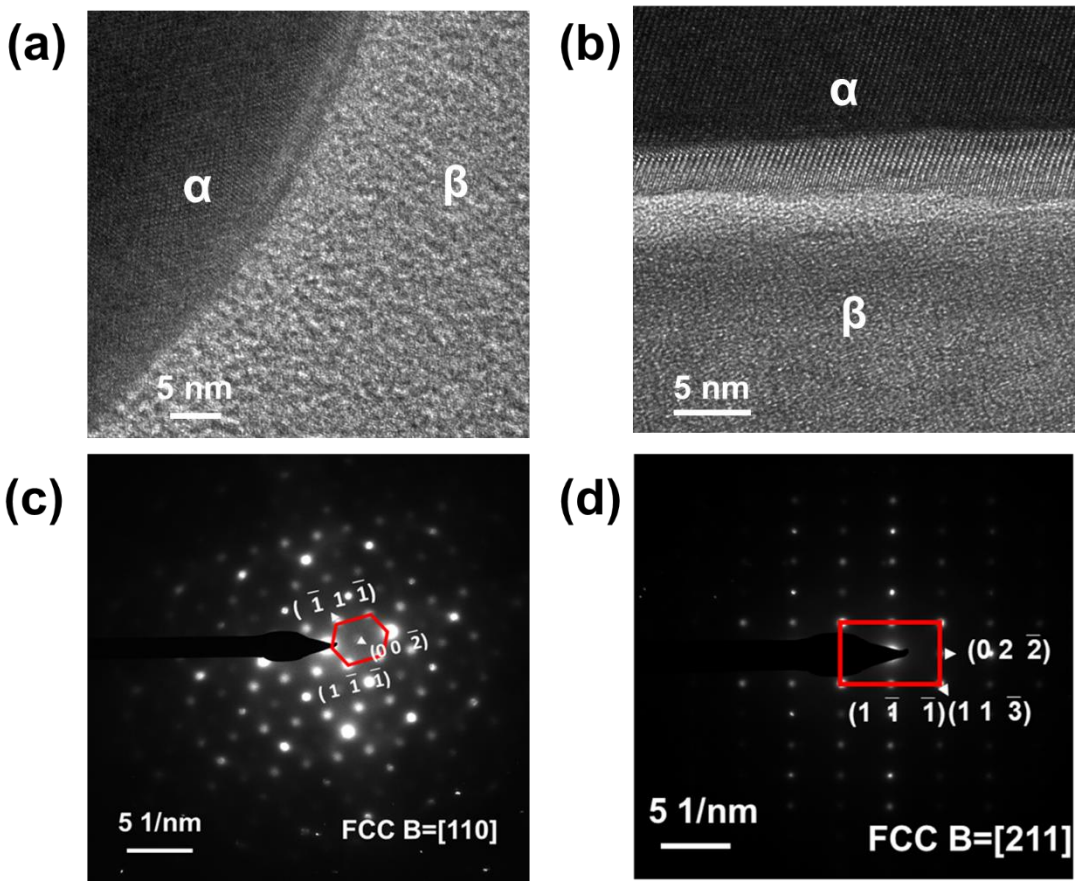

Figure 4.8. HRTEM image of bright (phase α) and dark grain (phase β) interface. (c) SEAD pattern of β grain in [110] zone, (d) SEAD pattern for β grain in [211] zone.

Figure 4.9 showed diffraction pattern of bright gains in Figure 4.6(c). The bright grain SEAD showed the similar pattern as tetragonal LLTO phase.

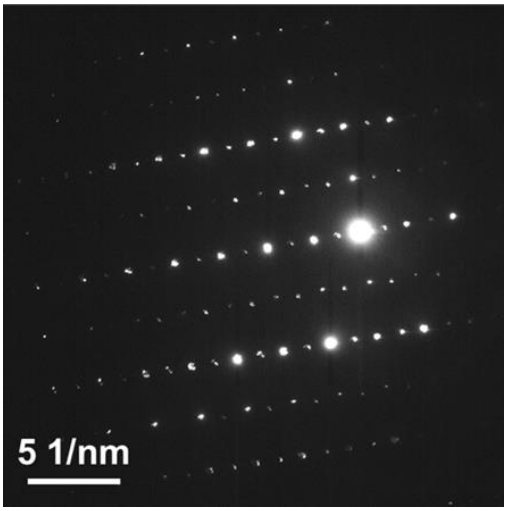

Figure 4.9 SEAD pattern for bright grains. (LLTO)

In summary, the analytical TEM reveals that at the interfacial region in LCO/LLTO half-cells, three additional layers (II, III, IV) have been identified by SEM/TEM observations. In Region II (Figure 4.5(a)), we identified two different phases (α, β) intercalating. Analytical TEM reveals that phase α is a crystalline Li-La-Ti-Co-O compound in perovskite phase, while the phase β is an Li-Ti-Co-O compound with a $LiTi_2O4$ host lattice. Phase α is rich in Li while phase β has higher Co and Ti concentration. Region III is a thin layer of phase α (Li-La-Ti-Co-O). Region IV is another few micron thick layer with LCO host lattice containing some Ti^{4+}. However, none of these compounds could be identified as a separate phase based on stoichiometry and the JCPDS database.

The EDS analysis for the interphase in Region III clearly indicated that an interdiffusion between Co and Ti occurred. In the perovskite LLTO, La^{3+} cations have a coordination number of 12 and Ti^{4+} have a coordination number of 6. In the LCO phase, Co^{3+} has a coordination number of 6. The ionic radii of these cations are 150 pm (La^{3+}), 74.5pm (Ti^{4+}) and 75pm (Co^{3+})[85]. Diffusion of La ions into the LCO are limited by a large misfit in ionic radius. However, as the Ti^{4+}/Co^{3+} couple have very similar ionic radii, like a substitutional interdiffusion occurred. The diffusion distance for Ti^{4+} was about 2μm in the interphase layer, while the Co^{3+} diffusion distance was about 20μm. As more Co^{3+} diffused in LLTO than Ti^{4+} diffused in LCO, it is possible that some Co vacancies are introduced in LCO thereby changing the point defect chemistry.

Computational Simulations of β Phase Composition

As observed in the experimental diffraction pattern of β phase (dark grains) showed in Figure 4.8(c) and (d), indicate the existence of Li-Ti-O FCC structure with a lattice parameter of ~8.4 Å. However, there could be various possible combinations of Li-Ti-O with different stoichiometry with FCC crystal structure and similar lattice parameter. To identify the possible stable compound with FCC crystal structure, we constructed a phase diagram of Li-Ti-O at 0K using the "phase diagram" package of the pymatgen library[121,122] . The solid dots/nodes in Figure 4.10 show stable compositions, whereas red and blue nodes highlight stable ternary phases. Other than $LiTi_2O_4$ (blue node), the rest compositions do not possess FCC symmetry (Fd-3m) for the minimum energy phase. The calculated lattice parameter for FCC $LiTi_2O_4$ is 8.46 Å, which is close to the observed value from the diffraction experiment. Besides, $LiTiO_2$ also exhibits an FCC crystal structure, but for a higher energy phase.

Further, to validate that the observed structure is $LiTi_2O_4$, we simulated the virtual selected area-electron diffraction (SAED) patterns for the FCC phase for comparison with the experimental findings. The SAED patterns are simulated for a supercell of $LiTi_2O_4$ using the Large-scale Atomic/Molecular Massively Parallel Simulator (LAMMPS) [123] user-diffraction package[124,125] . For SAED, an irradiation wavelength of 0.0251 Å (200-keV electron radiation) and a cutoff radius to 1.25 Å−1 are utilized. The SAED patterns are visualized for [110] and [211] zone axes to compare with experimental prediction. The SAED patterns are shown in Figure 4.10 (b) and show similar spots to those observed in the experimental diffraction patterns. The simulated SAED patterns confirm the formation of phase β with a $LiTi_2O_4$ structure and a lattice parameter of ~8.4 Å.

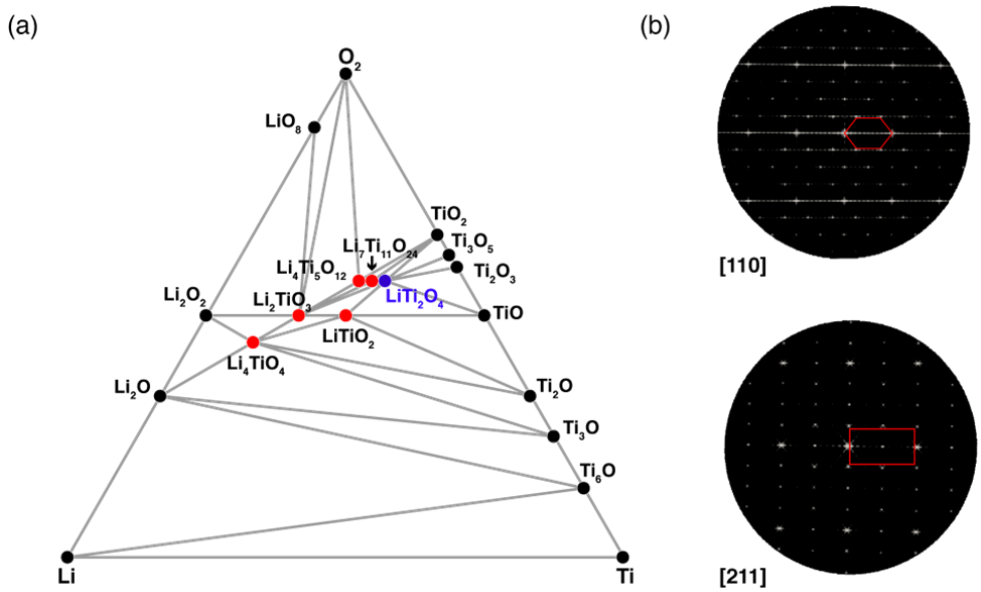

Figure 4.10. (a) Simulated phase diagram for Li-Ti-O to confirm possible structure with FCC symmetry. The red dots represent stable structure with combination Li-Ti-O, and the blue dot indicates stable structure with FCC as minimum energy phase (LiT_2O_4). (b) The simulated virtual selected area-electron diffraction (SAED) patterns of FCC LiT_2O_4 along [110] and [211] zone axes.

Electrical Characterization of the LCO/LLTO half cell

It was shown before that the formation of an interphase by interdiffusion can lead to very large interfacial resistance[114], which is undesirable in SSBs. This interphase layer appears as an additional part in the Nyquist plot of electrochemical impedance spectroscopy (EIS)[32]. In the present study, EIS analysis was carried out for an LCO/LLTO half-cell joined by SPS (700°C, 10 minutes, 20MPa).

Figure 4.11(a) shows the impedance profile of an LLTO pellet sintered by SPS (850°C, 10 minutes, 50MPa). An equivalent circuit as shown in Figure 4.11(a) was used to fit the impedance data.[114] The fitting parameters are listed in Table 4.4. The grain boundary impedance is expected to contribute to the low frequency part. Therefore, the grain boundary resistance for LLTO was 2714 Ω yielding a grain boundary conductivity of $\sigma_{gb} = \rho\frac{l}{s} = 4.69\times10^{-5}$ S/cm. The bulk conductivity of LLTO including both grain and grain boundary resistance was found to be 4.62×10^{-5} S/cm. This is comparable with the LLTO bulk conductivity reported in the literature[126].

The impedance profile of the LCO pellet sintered by SPS (850°C, 10 minutes, 50MPa) is shown in Figure 4.11(b). Both electronic and ionic conductivity occur in LCO[87]. Therefore, the equivalent circuit in Figure 4.11(b) was used. The fitting parameters are listed in Table 4.5.

Figure 4.11(c) shows the impedance of the LCO/LLTO half-cell along with LCO and LLTO. The impedance of LLTO is two order of magnitude lower than that of LCO and LCO/LLTO (see inset). The LCO/LLTO impedance is two times larger than the LCO impedance. Accordingly, the interfacial resistance is in the same order of magnitude as the LCO bulk impedance. To obtain detailed information on the impedance signal of the interphase, a subtraction method had been applied to analyze the data[114]. The imaginary part of the interphase ($Z_{interphase}$) was estimated based on the information of sperate LCO (Z_{LCO}) and LLTO (Z_{LLTO}):

$$Im(Z_{interphase})=Im(Z_{LLTO/LCO})-(Im(Z_{LLTO})+Im(Z_{LCO})). \quad (1)$$

Analogue, the real part of interphase was estimated by:

$$Re(Z_{interphase})=Re(Z_{LLTO/LCO})-(Re(Z_{LLTO})+Re(Z_{LCO})). \quad (2)$$

The calculated imaginary and real parts for this interphase were plotted in a Nyquist plot ($-Im(Z_{interphase})$ vs $Re(Z_{interphase})$) showed in Figure 4.11(d), with a frequency range from 50kHz to 1Hz. In the Nyquist plot, we observed two semi-circles, which were fitted with two RC circuits. A single CPE element was also added to account for the low frequency tail. The corresponding equivalent circuit provides a reasonable fitting result in Figure 4.11(d). The fitting parameters are shown in Table 4.6. Based on the fitting, it was evident that the interfacial resistance contains two parts. The total resistance for the interphase layer can be estimated based on R1(296730 Ω) and R2(160279 Ω), which adds to about 4.6×10^5 Ω.

Based on the equivalent circuit for the interphase we applied in Figure 4.11(d) and the equivalent circuits for separated LLTO and LCO, a circuit for the joined LCO/LLTO pellet can be obtained by placing the LLTO, LCO, interphase circuits in series. The circuit is shown in Figure 4.11(e). The grain impedance for LLTO is very low compared to the other components, therefore we neglected this part in the fitting process of the LLTO/LCO half-cell. The remaining parameters for LLTO and LCO were taken from the fitting in Figure 4.11(a) and (b) and were held constant.

The parameters for the interphase (R5, CPE5, R6, CPE6) were obtained by fitting the LCO/LLTO impedance profile with the equivalent circuit in Figure 4.11(e). According to Figure 4.11(f) and Table 4.3, the fit is very accurate. From this data, the impedance parameters of the interphase are R5= 298010 Ω, Q5= 5.144×10^{-11} F·s $^{a-1}$(a=0.99708), R6=108680 Ω and Q6=1.7388×10^{-8} F·s $^{a-1}$ (a=0.92347). These values agree well with the subtraction method in Figure 4.11(d). Therefore, we conclude that the interfacial resistance of LCO/LLTO contains two parts and the total resistance is about 4×10^5 Ω.

The effective capacity for a constant phase element can be calculated through the equation:

$$c_{eff}=Q^{1/a}R^{(1-a)/a} \qquad (3)$$

Where Q and a are CPE parameters.

Using a plate capacitor approach, the obtained capacity can be used to calculate the thickness of the interphase layers, where:

$$d = \varepsilon_0\varepsilon_r A/C \qquad (4).$$

ε_0 is the permittivity of vacuum and ε_r is the relative permittivity. We approximate ε_r=30 for LCO and LLTO. A is the cross-sectional area of the sample. The obtained thickness is 400μm for CPE5 and 2μm for CPE6. The 2μm layer matches the thickness of interdiffusion layer we observed in Figure 4.6(b), while the layer thickness of 400μm probably stems from bulk LLTO or LCO. Therefore, resistance of the LLTO/LCO interdiffusion layer is 10^5 Ω, which 40 times larger than the overall electrolyte resistance.

The EIS results underline that the interfacial resistance from the interdiffusion layer was still the major cause for the large internal resistance solid-state batteries and is likely to be a major problem to be overcome in such batteries[127]. Our group previously reported that this challenge does not only apply to LCO/LLTO half-cells, but also to LMO/LLTO half-cells[114]. Therefore, any cathode/electrolyte material pairs where an interphase is induced by interdiffusion is unfavorable for battery applications and needs to be suppressed carefully by choosing material combinations and processing methods that minimize this effect.

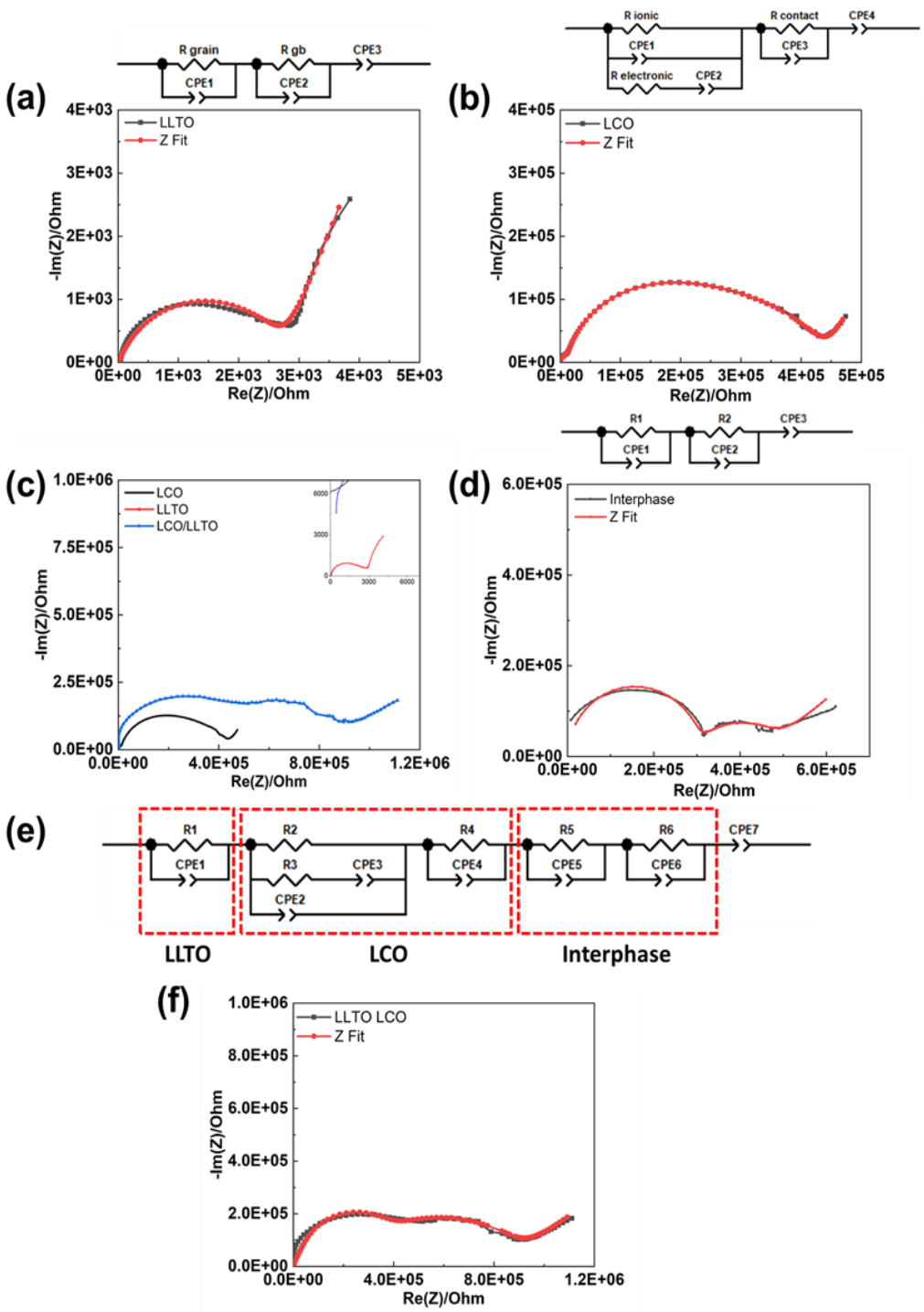

Figure 4.11 (a) Impedance profile of LLTO sintered by SPS. The equivalent circuit on the top was used for the fitting. (b) Impedance profile of LCO sintered by SPS along with the used equivalent circuit. (c) The impedance profiles of LLTO (red), LCO (black) and LLTO/LCO. (d) Nyquist plot of LCO/LLTO interphase from the subtraction method in the frequency range from 50kHz to 1Hz. (e) equivalent circuit for LLTO/LCO half-cell. (f) Impedance profile of LLTO sintered by SPS. The equivalent circuit from (e) was used for the fitting.

Table 4.3 Fitting parameters of LLTO/LCO impedance in Figure 4.11(f)

Parameter	Value	Unit	Freedom
R1(LLTO)	2714	Ohm	Fixed
CPE1 (LLTO)	1.218×10^{-6}	$F\cdot s^{a-1}$	Fixed
a1	0.766		Fixed
R2(LCO)	429720	Ohm	Fixed
CPE2(LCO)	1.256×10^{-6}	$F\cdot s^{a-1}$	Fixed
a2	0.87965		Fixed
R3(LCO)	672300	Ohm	Fixed
CPE 3(LCO)	8.807×10^{-9}	$F\cdot s^{a-1}$	Fixed
a3	0.66179		Fixed
R4(LCO)	10262	Ohm	Fixed
CPE4(LCO)	1.254×10^{-10}	$F\cdot s^{a-1}$	Fixed
a4	1		Fixed
R5(interphase)	298010	Ohm	Free
CPE5(interphase)	5.144×10^{-11}	$F\cdot s^{a-1}$	Free
a5	0.99708		Free
R6(interphase)	108680	Ohm	Free
CPE6(interphase)	1.7388×10^{-8}	$F\cdot s^{a-1}$	Free
a6	0.92347		Free
CPE7	1.5643×10^{-6}	$F\cdot s^{a-1}$	Free
a7	0.40422		Free

Additional Electrical characterization information

1. SPS sintered LLTO (d=1cm, h=1mm).

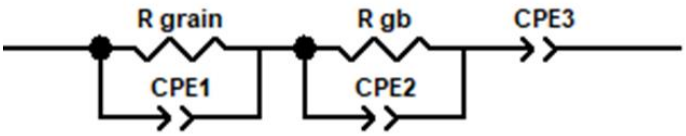

Figure 4.12 Equivalent circuit for LLTO.

Table 4.4 Fitting parameters for SPS sintered LLTO

Parameter	Value	Unit
CPE1	9.693×10^{-9}	$F\cdot s^{a-1}$
a1	1	
R grain	10.43	Ohm
CPE2	1.218×10^{-6}	$F\cdot s^{a-1}$
a2	0.7666	
R gb	2714	Ohm
CPE3	8.4512×10^{-5}	$F\cdot s^{a-1}$
a3	0.76104	

2. SPS sintered LCO (d=1cm, h=1mm)

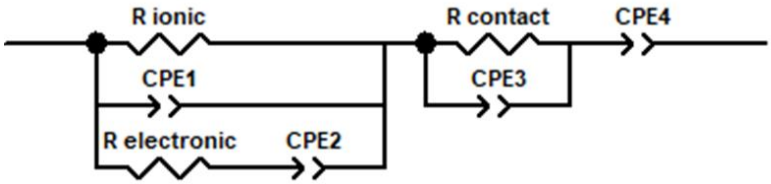

Figure 4.13 Equivalent circuit for LCO.

Table 4.5 Fitting parameters for SPS sintered LCO.

Parameter	Value	Unit
CPE 1	1.256×10^{-9}	$F\cdot s^{a-1}$
a1	0.87965	
R ionic	429720	Ohm
R electronic	672300	Ohm
CPE 2	8.807×10^{-9}	$F\cdot s^{a-1}$
a2	0.66179	
R3	10262	Ohm
CPE 3	1.254×10^{-10}	$F\cdot s^{a-1}$
a3	1	
CPE 4	3.3108×10^{-6}	$F\cdot s^{a-1}$
a4	0.68525	

3. LCO/LLTO interphase obtained by subtraction method.

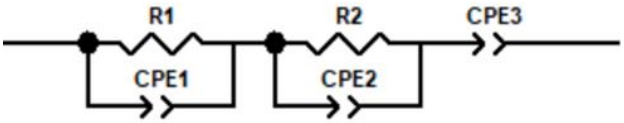

Figure 4.14 Equivalent circuit for LCO/LLTO interphase

Table 4.6 Fitting parameters for LLTO/LCO interphase by subtraction method

Parameter	Value	Unit
R1	296730	Ohm
CPE 1	4.672×10^{-11}	$F\cdot s^{a-1}$
a1	1	
R2	160279	Ohm
CPE 2	3.606×10^{-8}	$F\cdot s^{a-1}$
a2	0.7856	
CPE 3	2.327×10^{-6}	$F\cdot s^{a-1}$
a3	0.4508	

4.4 Conclusions

In this work, we studied the compatibility between the commercial cathode material $LiCoO_2$(LCO) and the perovskite solid electrolyte $Li_{0.33}La_{0.57}TiO_3$(LLTO) as it relates to their interfacial properties. An LCO/LLTO half-cell was prepared by a two-step joining via Spark Plasma Sintering (SPS). Subsequently, interfacial microstructures and the effect of interphase formation on half-cell conductivity were investigated by analytical SEM, TEM and EIS. At the LCO/LLTO interface, we observed 3 layers in addition to the pure LLTO or LCO phases:

-Region II: Phases α and β intercalating with each other. Phase α is a crystalline Li-La-Ti-Co-O compound, with a LLTO host lattice. Phase β is a Li-Ti-Co-O compound, with a $LiTi_2O_4$ host lattice. Phase α is Li rich and phase β is Ti rich. This structure probably formed due to a phase decomposition during cooling.

-Region III: A few microns thick layer of phase α, no existence of phase β.

-Region IV: A few microns thick interphase layer of Li-Co-Ti-O compound, which is a LCO host lattice with some Ti content.

According to the EIS analysis, the formation of an interdiffusion layer contributes to an interfacial resistance of $10^5\ \Omega$, which is 40 times larger than that of the LLTO bulk phase. Therefore, we concluded that it is the interdiffusion between Co^{3+} and Ti^{4+} that results in great interfacial resistance in the LCO/LLTO half-cell pair, making this material selection unfavorable for SSB applications. To improve the performance of the SSBs it is mandatory that the interdiffusion of ions at the cathode/electrolyte interface is suppressed. Interphase engineering would be necessary to improve the ionic conduction.

CHAPTER 5. COLD SINTERING PREPARATION FOR LLTO/LMO HALF-CELL*

5.1 Introduction

Cold sintering(CS) is a novel sintering technique that enables consolidation of inorganic ceramic powders at temperatures below 300 °C. [128] During the cold sintering (CS), a volume fraction of about 1-10% liquid is added to the powders as mass transport medium. Water is the most common liquid for CS, while in other cases organic solvents can also be used as this liquid phase.[129] The particles would exhibit some solubility in the selected liquid media. Subsequently, the powders are loaded in a die and the densification is carried out under a uniaxial pressure of 100~500MPa and temperature of RT to approximately 300°C.

In cold sintering, the consolidation of particles includes two main stages[129,130]: (i) the initial stage where particle compaction take place, and (ii) the second stage that includes dissolution, precipitation and grain growth, etc. In the initial stage, the introduced liquid phase serves as the lubricant and facilitates rearrangement of particles. Part of the sharp edges of particles would dissolve in liquid phase and be rearranged as the liquid phase fills the interstitial space between particles and therefore result in particle compaction. The second stage takes place at elevated temperature under high uniaxial pressure. As the temperature is elevated at this stage, liquid phase evaporation occurs, and the remaining solution at particle interstitials becomes supersaturated. The applied high uniaxial pressure provides an additional driving force for mass transportation. In this case, the heterogeneous/ homogeneous nucleation takes place during this precipitation to minimize the surface free energy, followed by further Ostwald Ripening grain growth. Therefore, the porosity is removed in this step. On the other hand, Dr. Randall's group also proposed a second route[129], which is a metastable glass phase formation in the precipitation, which bridges the initial stage to the final product. Dr. Guo pointed out that according to the Oswald step rule[131], the supersaturated solution could nucleate an amorphous phase, after which the amorphous phase needs to go through recrystallization to form the final product. This new route was verified as Dr. Guo observed a glassy phase at the grain boundaries of $BaTiO_3$ densified through CS[132]. The formation of a glassy amorphous phase is usually expected when the first crystallization route is

* The author acknowledges Wolfgang Rheinheimer and Lia Stanciu for contribution to this work

not kinetically favorable.[128] However, the formation of this glassy phase is proven to have effect on ion transportation performance. Therefore, in most of the cold sintering work, a post-heating step is applied to eliminate this glassy phase.

Various inorganic materials have been reported that could be densified by the CS at temperatures below 300°C[128]. In CS, enhanced densification at low temperature could potentially relieve the temperature driven interdiffusion at cathode/ electrolyte interface, therefore suppress the formation of high resistance interphase. The application of CS on solid electrolyte materials have been investigated[133]. The low temperatures for CS could minimize the lithium loss of electrolyte materials during processing as well as suppress the side reactions. Dr. Randall's group have managed to densify $Li_{1.5}Al_{0.5}Ge_{1.5}(PO_4)_3$ (LAGP) to about 80% density with cold sintering, the ionic conductivity reached 5×10^{-5} S/cm.[134] Thus, feasibility of applying cold sintering to solid electrolyte material has been proved. Moreover, densification of cathode material $LiFePO_4$ (LFP) with 6 wt% of carbon fiber through CS had also been reported by Dr. Randall group.[135] This further proved the possibility to apply cold sintering technique to battery materials. (cathode and electrolyte).

In previous chapters, the $Li_{0.33}La_{0.57}TiO_3$ (LLTO)/ $LiMn_2O_4$(LMO) half-cell, which was prepared by one-step co-sintering have been discussed. An interdiffusion layer was observed and originated a large resistance that is 40 times higher than LLTO. To suppress such unwanted diffusion, a lower temperature sintering technique, cold sintering, holds great promise. In this chapter, the densification of LLTO and LMO via cold sintering is investigated.

5.2 Experimental

Powder synthesis

$Li_{0.33}La_{0.57}TiO_3$(LLTO) powders are prepared by the same solid-state reaction method as mentioned in previous chapters. The particle size of LLTO is about 1 μm, powder, SEM and XRD have been applied to characterize the homemade LLTO. Two kinds of $LiMn_2O_4$(LMO, spinel) powders are used in the experiment. LMO powders with <0.5 μm particle size, >99% purity as well as electrochemical grade LMO are both commercially available from Sigma Aldrich. SEM and XRD again have been applied to characterize LMO powders.

Cold sintering

The setup of the cold sintering experiment is shown in Figure 5.1. Experimental set-ups include a ½ inch dry pressing die from MTI corporation; a Φ40mm × 45mm AC 110V 380W cylindrical heater; an LC-Z power controller, which is connected to the heater; two thermocouples, of which TC 1 is connected to the outer surface of the heater, and TC 2 is connected to the upper punch of the die. A Central Hydraulics 50 Ton Shop Press (Model 96188) is used to apply uniaxial press.

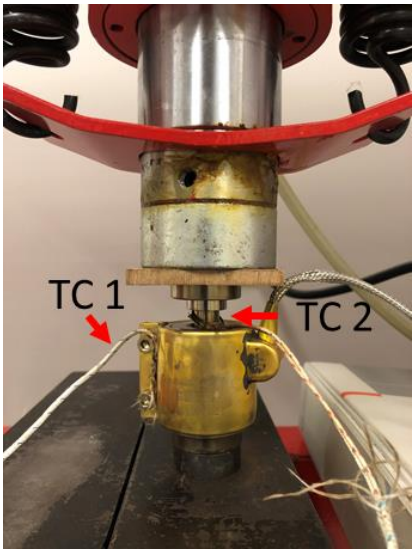

Figure 5.1. Experimental set up of cold sintering experiment

In this chapter we applied cold sintering to densify LLTO and LMO powders at different temperatures and holding times. Further, we applied a one-step co-sintering process with CS. During CS, 1g of LLTO powders were mixed with 0.09 g of DI water (about 40 vol% of the powder) in a mortar and pestle. Next, the well mixed powders were transferred to the die and a 500MPa pressure was applied. During heating, the sample temperature was estimated to be equivalent to the punch temperature (TC2). TC1 was used to regulate heating power, so that the temperature difference between the heater and punch was less than 15℃. Samples were held at 150℃, 180℃ and 200℃, respectively, for 40 minutes. The densification of LMO followed the same procedure. The co-press CPS for LLTO/LMO half-cell followed the flow chart as Figure 5.2. Here, 1g LLTO powders and 1g LMO powders were pre-mixed with 0.09 g of DI water, respectively. LLTO powders were transferred to the die and pressed into a green pellet, then LMO

powders were placed on the top of LLTO pellet and pressed into a co-pressed green pellet. Then, the co-pressed green pellet was densified by cold sintering at 200℃, 500MPa with 40 minutes holding time.

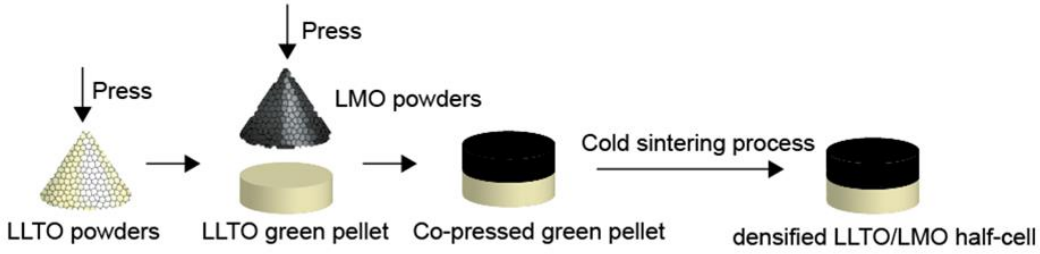

Figure 5.2 Experimental procedure for LLTO/LMO half-cell prepared by CS

X-ray diffraction (XRD) Characterization:

Powder characterization was performed by a Bruker D8 focus XRD machine. For LLTO powders, scan range is from 2θ = 20°~80°, with a scan rate of 5 degrees/ min. For LMO powders, scan range is from 2θ = 15°~80°, with a rate of 5 degrees/ min. The diffraction patterns are compared with standard PDF cards in JCPDS data base.

Scanning Electron Microscopy (SEM) Characterization:

The microstructure of powders as well as of CS densified pellets were observed by an FEI Quanta 650 FEG SEM. The accelerating voltage for SEM imaging is 10KV, spot size=4.

Density measurements

The densities of cold sintered pellets were measured by Archimedes' principle. Measured density of pellet can be calculated as $\rho_{measured} = \rho_{water} \cdot m_{dry}/(m_{dry} - m_{immersed})$. The relative density is calculated as $\rho_{relative} = \rho_{measured}/\rho_{theoretical}$. While the theoretical density of LLTO = 5 g/cm^3 and density of LMO= 4. 28 g/cm^3 according to the JCPDS data base.

5.3 Results and discussion.

Cold sintering of LLTO

The XRD results for LLTO densified by CS at 180℃ and 200°C are shown in Figure 5.3. By comparing XRD patterns with the pattern of LLTO raw powders as well as standard PDF card from JCPDS #870935, we confirm that there is no phase change during the cold sintering at both

temperatures. No extra peak has been identified. The XRD analysis of LLTO shows that CS at 200℃ will not lead to any phase change.

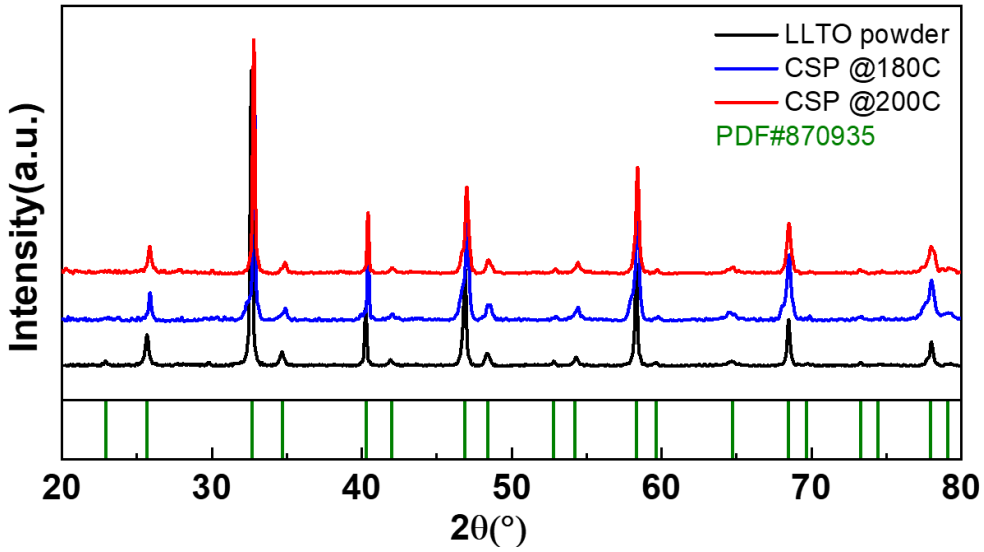

Figure 5.3 XRD pattern for LLTO raw powders, densified by cold sintering at 180℃ and 200℃. The diffraction patterns are compared with standard PDF card of LLTO (870935)

The densities of LLTO after cold sintering at 150℃, 180℃ and 200℃ are listed in Table 1. We can see that the relative densities increase at increased temperatures. At 200℃, the LLTO pellet reaches 90% density, which is higher than the 80% density reported for LAGP[134]. This means that LLTO is potentially a promising material that can be densified by CS. However, I need to mention that the theoretical density I use for calculation is based on standard PDF card in the data base. There might be some error as the theoretical density for my homemade powder could be different.

Table 5.1 Relative densities of LLTO pellets after cold sintering at different temperatures.

Processing temperature (°C)	Processing Time (mins)	Relative Density (%)
150	40	81
180	40	86
200	40	89

Scanning electron microscopy (SEM) have been applied to LLTO raw powders as well as pellets after CS at different temperatures. Images are shown in Figure 5.4 According to Figure 5.4(a), the particle size of homemade LLTO powder is about 1 μm. By comparing Figure 5.4(c), (e) and (g), we can see the relative density of the CS densified LLTO increased, which is verified by the results of the Archimedes' density measurements in Table 5.1. However, we noticed that there is still a very big gap in terms of density when comparing Spark Plasma Sintering (SPS) densified LLTO and cold pressed LLTO (Figure 5.4 (b), (d), (e), (f)). This suggests that cold sintering is not a very effective tool in consolidating particles when compared with SPS. Moreover, we can notice that the grain size of the pellets after CS remain to be about 1 μm, which confirms that grain growth is limited in CS. We also noticed that the microstructures in Figure 5.4 (d), (f) and (h) exhibit nonuniformity. Thus, some parts of the sample have greater density than the other parts. Two reasons could lead to such phenomena: (i) Water is not uniformly mixed with the powders. Thus, the region with more water has a higher density because water serves as lubricant in the first stage of the CS. (ii) Heat distribution is not homogeneous in the die, since we use a steel die and a cylindrical heater in the process. The upper/ bottom punches are also made of steel and the temperature of the punches should be lower than the die body. Therefore, there were two sources of heat, the die body and the punches, which results in an uneven temperature distribution inside the sample. Thus, the nonuniformity of the sample could lead to the formation of cracks and rupture of the pellet.

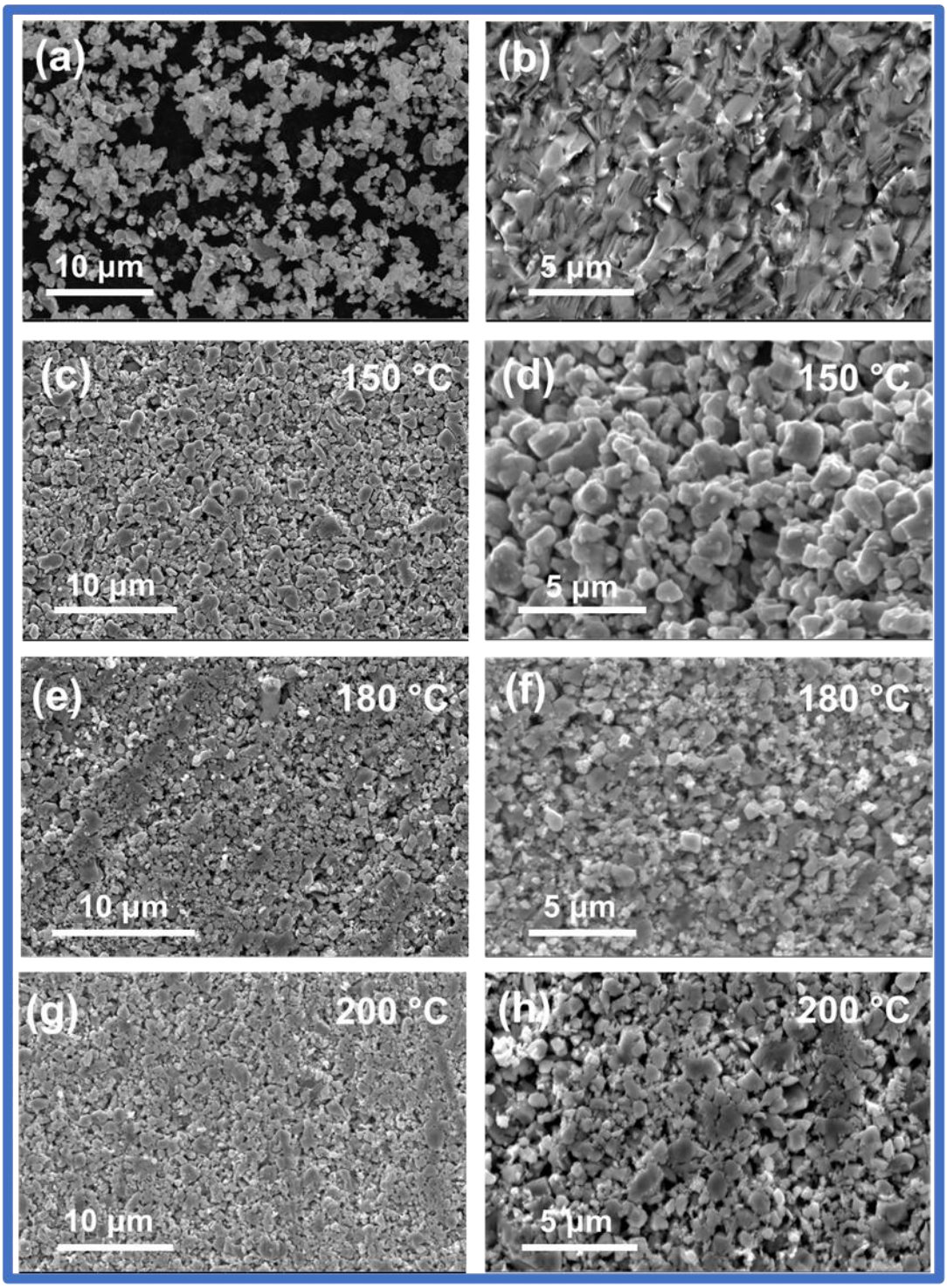

Figure 5.4 (a) SEM image of LLTO raw powders. (b) Fracture surface of SPS sintered LLTO. (c) Surface microstructure of LLTO pellet densified by CS at 150°C. (d) Higher magnification image of (c). (e)Surface microstructure of LLTO pellet densified by CS at 180°C. (f) Higher magnification image of (e). (g) Surface microstructure of LLTO pellet densified by CS at 200°C. (h) Higher magnification image of (e).

Cold sintering of LMO

Similar to LLTO, LMO pellets densified by CS and analyzed by XRD are shown in Figure 5.5. The diffraction patterns verify there is no phase change during CS of LMO. Therefore, we can conclude that cold sintering is a safe technique for LLTO and LMO densification and will not lead to any additional phase formation.

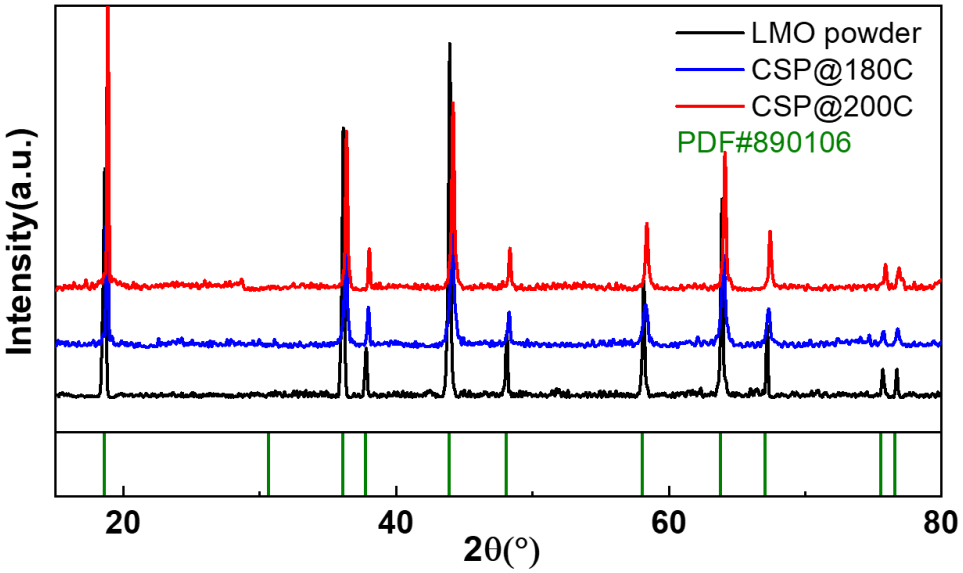

Figure 5.5 XRD pattern for LMO raw powders, LMO pellets densified by CS at 180℃ and 200℃. Diffraction patterns are compared with standard PDF card of LMO (890106).

For LMO, two types of powders with different particle sizes were densified by CS to verify the particle size effect on CS. SEM images of raw powders are shown in Figure 5.6 (a) and (b). Electrochemistry grade LMO (LMO 2, Figure 5.6 (b)) with a particle size of 5 μm is applied to compare with the LMO sample discussed in the XRD results. The previously analyzed LMO powder (LMO 1) has a particle size of about 200 nm. Relative densities of pellets in Figure 5.6 are listed in Table 5.2. Again, the theoretical density of LMO is obtained from JCPDS data base as 4.28 g/cm^3. First, by comparing Figure 5.6 (c)&(g), it is obvious that LMO powders with smaller particle size can reach a higher density at the same parameters. That is in good accordance with the common knowledge in sintering theory, which says that particles with smaller particle size have a larger driving force for densification. By comparing Figure 5.6 (d)&(f), we can see that the

density of the LMO 1 pellet at 200°C is higher than that of the LMO 1 pellet at 200°C. This again matches with the density measurement. However, nonuniformity of densification is still the biggest problem during CS densification of LMO. This have led to formation of cracks and even broken of the pellets.

Table 5.2 Relative densities of LMO pellets after cold sintering at different temperatures.

LMO powder type	Processing temperature (°C)	Processing Time (min)	Relative Density (%)
1	180	40	90
1	200	40	92
2	180	40	86

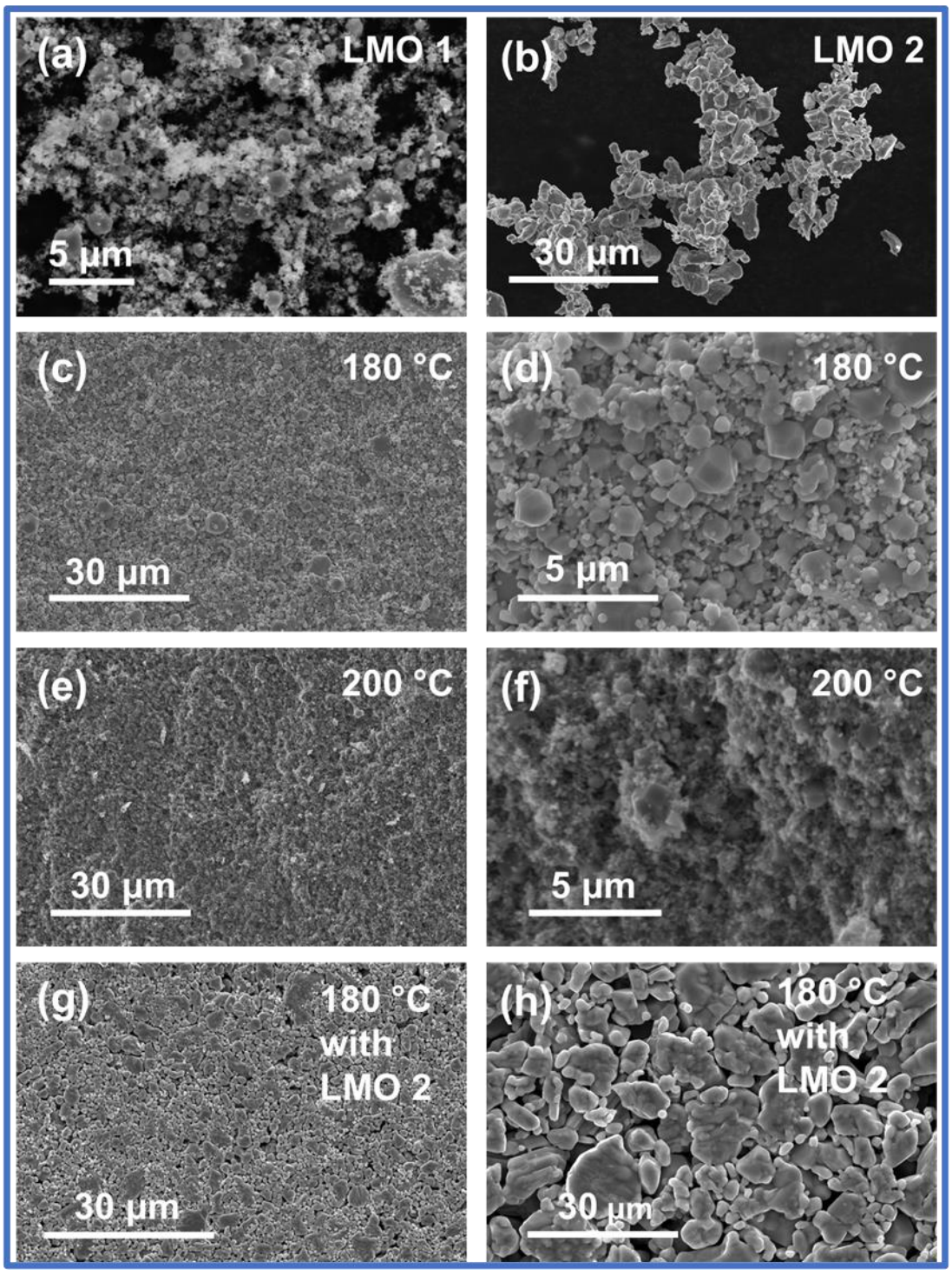

Figure 5.6 (a) LMO raw powder with particle size of about 300 nm (b) Electrochemistry grade LMO powder with particle size of about 5 µm. (c) Surface microstructure of LMO 1 pellet densified by CS at 180°C. (d) Higher magnification image of (c). (e) Surface microstructure of LMO 1 pellet densified by CS at 200°C. (f) Higher magnification image of (e). (g) Surface microstructure of LMO 2 pellet densified by CS at 180°C. (h) Higher magnification image of (g).

Cold sintering of LLTO/LMO half-cells

Based on the experience of densifying LLTO and LMO pellets respectively, a one-step CS, which is similar to SPS has been applied. The flow chart is shown in Figure 5.2. In this part, we used both LMO 1 and LMO 2 to compare the effect of density on the interfacial contact and interdiffusion phenomena. In this part, both half-cells were prepared at 200°C and 500MPa for 40 mins. SEM has been applied to the interfacial region for microsturctural observation. Further, EDS analysis also has been applied to detect the potential element interdiffusion at the interface. For SEM, we used the backscattering (BSE) mode, as it provides better contrast than secondary electron imaging between two different phases (LLTO and LMO).

The interfacial microstructure of LLTO/LMO half-cell densified by CS is shown in Figure 5.7(a). The LMO powder in this part was previous designated as LMO 1. We can observe from these images that LMO is denser than LLTO. The LLTO phase of the half cell is not as dense as the LLTO single pellet in Figure 5.4(g). From the higher magnification image of the interfacial region (Figure 5.7(b)), we can observe that the interfacial contact of the cold sintered samples is not good, and the interface is not sharp nor straight. We noticed the presence of some LMO particles in the LLTO phase region (red circle) as well, which is also indicative of insufficient interfacial contact in the CS densified sample. However, the half-cell prepared by CS showed limited interdiffusion. Based on element mappings shown in Figure 5.7(c), we observed a limited amount of Mn in the LLTO phase region, and limited Ti in the LMO phase. This result is very different from the EDS analysis of both the conventionally and SPS sintered samples. Moreover, the element fraction information of area 1 and area 2 in Table 5.3 verifies that there is limited interdiffusion, as there was no Mn detected in area 1 (LLTO phase) and negligible amount of Ti/La was detected in area 2 (LMO phase). Therefore, the CS is promising for the half cell processing since it could restrict the interdiffusion between cathode and eletrolyte. This in turn could potentially eliminate the formation of the previously discussed high resistance interphase. However, the poor interfacial contact, low density and nonuniformity of the pellet are the biggest challenges that need to be overcome when investigating cold sintering of such half-cells.

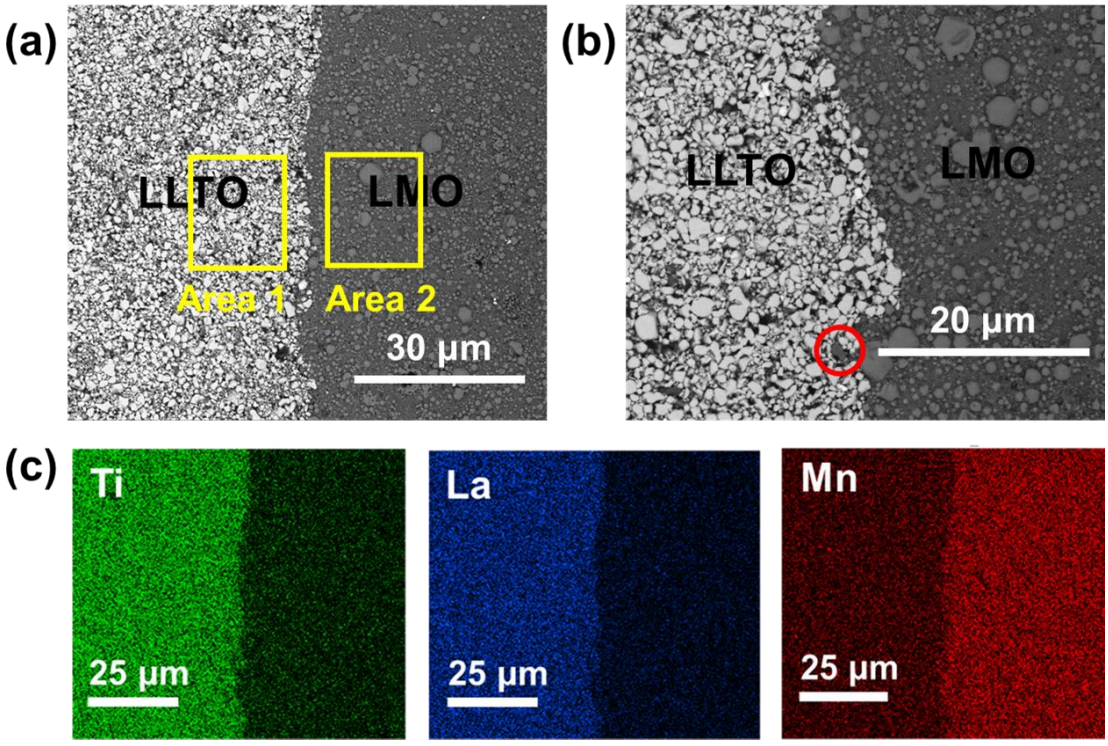

Figure 5.7 (a) Interfacial microstructure of CS densified LLTO/LMO half-cell prepared with LMO 1 powders. Atomic fraction of element in Area 1 and Area 2 are obtained by EDS area scans. (b) Higher magnification image of (a). (c) Element mappings of (a) obtained by EDS

The LMO 2 powder has also been used for half-cell preparation. The results are shown in Figure 5.8, and compared with the results in Figure 5.7. From Figure 5.8(a), we can notice that the LMO phase is less dense than the sample imaged in Figure 5.7(a). This again proves that a smaller particle size leads to better densified sample in CS. Moreover, the interfacial microstructure in Figure 5.8(b) proves that the contact is even worse, since the LMO phase is less dense. Both phases need to reach a high level of densification to obtain sufficient interfacial contact. Also, increasing the pressure applied to form the LLTO/LMO green pellet in Figure 5.2 could also improve the interfacial contact. The EDS mappings and area scans from Figure 5.8(c) and Table 5.3 again verify that the interdiffusion process in CS is inhibited.

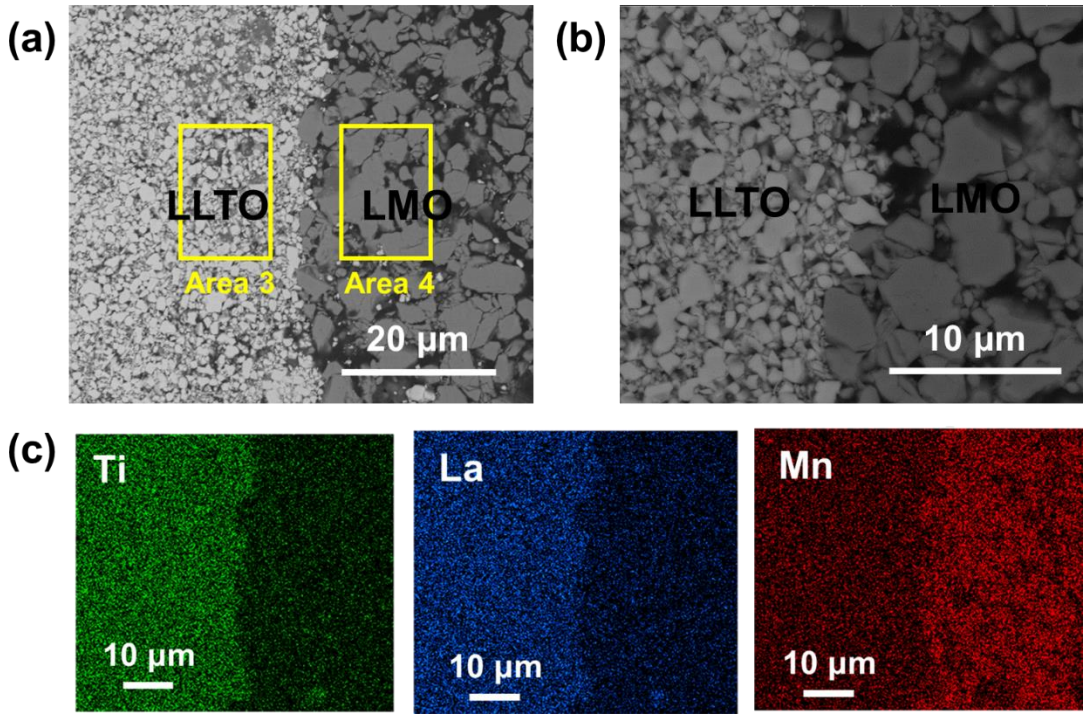

Figure 5.8 (a) Interfacial microstructure of CS densified LLTO/LMO half-cell, prepared with LMO 2 powders. Atomic fraction of elements in Area 3 and Area 4 are obtained by EDS area scans. (b) Higher magnification image of (a). (c) Element mappings of (a) obtained by EDS

Table 5.3 Atomic Percentage of elements for areas marked in Figure 5.8 (a), (b).

Atomic Percentage (%)				
Element	Area 1	Area 2	Area 3	Area 4
Mn	0	14.71	1.41	12.78
La	6.77	1.78	7.2	2.13
Ti	11.09	2.72	11.5	3.49
O	43.07	46.89	45.37	45.04
C	39.07	33.89	34.52	36.56

5.4 Conclusions and Future Plans

Cold sintering (CS) shows good potential for the densification of battery materials. The low processing temperature and short processing times could help mitigate interdiffusion processes and prevent the formation of high resistance phases at interfaces. Also, the initial powder particle

size changes very little during CS. Our experiment verifies the possibility of applying CS to electrolyte and electrode materials for solid state batteries. In our experiment, LLTO reached a relative density of about 90%, and LMO of 92% after CS at 200°C, 500MPa for 40 minutes. However, by comparing with the sample sintered by Spark Plasma Sinteirng (SPS), CS still has a long way to go to match the densification performance. There are a few ways that could improve the denisty:

1. Apply powders with smaller particle size. Our experiment with different LMO powders proves that smaller particle size could lead to a better CS density.
2. Increaing processing temperature. Our experiments for LLTO and LMO showed that higher temperature leads to a better CS density.
3. Increasing holding time. This needs to be balanced, as temperature and pressure are difficult to hold constant for a long time. This problem will be discussed in the next paragraph.

Briefly, longer holding time could lead to more uniform temperature inside the sample.

The quality of processing equipment has a significant influence on the last point. With the equipment available to us, we observed servere nonuniformty in CS samples, which we believe resulted in their low mechanical strength. Cracks and even repture have been observed in a large number of pellets, and as a result, no electrochemistry experiments (i.e. impedance measurements) have been performed on CS densified samples. Based on experimental experience, we listed a few possible solutions that could alleviate this situation:

1. Use a better press system that could hold the pressure at a constant value. The press we currently used is an oil press, which was a little bit too big for our experiment. During the experiment, the pressure would drop from time to time. Adding pressure mannually could break the sample.
2. Apply a program to control the temperature. In the previous experiment, the temperature is controled manually based on the read on thermocouples. However, the temperature could overshoot by tens of degrees after heating power is removed. That could lead to large temperature variations on the sample surface.
3. A more effective way of measuring temperature of the sample. The current experimental setup includes two thermocouples, one of which measures the heater temperature, and the

other measures the temperature of the punch. However, the punch temperature could be different from the temperature on the sample surface. Also as disucssed in previous section, the punches provided additional heat to the top and bottom surface of the sample, which could result in temperature nonuniformities.

4. A way to preserve heat. The die is made of steel and we applied wood planks between punches and press to isolate the heat transfer between press and die. However, the 200°C temperature could burn the planks and render it not as flat as when subjected to room temperature. Moreover, it should be better if this experiment could be performed inside a chamber to prevent heat exchange between die and air.

The cracking issue for the CS densified pellets should be alleviated after applying improvements as listed. The one-step CS preparation for half-cell also proves that cold sintering is a good tool in terms of restricting the high resistance interphase formation. If only we can solve the problem for better interfacial contact and higher density without cracking, CS would become a very promising tool for half-cell preparation.

CHAPTER 6. LLTO STABILITY AGAINST LITHIUM DENDRITES*

6.1 Introduction

Interfaces have become a critical bottleneck for the development of solid-state batteries (SSBs)[136]. In an inorganic SSB system, the cathode-electrolyte interface, anode-electrolyte interface, and interparticle interface all have great impact on Li-ion transportation in the batteries[137]. To understand the interfacial properties in solid-state batteries, it is necessary for us to study the anode-electrolyte interface. However, the lithium metal anode has drawn great attention among researchers, as it has a theoretical capacity of 3860 mAh/g, which is approximately ten times higher than that of traditional graphite anodes[138,139]. Li anode also possesses the lowest electrochemical potential of -3.04V vs SHE (Standard Hydrogen Electrode); therefore, the Li metal anode has been widely considered as the ultimate choice for anode material for SSBs[140]. However, the formation of Li dendrites into electrolytes has been a major roadblock for the practical use of Li metal anode, as it could lead to short circuit and significant capacity loss of the battery[141]. It is thus necessary to understand and suppress dendrite formation at the anode-electrolyte interface. Solid electrolytes have been considered as the solution for suppression of lithium dendrites for a long time. Monroe and Newman proposed that dendrite formation can be suppressed if the shear modulus of a separator is twice than that of lithium (3.4GPa).[142] Based on that, ceramic solid electrolytes, which usually have mechanical strengths of more than 100GPa are considered as the solution for suppressing lithium dendrite formation against lithium metal anodes[95]. However, further studies on solid electrolyte materials reveal that lithium dendrites can still form and penetrate SE during cycling and result in short circuit of batteries. Therefore, studying the stability of $Li_{0.33}La_{0.57}TiO_3$(LLTO) against lithium metal anode could be necessary for making LLTO a feasible material to be practically applied to solid state batteries design.

Current studies of solid electrolytes interfacing with Li reveal that the critical current density (CCD), which is the highest current density allowed before short-circuit, for the solid electrolyte $Li_7La_3Zr_2O_{12}$(LLZO) is usually below 1mA/cm^2, which is even lower than batteries with traditional organic liquid electrolyte[143,144]. This indicate that the dendrite formation in solid state batteries could not be suppressed simply by applying any high shear modulus ceramic SEs. For ceramic solid electrolytes, several factors could still result in dendrite growth[145]: (i) the poor

interfacial contact between electrolyte and Li anode; poor contact would generate voids at the interface so that dendrites can grow within these holes[146]; (ii) the porosity of solid electrolytes; pores inside solid electrolytes can also led to dendrite growth inside them[147]; (iii) different ionic conduction efficiency between grain and grain boundaries[148]; for example, in LLZO, grain boundaries are reported to have higher ionic resistance than grains[149]; that could result in propagation of lithium dendrite along grain boundaries. In addition to the danger of the short-circuit, dendrite growth could also lead to lithium loss and result in a low columbic efficiency of the battery.

Despite a large body of literature on LLZO aiming to reveal the fundamentals of dendrite growth in solid electrolyte, the dendrite formation and growth mechanism is still not fully understood. On the other hand, $Li_{0.33}La_{0.57}TiO_3$ (LLTO) has been reported as unstable against lithium metal anode[150,151]. The reasons behind this is that Ti^{4+} in LLTO can be reduced by lithium and form Ti^{3+} at low potential values. However, there is still very limited information about the reaction products and their effect on battery performance. Moreover, in recent work that Xiao group reported[152], they observed that, at $Li_2O–Al_2O_3–P_2O_5–TiO_2–GeO_2$ (LATP)/Li interface, an interfacial layer would form and alleviate the growth of Li dendrite. The CCD for LATP is much higher than that of LLZO. This is a conflicting result, since researchers used to believe such reduction reaction of Ti^{4+} could not impede dendrite growth[152]. Thus, studying the stability of LLTO against Li anode could not only reveal a more fundamental understanding of LLTO and Li reaction, but also potentially provide new insights for Li metal anode batteries in the future.

The stability of electrolytes against Li metal is tested through cycling experiments in Li/electrolyte/Li symmetric cells [144,153,154]. Dendrites are expected to form inside the electrolyte during stripping/ plating of Li and cause short-circuit while penetrating the electrolyte. The materials with higher critical current densities are conventionally believed to have stronger resistance against Li dendrites[155]. However, a term called “Soft shorts”[156] was put forward, in which the potential of batteries will not drop to zero as the dendrite penetrates the electrolyte when the thickness of Li electrodes are thicker than 30 μm. Newman mentioned that we can check for this “soft short” by analyzing impedance spectroscopy[156]. However, in literature, there are limited studies on symmetric cells using Li and LLTO. In such systems, the dendrite formation mechanism is not understood. Thus, this work aims to shed light on the Li/LLTO/Li cell performance.

6.2 Experimental

Powder Synthesis:

$Li_{0.33}La_{0.57}TiO_3$ (LLTO) powders were prepared via the same solid state reaction method described in previous chapters. The particle size of LLTO powder after sieving was 1 μm. $Li_{6.4}La_3Zr_{1.4}Ta_{0.6}O_{12}$ (Ta-doped LLZO) was commercially available from MSE Supplies, as Ampcera™ LLZO Nano-Powder Ta-Doped Lithium Lanthanum Zirconate Garnet, 500nm.

Ceramic electrolyte pellets preparation

LLTO pellets were sintered by Spark Plasma Sintering (SPS) in vacuum at 800℃ and 50MPa for 10 minutes with heating/cooling rate of 100℃/min. The sintered pellets then went through a re-heating process to remove the oxygen vacancies created during SPS, which was carried out in an MTI corporation tube furnace at 750℃ for 1 hour in air. After that, pellets were polished with 320 and 800 Grit SiC paper to the thickness of 0.7 mm. The diameters of LLTO pellets were of 10mm. The relative density of LLTO pellets after SPS was >95% according to Archimedes' measurements.

Ta-doped LLZO (LLZTO) pellets were sintered by Spark Plasma Sintering (SPS) in vacuum at 950℃, 30MPa for 20 minutes with heating rate of 100℃/min and cooling rate of 50℃/min. The sintered pellets also go through the reheating at 750℃ for 1 hour in air to eliminate the effect of oxygen vacancies. After that, LLZTO pellets were polished by 320 and 800 Grit SiC paper to the thickness of 0.7 mm. The diameters of LLTO pellets are 10mm. Relative density of LLZTO pellets after SPS is >95% according to Archimedes' measurement.

Battery Assembly:

Lithium electrodes were cut by a 7/32 inch punch from Lithium foil (GF47159826, Sigma Aldrich) in an Ar filled glovebox. Then, the Li symmetric cells were assembled as shown in Figure 6.1(a). A Li/LLTO/Li sandwich (Figure 6.1(b)) was pressed and heated on a hot plate at 170℃ for 30 seconds each side. Then, two Φ=3/8 inch, 0.5mm thick stainless steel plates were placed on both sides of Li/electrolyte/Li sandwich, respectively, and sealed into a 2032 coin cell by an MTI Hydraulic Crimper with a spring on the anode side.

Battery testing

The Li/electrolyte/Li batteries were heated in an oven at 80℃ overnight. Next, the cells went through a direct current (DC) Galvanostatic rating cycling with a Landt battery system. The cell started cycling at a current density of 0.05mA/cm^2 for 5 cycles (1 hour/ cycle), then the current density increased with rate (0.1, 0.2, 0.3, 0.4, 0.5, 1, 2, 3, 4, 5, 6, 7, 8, 9. 10 mA/cm^2) for 5 cycles, respectively. The impedance of batteries before and after cycling was measured by a potentiostat, with frequency from 1MHz to 0.1Hz.

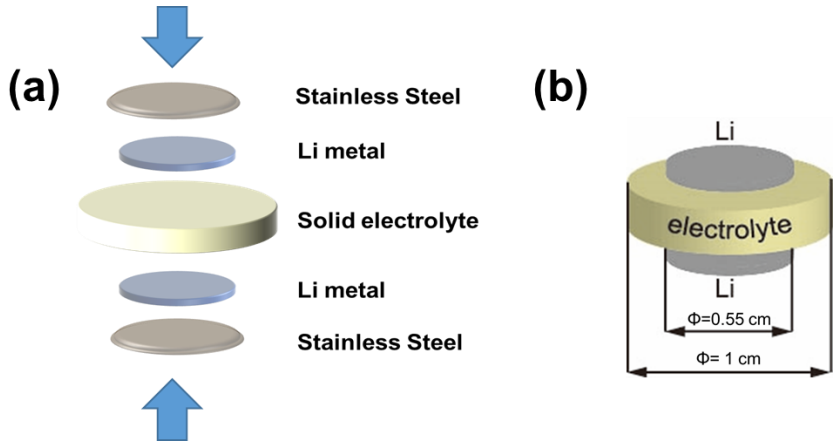

Figure 6.1 Schematic of Li/solid electrolyte/ Li symmetric cell.

Microstructure Characterization:

Microstructures of pellets before and after cycling were characterized by a FEI Quanta 650 SEM.

6.3 Results and discussion:

Homemade LLTO powders with particle sizes of about 1μm (Figure 6.2(a)) were sintered by SPS (Figure 6.2(b)) at 800℃ and the relative densities of sintered pellets are >95% according to Archimede's method. Commercial Ta-doped LLZO (LLZTO) powders with particle size of 500nm (Figure 6.2(c)) were also sintered by SPS, the relative densities of sintered pellets (Figure 6.2(d)) were >95% according to Archimede's method. This again proves SPS is a good tool for densifying electrolyte materials. The pellets can reach a high relative density with considerably short processing time compared with hot pressing and conventional sintering. The short processing

time can minimize grain growth during sintering. The lithium loss during high temperature sintering is also greatly reduced with the shorter processing time, which is beneficial for lithium conduction in solid electrolyte.

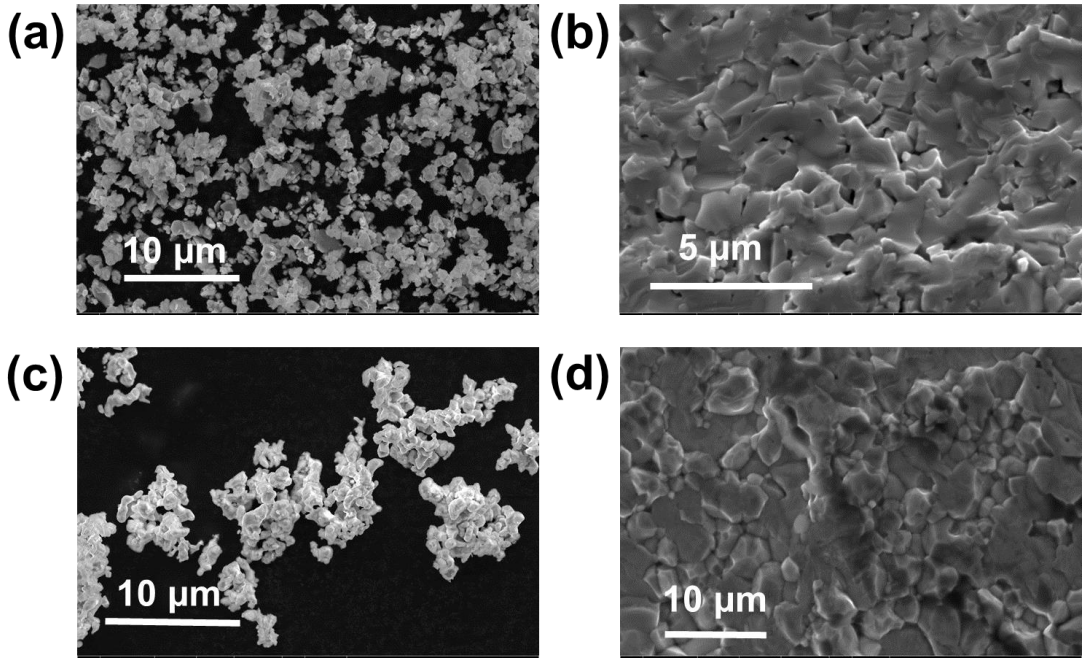

Figure 6.2 (a) SEM image of LLTO powders. (b) Fractured surface microstructure of LLTO sintered by SPS. (c) SEM of Ta-doped LLZTO powders. (d) Fractured surface of Ta-doped LLZTO pellet sintered by SPS

Li/LLTO/Li symmetric cells were assembled to test the durability of LLTO against Li dendrite. The cells were cycled with increasing current densities. It is obvious that LLTO is not stable against Li, as the LLTO pellet becomes dark just a few seconds after in contact with Li electrode (Figure 6.3). The color change is also observed on backside of LLTO pellet, which indicates the reaction is quite rapid. After cycling, the pellet become completely dark as shown in Figure 6.3. However, despite the reaction which has been reported as the reduction of Ti^{4+}, surprisingly, LLTO exhibits great stability during cycling experiments. Figure 6.4(a) shows the Galvanostatic cycling profile for Li/LLTO/Li symmetric cells. The cell is cycled with increasing current densities (0.05, 0.1, 0.2, 0.3, 0.4, 0.5, 1, 2, 3, 4, 5, 6, 7, 8, 9, 10 mA/cm^2). For each current density, the cell run for 5 cycles (1 hour/ cycle). The voltage response is recorded. Based on the voltage profile, we observed an obvious voltage drop at first two cycles, which we believe is due

to the improved interfacial contact between LLTO/ Li as lithium plating and stripping during charging/discharging stages. The voltage response is connected to the increase in current density, which proves that there is no short circuit in LLTO even at the high current density of 10 mA/cm^2. To further prove the cycling stability of LLTO, the cell was cycled with 10 mA/cm^2 for another 450 hours. From the cycling profile in Figure 6.4(b), the polarization potential of the cell dropped from 0.2V to 0.1V, indicating there is a decrease in resistance for the cell. To future eliminate the possibility of "soft circuit" for our LLTO electrolyte, impedance profiles of the cell after 45 cycles and 500 cycles were measured and compared with the initial impedance. We can see the impedance of the cell decreased significantly, from 4500 Ω to 250Ω. We have measured the impedance of the LLTO single pellet, which is about 2600Ω, in the Chapter 4, the current 250 Ω value is by far lower than the resistance of bulk LLTO. This indicates that the reaction product of at the LLTO/Li interface has lower resistance compared with the LLTO bulk phase. Moreover, the impedance of the cell after 500 cycle drops to 50Ω, which further proves that the reaction product could help Li conduction inside the ceramic electrolyte. The impedance profile shows a complete imaginary loop, which eliminate the possibility of "soft short" in this cell.[156] Therefore, it is evident that the LLTO has great stability and is able to prevent Li penetration. Moreover, the reaction product shows even better conduction ability compared with the individual LLTO phase. This is different than reported for another electrolyte material, LATP[157], for which resistance increased as the reaction proceeded, and the reaction could lead to the failure of the entire battery.

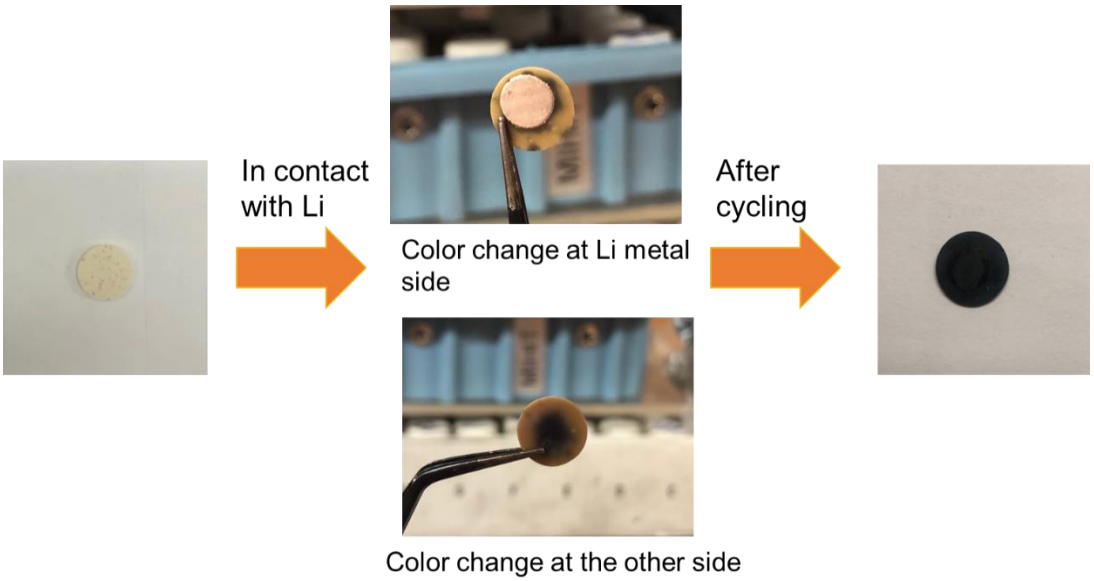

Figure 6.3 Color change in LLTO pellet after in contact with Li metal electrode

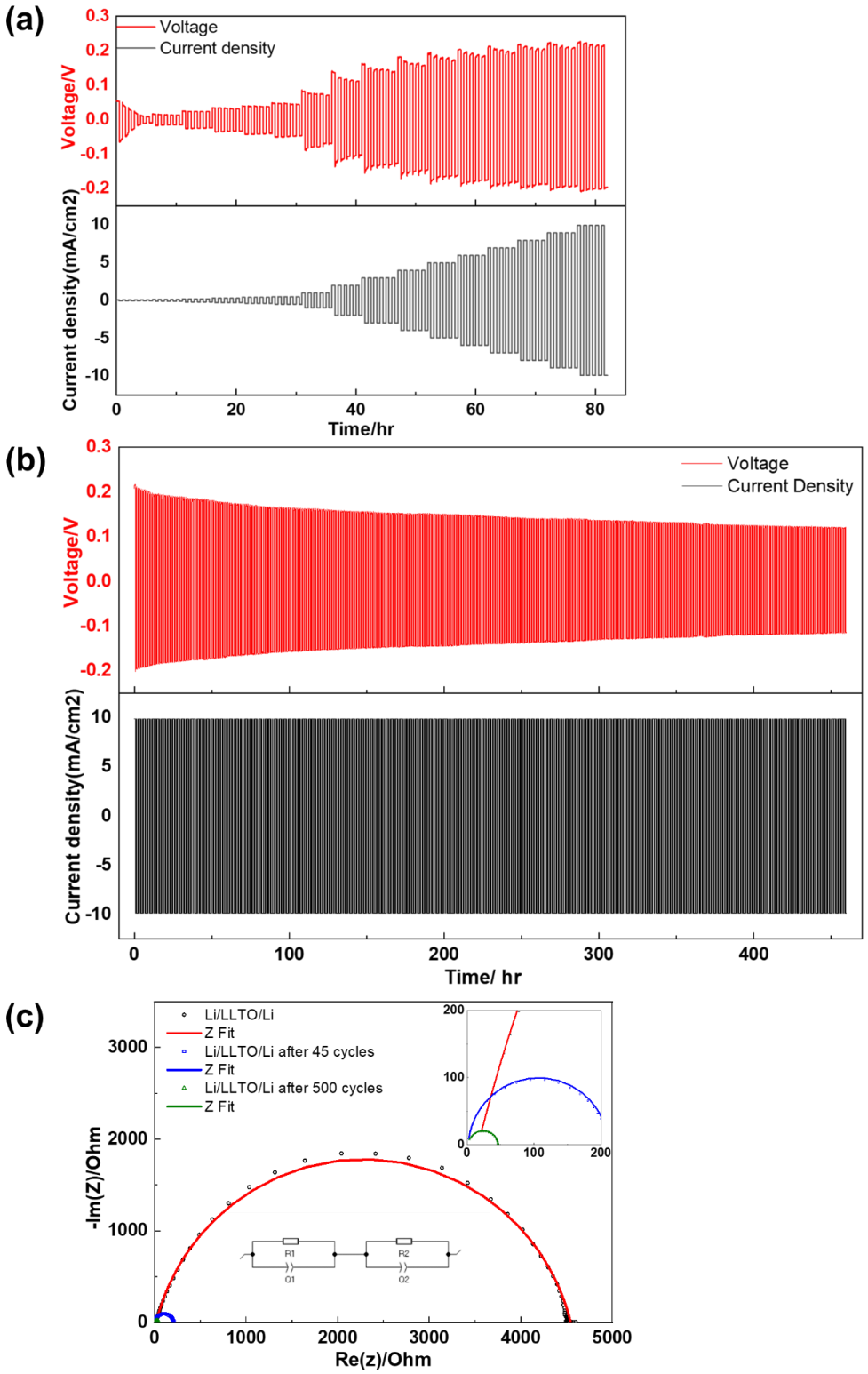

Figure 6.4 (a) Galvanostatic cycling of Li/LLTO/Li cell with increasing current densities at room temperature. (b) Galvanostatic cycling of Li/LLTO/Li cell with current density of 10 mA/cm^2 for another 450 hours after (a). (c) Impedance measurement of Li/LLTO/Li cell after assembly, after 45 cycles and after 500 cycles

To compare with LLTO performance, a symmetric cell with Li/LLZTO/Li has been assembled and run through a similar Galvanostatic cycling program. The voltage profile is shown in Figure 6.5(a). In the LLZO cell, we observed an obvious polarization drop at a current density of 0.4 mA/cm^2, which is similar to the CCD value for LLZO reported in literature[158,159]. After disassembling the cell, we observed clear Li dendrite formation on both sides of the pellet as shown in Figure 6.5(b). The impedance profile for Li/LLZTO/Li before and after cycling in Figure 6.5(c), (d) proves that the dendrite has penetrated the electrolyte and caused a short circuit of the cell. By comparing the Galvanostatic cycling profile of LLTO and LLZTO, it is evident that the LLTO/Li reaction could prevent Li dendrites from penetrating the electrode, which is very important for the solid state battery safety. The reduced resistance for LLTO after cycling also suggests it could potentially help improving the electrolyte stability against Li electrode.

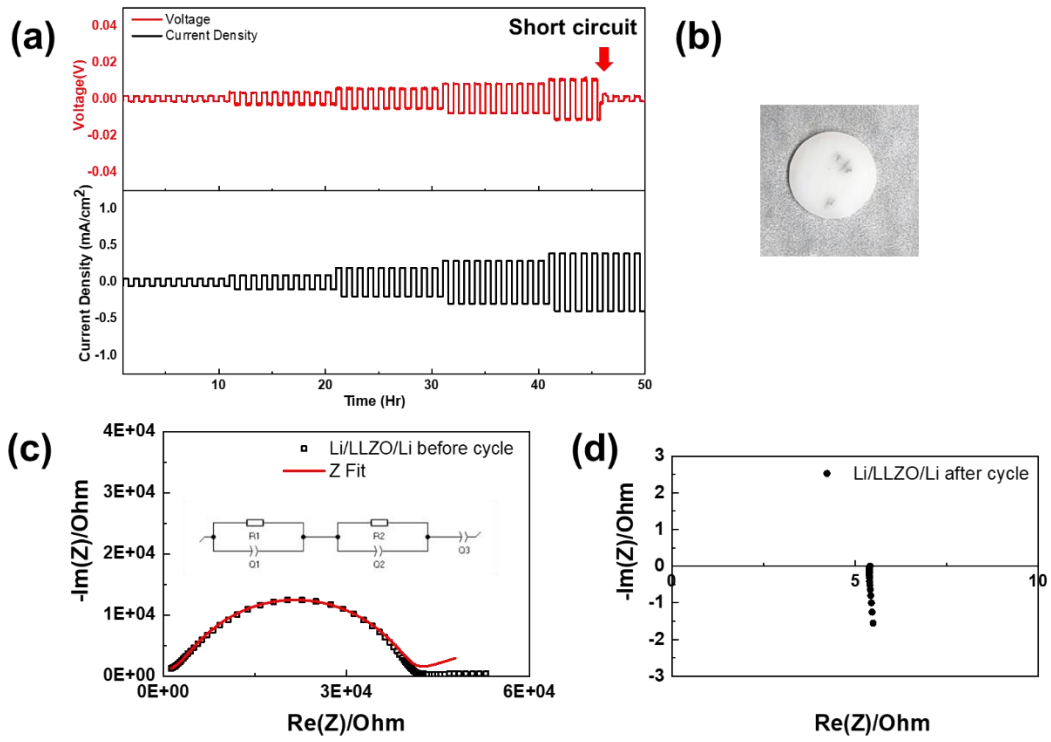

Figure 6.5 (a) Galvanostatic cycling of Li/LLZTO/Li symmetric cells. (b) LLZO pellet after cycling. (c) Impedance measurement of Li/LLZTO/Li cell before cycle (d) Impedance measurement of Li/LLZTO/Li cell after cycle.

SEM observations have been applied to the fractured surface of LLTO after cycling. Backscattered electron (BSE) detector is a powerful tool in recognizing Li dendrite formation within ceramic pellets as it reveals Z contrast. Li dendrite content should have a lower atomic weight compared with LLTO bulk phase. Therefore, the black clusters are believed to be Li dendrite content. From Figure 6.6, we can see at the fractured surface, the Li content clusters doesn't connect, which again explains why we did not observe short circuit within Li/LLTO/Li cells. EDS mapping in Figure 6.6(c) also reveals that the La, Ti, and O concentration are all lower in the dark spots, indicating the dark spots should have higher lithium concentration. However, further detailed characterization is needed to narrow down the composition of this dark phase.

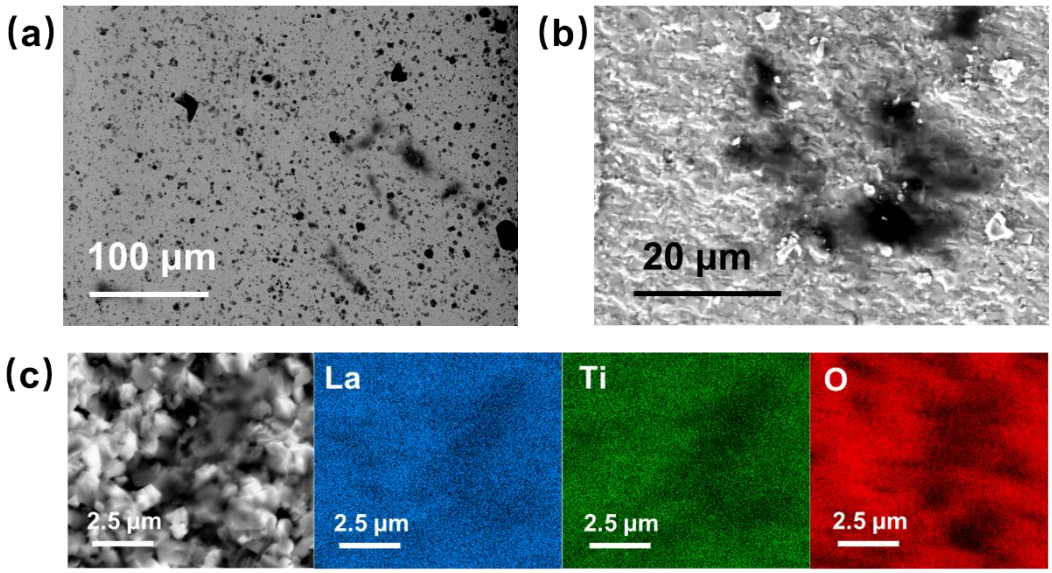

Figure 6.6 (a) Fractured surface of LLTO after cycling, obtained by backscattered electron detector. (b) Higher magnification image of (a). (c) Element concentration mappings of the dark spots, obtained by EDS.

6.4 Conclusions and Future Plans

So far, the galvanostatic cycling of the Li/LLTO/Li revealed two important facts: (i) Li will have a reduction reaction with LLTO, which makes LLTO pellets turn into dark color. This reaction has been discussed by Wenzel[151] and Yang[160], they applied XPS measurement to the LLTO after reaction with lithium. Yang concluded that in the reaction, Ti^{4+} is reduced to Ti^{3+} and that leads to an electric field assisted Li insertion into A site (Li/La site) vacancies in the perovskite LLTO structure. That can result in an increase in conductivity for LLTO[160]. This result matches

our observation that the impedance of the cell decreased significantly after cycling, indicating the reaction product can increase conductivity. (ii) LLTO shows great stability at high current density (10 mA/cm^2) cycling. As the reaction consumes lithium, and results in its insertion into perovskite LLTO, it is reasonable to speculate that the lithium dendrite is consumed because of this reaction. Thus, LLTO can prevent Li dendrite penetration, which could potentially solve the safety biggest roadblock standing in the way of using Li metal anodes in solid state batteries. This discovery may overturn the common knowledge that LLTO cannot be successfully used in such devices.

However, future work is needed to further prove the feasibility of applying LLTO together with Li anode in solid state batteries. Most importantly, solving the cathode/electrolyte contact problem and creating a full-cell for charge/discharge cycling testing would be the next step in this research. Also, it is important to further look into the chemical composition of dark clusters we observed via SEM (Figure 6.6). EELS method in the transmission electron microscope, and EDS could shed further light on this problem.

CHAPTER 7. SUMMARY AND FUTURE PERSPECTIVES

In this thesis, we focused on the interfacial phenomena, which has been a significant obstacle that hinders the development of solid-state lithium ion batteries. Both cathode/electrolyte and anode/electrolyte interface were studied.

For cathode/electrolyte interfaces, we proposed a novel half-cell preparation procedure via spark plasma sintering (SPS). With SPS, both cathode and electrolyte materials can reach high densities within 10 minutes of processing time. The interfacial contact is improved as well with this method, compared to other sintering methods. We selected oxide electrolyte materials, LLTO and LATP, and prepared half-cells with commercial cathode materials. LLTO/LMO, LATP/LMO and LLTO/LCO half-cells were fabricated and investigated. We applied electron microscopy methods and impedance spectroscopy to investigate the origin of large interfacial resistance in these half-cell systems. The results showed that the ion interdiffusion between cathode and electrolyte will introduce a micron-thick layer, which has a resistance of the order of 10^5 Ω. Such large resistance is detrimental for battery performance and needs to be eliminated. To suppress the interdiffusion layer between cathode and electrolyte, we investigated a novel low temperature densification technique: cold sintering. This method shows great potential from preliminary results, as it was successful suppressing temperature driven interdiffusion. However, the ceramics' relative densities need to be improved if we want to further apply this technique to half-cell preparation. Our study reveals the origin of large interfacial resistance in cathode/electrolyte half-cells. Moreover, it not only explains one of the reasons behind SSB failure, but can also serve as guidance for material selection for cathode/electrolyte pairs.

For anode/electrolyte interface studies, we looked into the most important obstacle standing in the way of using lithium metal anode in solid state batteries: dendrite formation. We discovered that choosing LLTO as the solid state electrolyte provides great stability against Li dendrite formation, even at very large current densities. The reaction products of LLTO and Li were proved to have higher conductivity than the single LLTO phase. This overturns the common knowledge that LLTO cannot be used in lithium metal batteries, and provide a new path for dendrite prevention.

For future work that could follow up these findings, the cold sintering results exhibit great potential in suppressing the high resistance interdiffusion layer. However, the main challenges for

applying cold sintering to half-cell preparation are: (1) the densities of cathode and electrolyte phases are not high enough to provide good mechanical strength as well as good ionic conduction, and (2) inadequate interfacial contact between cathode and electrolyte. Based on this study, we propose that by refining temperature and pressure control, the cold sintering density as well as interfacial contact can improve. On the other hand, LLTO exhibits great stability against lithium dendrite formation, and thus future experiments could be designed where LLTO is employed as electrolyte material toward the preparation and testing of a Li/LLTO/cathode full cell. This experiment could shed light on the feasibility of solving dendrite problem with LLTO electrolyte.

REFERENCE

(1) Dunn, B.; Kamath, H.; Tarascon, J.-M. Electrical Energy Storage for the Grid: A Battery of Choices.

(2) Janek, J.; Zeier, W. G. A Solid Future for Battery Development. *Nat. Energy* **2016**, *1* (9).

(3) Manthiram, A.; Yu, X.; Wang, S. Lithium Battery Chemistries Enabled by Solid-State Electrolytes. *Nat. Rev. Mater.* **2017**, *2* (4), 1–16.

(4) Wen, J.; Yu, Y.; Chen, C. A Review on Lithium-Ion Batteries Safety Issues: Existing Problems and Possible Solutions. *Mater. Express* **2012**, *2* (3), 197–212.

(5) Takada, K.; Ohno, T.; Ohta, N.; Ohnishi, T.; Tanaka, Y. Positive and Negative Aspects of Interfaces in Solid-State Batteries. *ACS Energy Lett.* **2018**, *3* (1), 98–103.

(6) Yu, C.; Ganapathy, S.; Eck, E. R. H. V.; Wang, H.; Basak, S.; Li, Z.; Wagemaker, M. Accessing the Bottleneck in All-Solid State Batteries, Lithium-Ion Transport over the Solid-Electrolyte-Electrode Interface. *Nat. Commun.* **2017**, *8* (1), 1–9.

(7) Richards, W. D.; Miara, L. J.; Wang, Y.; Kim, J. C.; Ceder, G. Interface Stability in Solid-State Batteries. *Chem. Mater.* **2016**, *28* (1), 266–273.

(8) Li, Y.; Zhou, W.; Chen, X.; Lü, X.; Cui, Z.; Xin, S.; Xue, L.; Jia, Q.; Goodenough, J. B. Mastering the Interface for Advanced All-Solid-State Lithium Rechargeable Batteries. *Proc. Natl. Acad. Sci.* **2016**, *113* (47), 13313–13317.

(9) Tarascon, J.-M.; Armand, M. Issues and Challenges Facing Rechargeable Lithium Batteries. *Nature* **2001**, *414* (6861), 359–367.

(10) Yamada, H.; Suzuki, K.; Nishio, K.; Takemoto, K.; Isomichi, G.; Moriguchi, I. Interfacial Phenomena between Lithium Ion Conductors and Cathodes. *Solid State Ionics* **2014**, *262*, 879–882.

(11) Kamaya, N.; Homma, K.; Yamakawa, Y.; Hirayama, M.; Kanno, R.; Yonemura, M.; Kamiyama, T.; Kato, Y.; Hama, S.; Kawamoto, K.; et al. A Lithium Superionic Conductor. *Nat. Mater.* **2011**, *10* (9), 682–686.

(12) Mizuno, F.; Hayashi, A.; Tadanaga, K.; Tatsumisago, M. New, Highly Ion-Conductive Crystals Precipitated from Li 2S-P2S5 Glasses. *Adv. Mater.* **2005**, *17* (7), 918–921.

(13) Ohta, N.; Takada, K.; Zhang, L.; Ma, R.; Osada, M.; Sasaki, T. Enhancement of the High-Rate Capability of Solid-State Lithium Batteries by Nanoscale Interfacial Modification. *Adv. Mater.* **2006**, *18* (17), 2226–2229.

(14) Sun, C.; Liu, J.; Gong, Y.; Wilkinson, D. P.; Zhang, J. Recent Advances in All-Solid-State Rechargeable Lithium Batteries. *Nano Energy* **2017**, *33* (January), 363–386.

(15) Huggins, R. A. *Advanced Batteries*; 2009; Vol. 1.

(16) Anwane, S. W. Solid Electrolytes: Principles and Applications. In *Advanced Energy Materials*; 2014; Vol. 9781118686, pp 259–294.

(17) Callister, W. D. MATERIALS SCIENCE AND ENGINEERING: An Introduction. *Mater. Sci. Eng. An Introd.* **2003**, *8*, 101.

(18) Bachman, J. C.; Muy, S.; Grimaud, A.; Chang, H. H.; Pour, N.; Lux, S. F.; Paschos, O.; Maglia, F.; Lupart, S.; Lamp, P.; et al. Inorganic Solid-State Electrolytes for Lithium Batteries: Mechanisms and Properties Governing Ion Conduction. *Chem. Rev.* **2016**, *116* (1), 140–162.

(19) Inaguma, Y.; Liquan, C.; Itoh, M.; Nakamura, T.; Uchida, T.; Ikuta, H.; Wakihara, M. High Ionic Conductivity in Lithium Lanthanum Titanate. *Solid State Commun.* **1993**.

(20) Yao, X.; Huang, B.; Yin, J.; Peng, G.; Huang, Z.; Gao, C.; Liu, D.; Xu, X. All-Solid-State Lithium Batteries with Inorganic Solid Electrolytes: Review of Fundamental Science. *Chinese Phys. B* **2015**, *25* (1), 1–14.

(21) Stramare, S.; Thangadurai, V.; Weppner, W. Lithium Lanthanum Titanates: A Review. *Chem. Mater.* **2003**, *15* (21), 3974–3990.

(22) Bohnke, O.; Bohnke, C.; Fourquet, J. L. J. Mechanism of Ionic Conduction and Electrochemical Intercalation of Lithium into the Perovskite Lanthanum Lithium Titanate. *Solid State Ionics* **1996**.

(23) Itoh, M.; Inaguma, Y.; Jung, W. H.; Chen, L.; Nakamura, T. High Lithium Ion Conductivity in the Perovskite-Type Compounds Ln1 2Li1 2TiO3(Ln=La,Pr,Nd,Sm). *Solid State Ionics* **1994**.

(24) Cussen, E. J. Structure and Ionic Conductivity in Lithium Garnets. *J. Mater. Chem.* **2010**, *20* (25), 5167–5173.

(25) Cussen, E. J.; Yip, T. W. S.; Oneill, G.; Ocallaghan, M. P. A Comparison of the Transport Properties of Lithium-Stuffed Garnets and the Conventional Phases Li3Ln3Te2O12. *J. Solid State Chem.* **2011**, *184* (2), 470–475.

(26) Murugan, R.; Thangadurai, V.; Weppner, W. Fast Lithium Ion Conduction in Garnet-Type Li7La 3Zr2O12. *Angew. Chemie - Int. Ed.* **2007**, *46* (41), 7778–7781.

(27) Awaka, J.; Takashima, A.; Kataoka, K.; Kijima, N.; Idemoto, Y.; Akimoto, J. Crystal Structure of Fast Lithium-Ion-Conducting Cubic $Li_7La_3Zr_2O_{12}$. *Chem. Lett.* **2011**, *40* (1), 60–62.

(28) Xia, W.; Xu, B.; Duan, H.; Tang, X.; Guo, Y.; Kang, H.; Li, H.; Liu, H. Reaction Mechanisms of Lithium Garnet Pellets in Ambient Air: The Effect of Humidity and CO2. *J. Am. Ceram. Soc.* **2017**, *100* (7), 2832–2839.

(29) Hagman, L. O.; Kierkegaard, P. The Crystal Structure of NaMe2(PO4)3; Me=Ge, Ti, Zr. *Acta Chemica Scandinavica*. 1968, pp 1822–1832.

(30) Arbi, K.; Tabellout, M.; Lazarraga, M. G.; Rojo, J. M.; Sanz, J. Non-Arrhenius Conductivity in the Fast Lithium Conductor Li1.2Ti1.8Al0.2(PO4)3: A Li7 NMR and Electric Impedance Study. *Phys. Rev. B - Condens. Matter Mater. Phys.* **2005**, *72* (9), 1–8.

(31) Aono, H.; Sugimoto, E. Ionic Conductivity of Solid Electrolytes Based on Lithium Titanium Phosphate. *J Electrochem Soc* **1990**, *137* (4), 1023–1027.

(32) Koerver, R.; Aygün, I.; Leichtweiß, T.; Dietrich, C.; Zhang, W.; Binder, J. O.; Hartmann, P.; Zeier, W. G.; Janek, J. Capacity Fade in Solid-State Batteries: Interphase Formation and Chemomechanical Processes in Nickel-Rich Layered Oxide Cathodes and Lithium Thiophosphate Solid Electrolytes. *Chem. Mater.* **2017**, *29* (13), 5574–5582.

(33) An, S. J.; Li, J.; Daniel, C.; Mohanty, D.; Nagpure, S.; Wood, D. L. The State of Understanding of the Lithium-Ion-Battery Graphite Solid Electrolyte Interphase (SEI) and Its Relationship to Formation Cycling. *Carbon N. Y.* **2016**, *105*, 52–76.

(34) Wang, A.; Kadam, S.; Li, H.; Shi, S.; Qi, Y. Review on Modeling of the Anode Solid Electrolyte Interphase (SEI) for Lithium-Ion Batteries. *npj Comput. Mater.* **2018**, *4* (1).

(35) Goodenough, J. B.; Kim, Y. Challenges for Rechargeable Li Batteries. *Chem. Mater.* **2010**, *22* (3), 587–603.

(36) Gao, J.; Shi, S.-Q.; Li, H. Brief Overview of Electrochemical Potential in Lithium Ion Batteries. *Chinese Phys. B* **2016**.

(37) Hayashi, K.; Nemoto, Y.; Tobishima, S. I.; Yamaki, J. I. Mixed Solvent Electrolyte for High Voltage Lithium Metal Secondary Cells. *Electrochim. Acta* **1999**, *44* (14), 2337–2344.

(38) Zhang, X.; Kostecki, R.; Richardson, T. J.; Pugh, J. K.; Ross, P. N. Electrochemical and Infrared Studies of the Reduction of Organic Carbonates. *J. Electrochem. Soc.* **2001**.

(39) Li, J.; Ma, C.; Chi, M.; Liang, C.; Dudney, N. J. Solid Electrolyte: The Key for High-Voltage Lithium Batteries. *Adv. Energy Mater.* **2015**, *5* (4), 1401408.

(40) Chong, J.; Xun, S.; Song, X.; Liu, G.; Battaglia, V. S. Surface Stabilized LiNi0.5Mn1.5O4cathode Materials with High-Rate Capability and Long Cycle Life for Lithium Ion Batteries. *Nano Energy* **2013**, *2* (2), 283–293.

(41) Mohanty, D.; Huq, A.; Payzant, E. A.; Sefat, A. S.; Li, J.; Abraham, D. P.; Wood, D. L.; Daniel, C. Neutron Diffraction and Magnetic Susceptibility Studies on a High-Voltage Li1.2Mn0.55Ni0.15Co0.10O 2 Lithium Ion Battery Cathode: Insight into the Crystal Structure. *Chem. Mater.* **2013**, *25* (20), 4064–4070.

(42) Mohanty, D.; Sefat, A. S.; Li, J.; Meisner, R. A.; Rondinone, A. J.; Payzant, E. A.; Abraham, D. P.; Wood, D. L.; Daniel, C. Correlating Cation Ordering and Voltage Fade in a Lithium-Manganese-Rich Lithium-Ion Battery Cathode Oxide: A Joint Magnetic Susceptibility and TEM Study. *Phys. Chem. Chem. Phys.* **2013**, *15* (44), 19496–19509.

(43) Mohanty, D.; Sefat, A. S.; Kalnaus, S.; Li, J.; Meisner, R. A.; Payzant, E. A.; Abraham, D. P.; Wood, D. L.; Daniel, C. Investigating Phase Transformation in the Li1.2Co0.1Mn0.55Ni0.15O2 Lithium-Ion Battery Cathode during High-Voltage Hold (4.5 V) via Magnetic, X-Ray Diffraction and Electron Microscopy Studies. *J. Mater. Chem. A* **2013**, *1* (20), 6249.

(44) Sata, N.; Eberman, K.; Eberl, K.; Maier, J. Mesoscopic Fast Ion Conduction in Nanometre-Scale Planar Heterostructures. *Nature* **2000**, *408* (6815), 946–949.

(45) Maier, J. Nanoionics: Ion Transport and Electrochemical Storage in Confined Systems. *Nat. Mater.* **2005**, *4* (11), 805–815.

(46) Maier, J. Space Charge Regions in Solid Two Phase Systems and Their Conduction Contribution. *Berichte der Bunsen-Gesellschaft für Phys. Chemie* **1985**, *89* (x), 355–362.

(47) Maier, J. Ionic Conduction in Space Charge Regions. *Prog. Solid State Chem.* **1995**, *23* (3), 171–263.

(48) Takada, K. Interfacial Nanoarchitectonics for Solid-State Lithium Batteries. *Langmuir* **2013**, *29* (24), 7538–7541.

(49) Haruyama, J.; Sodeyama, K.; Han, L.; Takada, K.; Tateyama, Y. Space-Charge Layer Effect at Interface between Oxide Cathode and Sulfide Electrolyte in All-Solid-State Lithium-Ion Battery. *Chem. Mater.* **2014**, *26* (14), 4248–4255.

(50) Takada, K.; Ohta, N.; Zhang, L.; Fukuda, K.; Sakaguchi, I.; Ma, R.; Osada, M.; Sasaki, T. Interfacial Modification for High-Power Solid-State Lithium Batteries. *Solid State Ionics* **2008**.

(51) Ohta, N.; Takada, K.; Sakaguchi, I.; Zhang, L.; Ma, R.; Fukuda, K.; Osada, M.; Sasaki, T. LiNbO3-Coated LiCoO2 as Cathode Material for All Solid-State Lithium Secondary Batteries. *Electrochem. commun.* **2007**.

(52) Sakuda, A.; Hayashi, A.; Tatsumisago, M. Interfacial Observation between LiCoO2 Electrode and Li 2S-P2S5 Solid Electrolytes of All-Solid-State Lithium Secondary Batteries Using Transmission Electron Microscopy. *Chem. Mater.* **2010**, *22* (3), 949–956.

(53) Kim, K. H.; Iriyama, Y.; Yamamoto, K.; Kumazaki, S.; Asaka, T.; Tanabe, K.; Fisher, C. A. J.; Hirayama, T.; Murugan, R.; Ogumi, Z. Characterization of the Interface between LiCoO2and Li7La3Zr2O12in an All-Solid-State Rechargeable Lithium Battery. *J. Power Sources* **2011**, *196* (2), 764–767.

(54) Aboulaich, A.; Bouchet, R.; Delaizir, G.; Seznec, V.; Tortet, L.; Morcrette, M.; Rozier, P.; Tarascon, J. M.; Viallet, V.; Dollé, M. A New Approach to Develop Safe All-Inorganic Monolithic Li-Ion Batteries. *Adv. Energy Mater.* **2011**.

(55) Okumura, T.; Takeuchi, T.; Kobayashi, H. All-Solid-State Lithium-Ion Battery Using Li2.2C0.8B0.2O3 Electrolyte. *Solid State Ionics* **2016**.

(56) Zhai, H.; Xu, P.; Ning, M.; Cheng, Q.; Mandal, J.; Yang, Y. A Flexible Solid Composite Electrolyte with Vertically Aligned and Connected Ion-Conducting Nanoparticles for Lithium Batteries. *Nano Lett.* **2017**.

(57) Han, F.; Gao, T.; Zhu, Y.; Gaskell, K. J.; Wang, C. A Battery Made from a Single Material. *Adv. Mater.* **2015**.

(58) Liu, L.; Wang, Z.; Li, H.; Chen, L.; Huang, X. Al2O3-Coated LiCoO2 as Cathode Material for Lithium Ion Batteries. *Solid State Ionics* **2002**, *152–153*, 341–346.

(59) Aono, H. Ionic Conductivity of Solid Electrolytes Based on Lithium Titanium Phosphate. *J. Electrochem. Soc.* **1990**.

(60) Bernuy-Lopez, C.; Manalastas, W.; Lopez Del Amo, J. M.; Aguadero, A.; Aguesse, F.; Kilner, J. A. Atmosphere Controlled Processing of Ga-Substituted Garnets for High Li-Ion Conductivity Ceramics. *Chem. Mater.* **2014**.

(61) Gellert, M.; Dashjav, E.; Grüner, D.; Ma, Q.; Tietz, F. Compatibility Study of Oxide and Olivine Cathode Materials with Lithium Aluminum Titanium Phosphate. *Ionics (Kiel).* **2018**, *24* (4), 1001–1006.

(62) Kim, K. H.; Iriyama, Y.; Yamamoto, K.; Kumazaki, S.; Asaka, T.; Tanabe, K.; Fisher, C. A. J.; Hirayama, T.; Murugan, R.; Ogumi, Z. Characterization of the Interface between LiCoO2 and Li 7La3Zr2O12 in an All-Solid-State Rechargeable Lithium Battery. *J. Power Sources* **2011**, *196* (2), 764–767.

(63) Takada, K. Progress and Prospective of Solid-State Lithium Batteries. *Acta Mater.* **2013**, *61* (3), 759–770.

(64) Han, F.; Yue, J.; Chen, C.; Zhao, N.; Fan, X.; Ma, Z.; Gao, T.; Wang, F.; Guo, X.; Wang, C. Interphase Engineering Enabled All-Ceramic Lithium Battery. *Joule* **2018**, *2* (3), 497–508.

(65) Uhlenbruck, S.; Dornseiffer, J.; Lobe, S.; Dellen, C.; Tsai, C.; Gotzen, B.; Sebold, D.; Finsterbusch, M.; Guillon, O. Cathode-Electrolyte Material Interactions during Manufacturing of Inorganic Solid-State Lithium Batteries. **2017**, 197–206.

(66) Ohta, S.; Seki, J.; Yagi, Y.; Kihira, Y.; Tani, T.; Asaoka, T. Co-Sinterable Lithium Garnet-Type Oxide Electrolyte with Cathode for All-Solid-State Lithium Ion Battery. *J. Power Sources* **2014**, *265*, 40–44.

(67) Miara, L.; Windmuller, A. About the Compatibility between High Voltage Spinel Cathode Materials and Solid Oxide Electrolytes as a Function of Temperature. **2016**.

(68) Ren, Y.; Chen, K.; Chen, R.; Liu, T.; Zhang, Y.; Nan, C. W. Oxide Electrolytes for Lithium Batteries. *J. Am. Ceram. Soc.* **2015**, *98* (12), 3603–3623.

(69) Bachman, J. C.; Muy, S.; Grimaud, A.; Chang, H.; Pour, N.; Lux, S. F.; Paschos, O.; Maglia, F.; Lupart, S.; Lamp, P.; et al. Inorganic Solid-State Electrolytes for Lithium Batteries : Mechanisms and Properties Governing Ion Conduction. **2016**.

(70) Gummow, R. J.; Kock, A. De; Thackeray, M. M. Improved Capacity Retention in Rechargeable 4 V Lithium/Lithiummanganese Oxide (Spinel) Cells. *Solid State Ionics* **1994**, *2738* (94).

(71) Kobayashi, Y. All-Solid-State Lithium Secondary Battery with Ceramic/Polymer Composite Electrolyte. *Solid State Ionics* **2002**, *152–153*, 137–142.

(72) Guillon, O.; Gonzalez-Julian, J.; Dargatz, B.; Kessel, T.; Schierning, G.; Räthel, J.; Herrmann, M. Field-Assisted Sintering Technology/Spark Plasma Sintering: Mechanisms, Materials, and Technology Developments. *Adv. Eng. Mater.* **2014**, *16* (7), 830–849.

(73) Ya, M. O. H. N. A. G. I. The Effect of Electric Field and Pressure on the Synthesis and Consolidation of Materials : A Review of the Spark Plasma Sintering Method. **2006**, *1*, 763–777.

(74) Kali, R.; Mukhopadhyay, A. Spark Plasma Sintered / Synthesized Dense and Nanostructured Materials for Solid-State Li-Ion Batteries : Overview and Perspective. *J. Power Sources* **2014**, *247*, 920–931.

(75) Kobayashi, Y.; Takeuchi, T.; Tabuchi, M.; Ado, K.; Kageyama, H. Densification of LiTi 2 ž PO 4 / 3 -Based Solid Electrolytes By. **1999**.

(76) Li, J.; Doig, R.; Camardese, J.; Plucknett, K.; Dahn, J. R. Measurements of Interdiffusion Coefficients of Transition Metals in Layered Li-Ni-Mn-Co Oxide Core-Shell Materials during Sintering. *Chem. Mater.* **2015**, *27* (22), 7765–7773.

(77) García, D. E.; Seidel, J.; Janssen, R.; Claussen, N. Fast Firing of Alumina. *J. Eur. Ceram. Soc.* **1995**.

(78) Cantwell, P. R.; Tang, M.; Dillon, S. J.; Luo, J.; Rohrer, G. S.; Harmer, M. P. Grain Boundary Complexions. *Acta Mater.* **2014**.

(79) Luo, J. Stabilization of Nanoscale Quasi-Liquid Interfacial Films in Inorganic Materials: A Review and Critical Assessment. *Crit. Rev. Solid State Mater. Sci.* **2007**.

(80) Luo, J. Interfacial Engineering of Solid Electrolytes. *J. Mater.* **2015**, *1* (1), 22–32.

(81) Mei, A.; Wang, X. L.; Lan, J. Le; Feng, Y. C.; Geng, H. X.; Lin, Y. H.; Nan, C. W. Role of Amorphous Boundary Layer in Enhancing Ionic Conductivity of Lithium-Lanthanum-Titanate Electrolyte. *Electrochim. Acta* **2010**.

(82) Ma, C.; Chen, K.; Liang, C.; Nan, C. W.; Ishikawa, R.; More, K.; Chi, M. Atomic-Scale Origin of the Large Grain-Boundary Resistance in Perovskite Li-Ion-Conducting Solid Electrolytes. *Energy Environ. Sci.* **2014**.

(83) Kayyar, A.; Qian, H.; Luo, J. Surface Adsorption and Disordering in LiFePO 4 Based Battery Cathodes. *Appl. Phys. Lett.* **2009**.

(84) Chiang, Y.-M.; Birnie, D. P.; Kingery, W. D. *Physical Ceramics*; 1997.

(85) Barsoum, M. W. *Fundamentals Of Ceramics*; 2003.

(86) Wu, J.-F.; Guo, X. Origin of the Low Grain Boundary Conductivity in Lithium Ion Conducting Perovskites: $Li_{3x}La_{0.67-x}TiO_3$. *Phys. Chem. Chem. Phys.* **2017**, *19* (8), 5880–5887.

(87) Huggins, R. A. *Advanced Batteries: Materials Science Aspects*; 2009.

(88) Kang, B.; Ceder, G. Battery Materials for Ultrafast Charging and Discharging. *Nature* **2009**.

(89) Li, M.; Lu, J.; Chen, Z.; Amine, K. 30 Years of Lithium-Ion Batteries. *Adv. Mater.* **2018**, *30* (33), 1–24.

(90) Zhang, Z.; Shao, Y.; Lotsch, B.; Hu, Y. S.; Li, H.; Janek, J.; Nazar, L. F.; Nan, C. W.; Maier, J.; Armand, M.; et al. New Horizons for Inorganic Solid State Ion Conductors. *Energy Environ. Sci.* **2018**, *11* (8), 1945–1976.

(91) Zheng, F.; Kotobuki, M.; Song, S.; Lai, M. O.; Lu, L.; Goodenough, J. B.; Singh, P.; Li, J.; Ma, C.; Chi, M.; et al. Inorganic Solid-State Electrolytes for Lithium Batteries: Mechanisms and Properties Governing Ion Conduction. *Adv. Energy Mater.* **2015**, *116* (1), 1–6.

(92) Hao, F.; Han, F.; Liang, Y.; Wang, C.; Yao, Y. Architectural Design and Fabrication Approaches for Solid-State Batteries. *MRS Bull.* **2018**, *43* (10), 746–751.

(93) Levit, O.; Xu, P.; Shvartsev, B.; Avioz Cohen, G.; Stanciu, L.; Tsur, Y.; Ein-Eli, Y. Interphases Formation and Analysis at the Lithium–Aluminum–Titanium–Phosphate (LATP) and Lithium–Manganese Oxide Spinel (LMO) Interface during High-Temperature Bonding. *Energy Technol.* **2020**, *8* (12), 1–12.

(94) Li, J.; Ma, C.; Chi, M.; Liang, C.; Dudney, N. J. Solid Electrolyte: The Key for High-Voltage Lithium Batteries. *Adv. Energy Mater.* **2015**, *5* (4), 1–6.

(95) Wolfenstine, J.; Allen, J. L.; Sakamoto, J.; Siegel, D. J.; Choe, H. Mechanical Behavior of Li-Ion-Conducting Crystalline Oxide-Based Solid Electrolytes: A Brief Review. *Ionics (Kiel).* **2017**, 1–6.

(96) Gao, Z.; Sun, H.; Fu, L.; Ye, F.; Zhang, Y.; Luo, W.; Huang, Y. Promises, Challenges, and Recent Progress of Inorganic Solid-State Electrolytes for All-Solid-State Lithium Batteries. *Adv. Mater.* **2018**, *30* (17), 1–27.

(97) Pervez, S. A.; Cambaz, M. A.; Thangadurai, V.; Fichtner, M. Interface in Solid-State Lithium Battery: Challenges, Progress, and Outlook. *ACS Appl. Mater. Interfaces* **2019**.

(98) Wu, Z.; Xie, Z.; Yoshida, A.; Wang, Z.; Hao, X.; Abudula, A.; Guan, G. Utmost Limits of Various Solid Electrolytes in All-Solid-State Lithium Batteries: A Critical Review. *Renew. Sustain. Energy Rev.* **2019**, *109* (March), 367–385.

(99) Seino, Y.; Ota, T.; Takada, K.; Hayashi, A.; Tatsumisago, M. A Sulphide Lithium Super Ion Conductor Is Superior to Liquid Ion Conductors for Use in Rechargeable Batteries. *Energy Environ. Sci.* **2014**, *7* (2), 627–631.

(100) Harada, Y.; Ishigaki, T.; Kawai, H.; Kuwano, J. Lithium Ion Conductivity of Polycrystalline Perovskite La0.67-XLi3xTiO3 with Ordered and Disordered Arrangements of the A-Site Ions. *Solid State Ionics* **1998**, *108* (1–4), 407–413.

(101) Haruyama, J.; Sodeyama, K.; Han, L.; Takada, K.; Tateyama, Y. Space-Charge Layer Effect at Interface between Oxide Cathode and Sulfide Electrolyte in All-Solid-State Lithium-Ion Battery. *Chem. Mater.* **2014**.

(102) Nie, K.; Hong, Y.; Qiu, J.; Li, Q.; Yu, X.; Li, H.; Chen, L. Interfaces between Cathode and Electrolyte in Solid State Lithium Batteries: Challenges and Perspectives. *Front. Chem.* **2018**, *6* (DEC), 1–19.

(103) Santhanagopalan, D.; Qian, D.; McGilvray, T.; Wang, Z.; Wang, F.; Camino, F.; Graetz, J.; Dudney, N.; Meng, Y. S. Interface Limited Lithium Transport in Solid-State Batteries. *J. Phys. Chem. Lett.* **2014**, *5* (2), 298–303.

(104) Park, K.; Yu, B. C.; Jung, J. W.; Li, Y.; Zhou, W.; Gao, H.; Son, S.; Goodenough, J. B. Electrochemical Nature of the Cathode Interface for a Solid-State Lithium-Ion Battery: Interface between LiCoO2 and Garnet-Li7La3Zr2O12. *Chem. Mater.* **2016**, *28* (21), 8051–8059.

(105) Ohta, S.; Seki, J.; Yagi, Y.; Kihira, Y.; Tani, T.; Asaoka, T. Co-Sinterable Lithium Garnet-Type Oxide Electrolyte with Cathode for All-Solid-State Lithium Ion Battery. *J. Power Sources* **2014**, *265*, 40–44.

(106) Kato, T.; Hamanaka, T.; Yamamoto, K.; Hirayama, T.; Sagane, F.; Motoyama, M.; Iriyama, Y. In-Situ Li7La3Zr2O12/LiCoO2interface Modification for Advanced All-Solid-State Battery. *J. Power Sources* **2014**, *260*, 292–298.

(107) Ohta, N.; Takada, K.; Zhang, L.; Ma, R.; Osada, M.; Sasaki, T. Enhancement of the High-Rate Capability of Solid-State Lithium Batteries by Nanoscale Interfacial Modification. *Adv. Mater.* **2006**, *18* (17), 2226–2229.

(108) Liu, T.; Ren, Y.; Shen, Y.; Zhao, S. X.; Lin, Y.; Nan, C. W. Achieving High Capacity in Bulk-Type Solid-State Lithium Ion Battery Based on Li6.75La3Zr1.75Ta0.25O12 Electrolyte: Interfacial Resistance. *J. Power Sources* **2016**, *324*, 349–357.

(109) Gellert, M.; Dashjav, E.; Grüner, D.; Ma, Q.; Tietz, F. Compatibility Study of Oxide and Olivine Cathode Materials with Lithium Aluminum Titanium Phosphate. *Ionics (Kiel).* **2018**, *24* (4), 1001–1006.

(110) Miara, L.; Windmüller, A.; Tsai, C. L.; Richards, W. D.; Ma, Q.; Uhlenbruck, S.; Guillon, O.; Ceder, G. About the Compatibility between High Voltage Spinel Cathode Materials and Solid Oxide Electrolytes as a Function of Temperature. *ACS Appl. Mater. Interfaces* **2016**, *8* (40), 26842–26850.

(111) Aboulaich, A.; Bouchet, R.; Delaizir, G.; Seznec, V.; Tortet, L.; Morcrette, M.; Rozier, P.; Tarascon, J. M.; Viallet, V.; Dollé, M. A New Approach to Develop Safe All-Inorganic Monolithic Li-Ion Batteries. *Adv. Energy Mater.* **2011**, *1* (2), 179–183.

(112) Munir, Z. A.; Anselmi-Tamburini, U.; Ohyanagi, M. The Effect of Electric Field and Pressure on the Synthesis and Consolidation of Materials: A Review of the Spark Plasma Sintering Method. *J. Mater. Sci.* **2006**, *41* (3), 763–777.

(113) Garay, J. E.; Anselmi-Tamburini, U.; Munir, Z. A. Enhanced Growth of Intermetallic Phases in the Ni-Ti System by Current Effects. *Acta Mater.* **2003**, *51* (15), 4487–4495.

(114) Xu, P.; Rheinheimer, W.; Shuvo, S. N.; Qi, Z.; Levit, O.; Wang, H.; Ein-Eli, Y.; Stanciu, L. A. Origin of High Interfacial Resistances in Solid-State Batteries: Interdiffusion and Amorphous Film Formation in Li 0.33 La 0.57 TiO 3 /LiMn 2 O 4 Half Cells . *ChemElectroChem* **2019**, *6* (17), 4576–4585.

(115) Takahashi, Y.; Tode, S.; Kinoshita, A.; Fujimoto, H.; Nakane, I.; Fujitani, S. Development of Lithium-Ion Batteries with a LiCoO2 Cathode toward High Capacity by Elevating Charging Potential. *J. Electrochem. Soc.* **2008**, *155* (7), 537–541.

(116) Ozawa, K. Lithium-Ion Rechargeable Batteries with LiCoO2 and Carbon Electrodes: The LiCoO2/C System. *Solid State Ionics* **1994**, *69* (3–4), 212–221.

(117) Ren, Y.; Liu, T.; Shen, Y.; Lin, Y.; Nan, C. W. Chemical Compatibility between Garnet-like Solid State Electrolyte Li6.75La3Zr1.75Ta0.25O12 and Major Commercial Lithium Battery Cathode Materials. *J. Mater.* **2016**, *2* (3), 256–264.

(118) Aroshas, R.; Kalabukhov, S.; Stern, A.; Frage, N. Diffusion Bonding of Ceramics by Spark Plasma Sintering (SPS) Apparatus. *Adv. Mater. Res.* **2015**, *1111*, 97–102.

(119) Ma, C.; Chi, M. Novel Solid Electrolytes for Li-Ion Batteries: A Perspective from Electron Microscopy Studies. *Front. Energy Res.* **2016**, *4* (JUN), 1–6.

(120) Cantwell, P. R.; Tang, M.; Dillon, S. J.; Luo, J.; Rohrer, G. S.; Harmer, M. P. Grain Boundary Complexions. *Acta Mater.* **2014**, *62* (1), 1–48.

(121) Ong, S. P.; Jain, A.; Hautier, G.; Kang, B.; Ceder, G. Thermal Stabilities of Delithiated Olivine MPO4 (M = Fe, Mn) Cathodes Investigated Using First Principles Calculations. *Electrochem. commun.* **2010**, *12* (3), 427–430.

(122) Ong, S. P.; Wang, L.; Kang, B.; Ceder, G. Li - Fe - P - O2 Phase Diagram from First Principles Calculations. *Chem. Mater.* **2008**, *20* (5), 1798–1807.

(123) Plimpton, S. Fast Parallel Algorithms for Short-Range Molecular Dynamics. *Journal of Computational Physics*. 1995, pp 1–19.

(124) Coleman, S. P.; Spearot, D. E.; Capolungo, L. Virtual Diffraction Analysis of Ni [0 1 0] Symmetric Tilt Grain Boundaries. *Model. Simul. Mater. Sci. Eng.* **2013**, *21* (5).

(125) Coleman, S. P.; Sichani, M. M.; Spearot, D. E. A Computational Algorithm to Produce Virtual X-Ray and Electron Diffraction Patterns from Atomistic Simulations. *Jom* **2014**, *66* (3), 408–416.

(126) Inaguma, Y.; Liquan, C.; Itoh, M.; Nakamura, T.; Uchida, T.; Ikuta, H.; Wakihara, M. High Ionic Conductivity in Lithium Lanthanum Titanate. *Solid State Commun.* **1993**, *86* (10), 689–693.

(127) Wenzel, S.; Leichtweiss, T.; Krüger, D.; Sann, J.; Janek, J. Interphase Formation on Lithium Solid Electrolytes - An in Situ Approach to Study Interfacial Reactions by Photoelectron Spectroscopy. *Solid State Ionics* **2015**, *278*, 98–105.

(128) Maria, J. P.; Kang, X.; Floyd, R. D.; Dickey, E. C.; Guo, H.; Guo, J.; Baker, A.; Funihashi, S.; Randall, C. A. Cold Sintering: Current Status and Prospects. *J. Mater. Res.* **2017**, *32* (17), 3205–3218.

(129) Guo, H.; Baker, A.; Guo, J.; Randall, C. A. Cold Sintering Process: A Novel Technique for Low-Temperature Ceramic Processing of Ferroelectrics. *J. Am. Ceram. Soc.* **2016**.

(130) Guo, J.; Baker, A. L.; Guo, H.; Lanagan, M.; Randall, C. A. Cold Sintering Process: A New Era for Ceramic Packaging and Microwave Device Development. *J. Am. Ceram. Soc.* **2017**, *100* (2), 669–677.

(131) Van Santen, R. A. The Ostwald Step Rule. *J. Phys. Chem.* **1984**, *88* (24), 5768–5769.

(132) Guo, H.; Baker, A.; Guo, J.; Randall, C. A. Protocol for Ultralow-Temperature Ceramic Sintering: An Integration of Nanotechnology and the Cold Sintering Process. *ACS Nano* **2016**, *10* (11), 10606–10614.

(133) Liu, Y.; Sun, Q.; Wang, D.; Adair, K.; Liang, J.; Sun, X. Development of the Cold Sintering Process and Its Application in Solid-State Lithium Batteries. *J. Power Sources* **2018**, *393* (March), 193–203.

(134) Berbano, S. S.; Guo, J.; Guo, H.; Lanagan, M. T.; Randall, C. A. Cold Sintering Process of Li1.5Al0.5Ge1.5(PO4)3 Solid Electrolyte. *J. Am. Ceram. Soc.* **2017**, *100* (5), 2123–2135.

(135) Seo, J. H.; Verlinde, K.; Guo, J.; Heidary, D. S. B.; Rajagopalan, R.; Mallouk, T. E.; Randall, C. A. Cold Sintering Approach to Fabrication of High Rate Performance Binderless LiFePO4 Cathode with High Volumetric Capacity. *Scr. Mater.* **2018**, *146*, 267–271.

(136) Du, M.; Liao, K.; Lu, Q.; Shao, Z. Recent Advances in the Interface Engineering of Solid-State Li-Ion Batteries with Artificial Buffer Layers: Challenges, Materials, Construction, and Characterization. *Energy Environ. Sci.* **2019**, *12* (6), 1780–1804.

(137) Xu, L.; Tang, S.; Cheng, Y.; Wang, K.; Liang, J.; Liu, C.; Cao, Y. C.; Wei, F.; Mai, L. Interfaces in Solid-State Lithium Batteries. *Joule* **2018**, *2* (10), 1991–2015.

(138) Xu, W.; Wang, J.; Ding, F.; Chen, X.; Nasybulin, E.; Zhang, Y.; Zhang, J. G. Lithium Metal Anodes for Rechargeable Batteries. *Energy Environ. Sci.* **2014**, *7* (2), 513–537.

(139) Eftekhari, A. Low Voltage Anode Materials for Lithium-Ion Batteries. *Energy Storage Mater.* **2017**, *7* (January), 157–180.

(140) Lin, D.; Liu, Y.; Cui, Y. Reviving the Lithium Metal Anode for High-Energy Batteries. *Nat. Nanotechnol.* **2017**, *12* (3), 194–206.

(141) Hatzell, K. B.; Chen, X. C.; Cobb, C. L.; Dasgupta, N. P.; Dixit, M. B.; Marbella, L. E.; McDowell, M. T.; Mukherjee, P. P.; Verma, A.; Viswanathan, V.; et al. Challenges in Lithium Metal Anodes for Solid-State Batteries. *ACS Energy Lett.* **2020**, *5* (3), 922–934.

(142) Monroe, C.; Newman, J. The Impact of Elastic Deformation on Deposition Kinetics at Lithium/Polymer Interfaces. *J. Electrochem. Soc.* **2005**, *152* (2), A396.

(143) Cao, D.; Sun, X.; Li, Q.; Natan, A.; Xiang, P.; Zhu, H. Lithium Dendrite in All-Solid-State Batteries: Growth Mechanisms, Suppression Strategies, and Characterizations. *Matter* **2020**, *3* (1), 57–94.

(144) Ishiguro, K.; Nakata, Y.; Matsui, M.; Uechi, I.; Takeda, Y.; Yamamoto, O.; Imanishi, N. Stability of Nb-Doped Cubic Li 7 La 3 Zr 2 O 12 with Lithium Metal . *J. Electrochem. Soc.* **2013**, *160* (10), A1690–A1693.

(145) Cheng, X. B.; Zhao, C. Z.; Yao, Y. X.; Liu, H.; Zhang, Q. Recent Advances in Energy Chemistry between Solid-State Electrolyte and Safe Lithium-Metal Anodes. *Chem* **2019**, *5* (1), 74–96.

(146) Tsai, C. L.; Roddatis, V.; Chandran, C. V.; Ma, Q.; Uhlenbruck, S.; Bram, M.; Heitjans, P.; Guillon, O. Li7La3Zr2O12 Interface Modification for Li Dendrite Prevention. *ACS Appl. Mater. Interfaces* **2016**, *8* (16), 10617–10626.

(147) Shen, F.; Dixit, M. B.; Xiao, X.; Hatzell, K. B. Effect of Pore Connectivity on Li Dendrite Propagation within LLZO Electrolytes Observed with Synchrotron X-Ray Tomography. *ACS Energy Lett.* **2018**, *3* (4), 1056–1061.

(148) Zhang, Z.; Zhang, L.; Liu, Y.; Wang, H.; Yu, C.; Zeng, H.; Wang, L. min; Xu, B. Interface-Engineered Li7La3Zr2O12-Based Garnet Solid Electrolytes with Suppressed Li-Dendrite Formation and Enhanced Electrochemical Performance. *ChemSusChem* **2018**, *11* (21), 3774–3782.

(149) Cheng, L.; Chen, W.; Kunz, M.; Persson, K.; Tamura, N.; Chen, G.; Doeff, M. Effect of Surface Microstructure on Electrochemical Performance of Garnet Solid Electrolytes. *ACS Appl. Mater. Interfaces* **2015**, *7* (3), 2073–2081.

(150) Chen, C. H.; Amine, K. Ionic Conductivity, Lithium Insertion and Extraction of Lanthanum Lithium Titanate. *Solid State Ionics* **2001**, *144* (1–2), 51–57.

(151) Wenzel, S.; Leichtweiss, T.; Krüger, D.; Sann, J.; Janek, J. Interphase Formation on Lithium Solid Electrolytes - An in Situ Approach to Study Interfacial Reactions by Photoelectron Spectroscopy. *Solid State Ionics* **2015**, *278*, 98–105.

(152) Wu, B.; Wang, S.; Lochala, J.; Desrochers, D.; Liu, B.; Zhang, W.; Yang, J.; Xiao, J. The Role of the Solid Electrolyte Interphase Layer in Preventing Li Dendrite Growth in Solid-State Batteries. *Energy Environ. Sci.* **2018**, *11* (7), 1803–1810.

(153) Ren, Y.; Shen, Y.; Lin, Y.; Nan, C. W. Direct Observation of Lithium Dendrites inside Garnet-Type Lithium-Ion Solid Electrolyte. *Electrochem. commun.* **2015**, *57*, 27–30.

(154) Sudo, R.; Nakata, Y.; Ishiguro, K.; Matsui, M.; Hirano, A.; Takeda, Y.; Yamamoto, O.; Imanishi, N. Interface Behavior between Garnet-Type Lithium-Conducting Solid Electrolyte and Lithium Metal. *Solid State Ionics* **2014**, *262*, 151–154.

(155) Raj, R.; Wolfenstine, J. Current Limit Diagrams for Dendrite Formation in Solid-State Electrolytes for Li-Ion Batteries. *J. Power Sources* **2017**, *343*, 119–126.

(156) Albertus, P.; Babinec, S.; Litzelman, S.; Newman, A. Rechargeable Batteries. *Nat. Energy* **2018**, *3* (January).

(157) Zhu, J.; Zhao, J.; Xiang, Y.; Lin, M.; Wang, H.; Zheng, B.; He, H.; Wu, Q.; Huang, J. Y.; Yang, Y. Chemomechanical Failure Mechanism Study in NASICON-Type Li1.3Al0.3Ti1.7(PO4)3Solid-State Lithium Batteries. *Chem. Mater.* **2020**, *32* (12), 4998–5008.

(158) Pesci, F. M.; Brugge, R. H.; Hekselman, A. K. O.; Cavallaro, A.; Chater, R. J.; Aguadero, A. Elucidating the Role of Dopants in the Critical Current Density for Dendrite Formation in Garnet Electrolytes. *J. Mater. Chem. A* **2018**, *6* (40), 19817–19827.

(159) Sharafi, A.; Meyer, H. M.; Nanda, J.; Wolfenstine, J.; Sakamoto, J. Characterizing the Li-Li7La3Zr2O12 Interface Stability and Kinetics as a Function of Temperature and Current Density. *J. Power Sources* **2016**, *302*, 135–139.

(160) Yang, K. Y.; Leu, I. C.; Fung, K. Z.; Hon, M. H.; Hsu, M. C.; Hsiao, Y. J.; Wang, M. C. Mechanism of the Interfacial Reaction between Cation-Deficient La0.56 Li0.33 TiO3 and Metallic Lithium at Room Temperature. *J. Mater. Res.* **2008**, *23* (7), 1813–1825.